Fine and Coarse Dust Effects on Radiative Forcing, Mass Deposition, and Solar Devices over the Middle East

Suleiman Mostamandi[1], Alexander Ukhov[2], Johann P Engelbrecht[3], Illia Shevchenko[2], Sergey Osipov[4], and Georgiy Stenchikov[2]

[1]KAUST
[2]King Abdullah University of Science and Technology
[3]Desert Research Institute
[4]Max Planck Institute for Chemistry

June 23, 2023

Abstract

In desert regions like the Middle East (ME), dust has a profound impact on the environment, climate, air quality, and solar devices. The size of dust particles determines the extent of these effects. Dust deposition (DD) measurements show that coarse dust particles with geometric radius $r > 10$ µm comprise most of the deposited mass. Still, these particles are not represented in the current models that are tuned to fit the observed aerosol visible optical depth (AOD). As a result, the existing models and reanalysis products underestimate DD and dust emission (DE) almost three times. This is the first study to constrain the dust simulations by both AOD and DD measurements to quantify the effect of coarse and fine dust using the WRF-Chem model. We found that, on average, coarse dust contributes less than 10% to dust shortwave (SW) radiative forcing (RF) at the surface but comprises more than 70% of DE. Annual mean net RF over the Arabian Peninsula and regional seas locally reaches -25 W m-2. Airborne fine dust particles with radii $r < 3$ µm are mainly responsible for the significant dimming (5-10%) of solar radiation, cooling the surface and hampering solar energy production. However, dust mass deposition is primarily linked to coarse particles, decreasing the efficiency of Photovoltaic panels by 2-5% per day. Therefore, incorporating coarse dust in model simulations and data assimilation would improve the overall description of the dust mass balance and its impact on environmental systems and solar devices.

Fine and Coarse Dust Effects on Radiative Forcing, Mass Deposition, and Solar Devices over the Middle East

Suleiman Mostamandi[1], Alexander Ukhov[1], Johann Engelbrecht[1,2], Illia Shevchenko[1], Sergey Osipov[1], Georgiy Stenchikov[1]

[1]King Abdullah University of Science and Technology, Thuwal, Saudi Arabia
[2]Desert Research Institute, Reno, Nevada, USA

Key Points:

- Models and reanalysis products underestimate coarse dust emission and dust deposition by 2-3 times
- Fine dust affects radiation, but coarse dust dominates mass deposition rates
- Atmospheric dust dims solar radiation, and coarse dust causes soiling of solar panels

Key Words: Emission, Air quality, Arabian Peninsula, PV, Soiling, WRF-Chem

Corresponding author: Georgiy Stenchikov, `georgiy.stenchikov@kaust.edu.sa`

Abstract

In desert regions like the Middle East (ME), dust has a profound impact on the environment, climate, air quality, and human health. In addition, dust affects the efficiency of solar energy devices by reducing the downward solar flux and settling on their optically active surfaces. The size of dust particles determines the extent of these effects. Our size-segregated dust deposition (DD) measurements show that coarse dust particles with geometric radius r > 10 μm comprise the majority of the deposited mass, but these particles are not represented in the current models that are tuned to fit the observed aerosol visible optical depth (AOD) but not dust emission (DE) or DD. As a result, the current models and reanalysis products severely underestimate DD and DE. This is the first study to constrain the dust simulations by both AOD and DD measurements to quantify the effect of coarse and fine dust on radiative fluxes and DD/DE rates using the WRF-Chem model. We found that, on average, coarse dust contributes less than 10% to dust shortwave (SW) radiative forcing (RF) at the surface but comprises more than 70% of DE. Coarse dust warms the atmosphere more effectively than fine dust in longwave (LW), comprising 30% of LW RF at the surface, although the LW effect is 2-3 times smaller than the SW effect. Aerosol annual mean net radiative cooling at the surface over the Arabian Peninsula and regional seas locally reaches 25 $W\ m^{-2}$. Airborne fine dust particles with radii r < 3 μm are mainly responsible for the significant dimming (5-10%) of solar radiation, cooling the surface and hampering solar energy production. However, dust mass deposition is primarily linked to coarse particles, causing accumulation of soiling losses at the rate of 2-5% per day. Therefore, incorporating coarse dust in model simulations and data assimilation would improve the overall description of the dust mass balance and its impact on environmental systems and solar devices.

1 Introduction

Mineral dust is a critical player in the earth system, with a broad impact on the environment and different aspects of weather, climate, planetary radiative budget, cloud microphysics, and atmospheric chemistry (Knippertz & Stuut, 2014; Anisimov et al., 2018; Z. Meng & Lu, 2007; Prospero et al., 2008; Ukhov et al., 2020; Parajuli et al., 2022). Dust fertilizes oceans by providing nutrients to surface waters and, ultimately, the seabed (Talbot et al., 1986; Watson et al., 2000; Swap et al., 1996; Zhu et al., 1997). The total annual dust deposition in the Red Sea reaches 8.6 Mt (Shevchenko et al., 2021), and major dust storms are estimated to contribute 6 Mt to this total (Jish Prakash et al., 2015). Dust can negatively impact infrastructure and technology by attenuating the solar radiation reaching the earth's surface due to dust scattering and absorption, therefore reducing the output of photovoltaic (PV) systems. Furthermore, dust deposition on solar panels diminishes their efficacy (Mani & Pillai, 2010a; Rao et al., 2014; Sulaiman et al., 2014; Valerino et al., 2020).

With its large deserts, the Middle East (ME) is one of the most significant mineral dust sources on Earth (Zender et al., 2004; Knippertz & Stuut, 2014; Ukhov et al., 2020). The region is characterized by hot, dry summers and mild winters with intermittent rains (Climate.com, 2018; Mostamandi et al., 2022). In summer, northern wind (Shamal) dominates (Yu et al., 2016; Hamidi et al., 2013; Anisimov et al., 2018); whereas in winter, southern wind, related to monsoon circulation, prevails. Column dust loading (DL) is controlled by dust emission (DE), dust transport (DT), and dust deposition (DD) (Knippertz & Stuut, 2014). DE is difficult to measure in situ and also to calculate in meteorological and climate models coupled with aerosol chemical transport models (Zender et al., 2004; Uno et al., 2006; Todd et al., 2008; Ginoux et al., 2012). The main mechanisms of dust generation in the ME are cold fronts, haboobs, and gust winds, but they are not all well represented in the up-to-date atmospheric chemical transport models. To resolve haboobs, for example, a grid spacing of at least 3-km is required to allow resolving deep convection (Anisimov et al., 2018; Kalenderski & Stenchikov, 2016). Unfortunately, calculations at this level of resolution require enormous computational resources and are not yet practical for long-term simulations. Insufficient model spatial resolution is compensated by adjusting the DE to fit the observed aerosol optical depth (AOD) (Anisimov et al., 2018; Z. Meng & Lu, 2007; Ukhov et al., 2020; Parajuli et al., 2022). However, DE is intrinsically related to DD because all emitted dust eventually settles to the surface. Thus, averaged annually and over the globe, DE = DD.

In addition to absorbing and scattering radiation, dust affects clouds, acting as cloud condensation nuclei (CCN) and ice nuclei (IN), and causes indirect radiation forcing (RF) (DeMott et al., 2010; Parajuli et al., 2022). Deposited dust alters surface albedo and harms vegetation (Chadwick et al., 1999). DL and dust optical depth (DOD) over the ME are higher than in other parts of the world (Jish Prakash et al., 2015; Kalenderski et al., 2013). Osipov et al. (2015) and Kalenderski and Stenchikov (2016) showed that mineral dust over the ME contributes more than 80% to AOD. Non-dust aerosols like sulfate (SO_4), sea salt (SS), black carbon (BC), organic carbon (OC), and volatile organic compounds (VOCs) comprise, on average, about 20% of AOD. We assume that the optical depth of non-dust aerosols is NOD=AOD-DOD. Osipov et al. (2022) indicated an even larger fractional contribution (about 30%) of anthropogenic fine particulates with geometric diameter less than 1 μm to AOD. In this study, we characterize particles by their geometric radii instead of using aerodynamic radii; for dust, aerodynamic radii are almost 50% smaller than geometric radii (Adebiyi et al., 2023).

Dust impacts regional radiative balance, thus affecting climate (Forster et al., 2007; Zhao et al., 2014; Ukhov et al., 2020). Kalenderski et al. (2013) simulated reduction of solar radiation at the earth's surface during a dust storm reaching 100 $W\ m^{-2}$. Osipov and Stenchikov (2018) calculated that the dust radiative effect has a profound thermal and dynamic impact on the Red Sea. Over the last two decades, the dust effects on the environment have been extensively studied (Marticorena & Bergametti, 1995; Ginoux et al., 2001; Shao, 2001; Zender et al., 2003; Darmenova et al., 2009; Shao et al., 2010; Zhao et al., 2010; Solomos et al., 2011; Mahowald et al., 2011; Cakmur et al., 2006; Kok et al., 2021; Adebiyi et al., 2023; Adebiyi & Kok, 2020). Although up-to-date models capture many features of dust generation and transport, the spatial distribution of dust and its RF remains uncertain (Zhao et al., 2013). For example, the simulated global DE in AeroCom models varies from 500 $Mt\ year^{-1}$ to 5000 $Mt\ year^{-1}$ (Textor et al., 2006; Huneeus et al., 2011; Kalenderski & Stenchikov, 2016).

The discrepancies in simulated dust emissions can be attributed to the fact that models are tuned to fit the observed visible AOD, and DE is a tuning parameter. Among different models, varying dust sources, particle size distribution (PSD), optical properties, and chemical composition are the major factors that exacerbate differences in the emissions (Ginoux et al., 2012; Tegen et al., 2002; Zender et al., 2003; Balkanski et al., 2007; Darmenova et al., 2009; McConnell et al., 2010; Kok, 2011; Zhao et al., 2010, 2011).

Dust size distribution and composition are key factors that control dust optical properties and the rate of gravitational sedimentation (Mallet et al., 2009; Bergametti & Forêt, 2014; Zhao et al., 2013; Mahowald et al., 2011; Kok et al., 2021; Adebiyi & Kok, 2020). However, the dust microphysical modules often do not consider giant (r > 10 μm) dust particles, which could be radiatively significant (Ryder et al., 2019; Kok et al., 2021; Adebiyi et al., 2023). The amount and size distribution of emitted dust depends on the surface wind, soil morphology, and moisture content. Kok (2011) analyzed six sets of size-resolved dust emission measurements and found that the size distribution of emitted fine dust with r < 5 μm is independent of wind speed (Kok, 2011; Kok et al., 2017). Adebiyi et al. (2023) suggested that the up-to-date models significantly underestimate coarse DL in the atmosphere because the models deposit coarse dust too rapidly.

Reducing the efficacy of solar energy devices is another aspect of dust impacts on human activities. Deserts receive a record amount of solar radiation, but a high concentration of dust in the atmosphere attenuates solar radiation at the Earth's surface. Dust deposited on PV panel surfaces causes soiling losses that accumulate at a rate of 0.1 to 1% per day (Ilse, Figgis, Naumann, et al., 2018; Valerino et al., 2020). Ilse, Figgis, Werner, et al. (2018) analyzed soiling and cementation processes on PV panels in Qatar, finding that dust deposition on PV surface causes energy losses exceeding 1% per day. Boyle et al. (2013, 2015) showed that 1 $g\ m^{-2}$ of dust deposited on a PV panel reduces power output by 4-6%. Ilse, Figgis, Naumann, et al. (2018) detected that the highest soiling rate is in the ME (0.95 % per day), and the lowest is in South America. Bergin et al. (2017) combined field measurements and global modeling to estimate the effect of aerosols on solar electricity generation, showing that about 17 to 25% of solar energy could be lost due to soiling in regions with abundant dust and anthropogenic aerosols. It was suggested that soiling losses associated with fine dust particles are larger than those caused by coarse particles (El-Shobokshy & Hussein, 1993; Sayyah et al., 2014; El-Shobokshy & Hussein, 1993; Ilse, Figgis, Werner, et al., 2018). Baras et al. (2016) conducted three years of soiling measurements in Rumah, Saudi Arabia, and proposed an 8-day cleaning cycle to increase the efficiency of PV panels. Mani and Pillai (2010b) found that weekly cleaning is necessary for the dry subtropics ($15-25°$N), which experience rare rainfall; in low latitudes with frequent rainfall, natural cleaning is usually sufficient. However, while heavy rains clean solar panels, light rains can increase surface contamination (Valerino et al., 2020; Ilse, Figgis, Naumann, et al., 2018). In regions with an arid and semi-arid climate, for example, dew can cause particle cementation on PV panel surfaces (Ilse, Figgis, Naumann, et al., 2018). Valerino et al. (2020) showed that high relative humidity almost doubles the soiling rate.

Thus both AOD and DD play an important role in shaping the dust impact on climate and solar devices. To achieve an agreement with observations, DE is usually tuned to fit the observed AOD in visible wavelengths in models. Because giant dust particles with r > 10 μm are often not considered in the models, the emission of dust particles with r < 10 μm is artificially increased to fit visible AOD, while the longwave (LW) effect of giant particles is underestimated (Zhao et al., 2014; Ukhov et al., 2020; Kalenderski et al., 2013; Adebiyi & Kok, 2020). At the same time, the simulated DD (and consequently DE) rates are much lower than observed (Engelbrecht et al., 2017; Shevchenko et al., 2021). DOD characterizes the amount of dust suspended in the atmosphere, and it alone is insufficient to constrain the dust mass balance because it is defined by DT, DD, and DE.

In this study, we combine model simulations, data assimilation products, and DD and AOD observations to quantify the dust impact in the ME. For the first time, we constrain the model dust simulations with both AOD and DD measurements. Considering the dust impact on solar devices, we account for both attenuation of incoming solar radiation by dust suspended in the atmosphere and soiling caused by DD, discriminating the effects of fine and coarse dust particles. Along with AOD observations, we utilize size-segregated DD measurements conducted at King Abdullah University of Science and Technology (KAUST, Saudi Arabia) (Jish Prakash et al., 2016; Engelbrecht et al., 2017; Shevchenko et al., 2021). We quantify the contributions of different dust sizes to RF and DD rate, aiming to answer the following questions:

1. What is the temporal and spatial distribution of dust mass deposition over the ME land areas and regional seas?
2. What are the comparative contributions of fine and coarse dust to radiative forcing and mass deposition rates over the ME?
3. What is the comparative impact of fine and coarse dust suspended in the atmosphere and deposited on surfaces on solar energy devices?

2 Methodology

First, we analyzed the model output obtained using the up-to-date model constrained only by AOD observations to reveal the deficiencies in the current models and reanalysis products. The size-segregated DD measurements, which we collected at the Red Sea coastal plain, allowed us to improve the model DE and calculate the effects of coarse and fine dust on DL, DD, RF, and the efficacy of solar devices. Below, in this section, we briefly discuss the data sets and the model used in this study.

2.1 Observations and Data Assimilation Products

The CIMEL robotic sun-photometer at the KAUST Campus has collected observations since the start of 2012. This instrument is part of the National Aeronautics and Space Administration (NASA) AErosol RObotic NETwork (AERONET, `http://aeronet.gsfc.nasa.gov`). The sun-photometer measures in clear-sky conditions direct sun and sky radiances at eight wavelengths (340, 380, 440, 500, 550, 670, 870, 940, and 1020 nm) every 15 min during daylight, providing spectral AODs and aerosol column integrated size distribution (Dubovik & King, 2000). AERONET data are available from `https://aeronet.gsfc.nasa.gov/cgi-bin/data_display_aod_v3?`. In addition to the KAUST site, this study uses AERONET observations from sites at Sede Boker and Mezaira (Fig. 1).

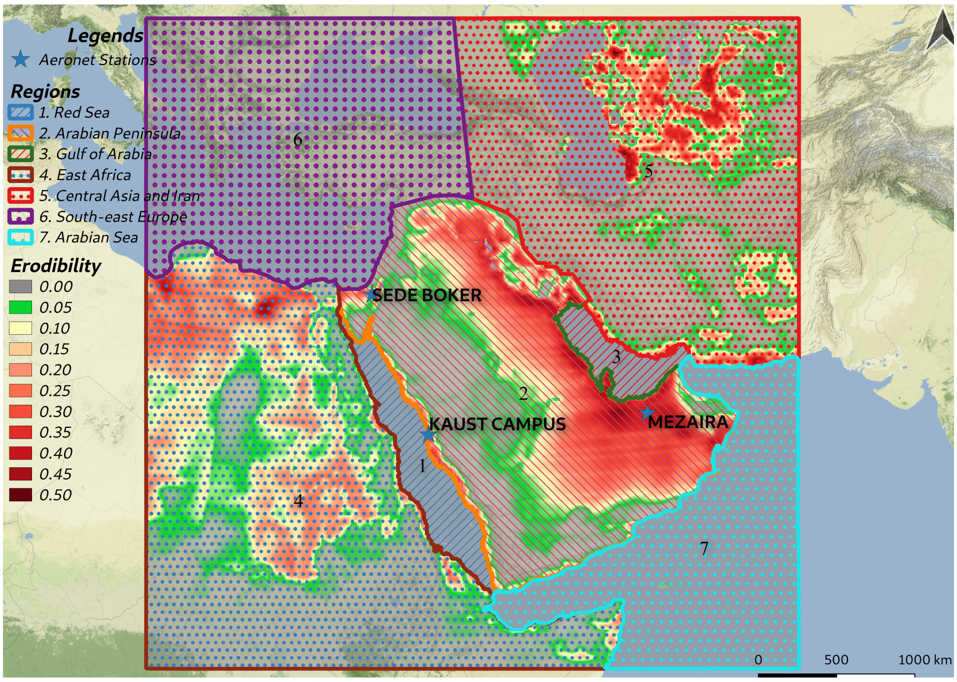

Figure 1: The square area depicts the simulation domain. Shading shows dust source function S. Contours show selected regions: 1 - The Red Sea, 0.46×10^6 km^2; 2 - Arabian Peninsula, 3.63×10^6 km^2; 3 - Arabian Gulf, 0.24×10^6 km^2; 4 - East Africa, 5.10×10^6 km^2; 5 - Central Asia and Iran, 4.51×10^6 km^2; 6 - South-East Europe, 3.37×10^6 km^2; and 7 - Arabian Sea, 2.09×10^6 km^2. Blue stars indicate the locations of AERONET stations used in the current study.

We used satellite observations to estimate the spatial-temporal distribution of modeled AOD. The Moderate Resolution Imaging Spectroradiometer (MODIS) instruments are aboard the NASA EOS (Earth Observing System) Terra and Aqua satellites. MODIS provides AOD over the global continents and oceans with a spatial resolution of $10 \times 10\ km^2$ (Remer et al., 2005; Abdou et al., 2005). We used AOD retrieval obtained using a "deep-blue" algorithm that is capable of providing aerosol optical thickness over bright land areas, such as most deserts (Levy et al., 2015).

To measure the amount of deposited dust, we used passive dust samplers, which collect settling dust in a sponge layer over a “frisbee plate” on a monthly basis. The dust was washed down from the frisbee and sponge with distilled water. After lyophilization, the samples were weighed and then subjected to XRD analysis to obtain their mineralogical composition. We measured particle size distribution in the samples using a Malvern Mastersizer 3000 Laser Diffraction Particle Size Analyzer (LPSA). The installation details, geographical coordinates of the deposition samplers, and observational data from December 2014-December 2019 can be found in (Shevchenko et al., 2021).

We also used reanalysis and data assimilation products as a data source. MERRA-2 reanalysis (`https://gmao.gsfc.nasa.gov/reanalysis/MERRA-2`) provides meteorological and atmospheric composition fields on a $0.625° \times 0.5°$ latitude-longitude grid and 72 terrain-following hybrid σ-p model levels (Randles et al., 2017; Buchard et al., 2017). MERRA-2 uses the Goddard Earth Observing System, version 5 (GEOS-5) atmospheric model (Rienecker et al., 2008), which is interactively coupled with the GOCART aerosol model (Chin et al., 2002, 2000). Anthropogenic emissions in MERRA-2 are based on the EDGAR-4.2 emission inventory (Janssens-Maenhout et al., 2013). MERRA-2 assimilates AERONET AODs and MODIS radiances (Randles et al., 2017). The European Center for Medium-Range Weather Forecast (ECMWF) Copernicus Atmosphere Monitoring Service (CAMS) provides operational daily analysis and forecast of AOD for aerosol species using an Integrated Forecast System (IFS) (Bozzo et al., 2017). The aerosol model implemented in CAMS is based on the modified version of the Laboratoire d’Optique Atmospherique (LMD) model (Boucher et al., 2002; Morcrette et al., 2009).

2.2 Model

In this study, we used a free-running regional meteorological and chemical transport model, WRF-Chem-3.7.1 (Skamarock et al., 2005; Grell et al., 2005), which has been configured for the ME. The model settings and the domain are similar to those we previously used in (Ukhov et al., 2020). The model domain (Fig. 1) covers the ME, Arabian Peninsula, Eastern Mediterranean, and parts of Central Asia with a $10 \times 10\ km^2$ horizontal grid and 50 hybrid vertical levels (See Figure 1). We employed the Yonsei University planetary boundary layer Scheme (YSU) (Hong et al., 2003). To account for atmospheric convection, we used the Grell 3D ensemble convective parameterization scheme (Grell & Dévényi, 2002).

To calculate atmospheric chemistry, we used the Regional Atmospheric Chemistry Mechanism (RACM) (Stockwell et al., 1997). The photolysis rates were calculated online according to (Madronich, 1987). Dust microphysics was calculated within the GOCART (Chin et al., 2000, 2002, 2014) model, which approximates the dust size distributions into five bins (Table 1).

The Rapid Radiative Transfer Model (RRTMG) for both SW and LW radiation is used for radiative transfer calculations (Iacono et al., 2008; E. Mlawer & Clough, 1998; E. J. Mlawer et al., 1997). In the course of this study, we found that WRF-Chem with GOCART microphysics erroneously disregards the radiative effect of dust particles with $r > 5\ \mu m$. However, GOCART considers particles with $0.1\ \mu m < r < 10\ \mu m$. We modified the code to rectify this error. It had a marginal effect in our previous simulations as bin 5 was poorly populated. However, it had a much stronger effect in the current study, as we significantly increased DE in bin 5 to account for the effect of giant dust particles (see below).

The dust emission scheme we employed in our simulations (Ginoux et al., 2001) assumes that dust emission mass flux, F_p ($\mu g\ m^{-2}\ s^{-1}$) in each dust-bin p=1,2,...,5 is defined by the relation:

$$F_p = \begin{cases} CSs_p u_{10m}^2(u_{10m} - u_t), & u_{10m} > u_t \\ 0, & u_{10m} < u_t \end{cases} \quad (1)$$

where C has the dimension of [$\mu g\ s^2\ m^{-5}$] and is a spatially uniform factor that controls the magnitude of dust emission flux; S is the dimensionless spatially varying dust source function (Ginoux et al., 2001) that characterizes the spatial distribution of dust emission sources ($0 < S < 1$); u_{10m} is the horizontal wind speed at 10 m above ground level; u_t is the threshold velocity, which depends on particle size and surface wetness; s_p is a fraction of dust mass emitted into dust-bin p, and $\sum s_p = 1$. s_p (p=1,2,3,4,5) defines the size distribution of emitted dust.

2.3 Model Tuning Using AERONET AOD and PSD

In (Ukhov et al., 2020), following the common practice (Kalenderski & Stenchikov, 2016; Jish Prakash et al., 2015; Zhao et al., 2010), we tuned dust emissions to fit the AOD from the AERONET stations located within the domain. For this purpose, the factor C from Eq. (1) was adjusted to obtain the best agreement between simulated and observed AOD at the KAUST Campus, the Mezaira, and Sede Boker AERONET sites (C = 0.525). We also tuned s_p from (1) to better reproduce the Aerosol Volume Size Distribution (PSD) provided by the AERONET inversion algorithm (Ukhov et al., 2020, 2021) (see Table 1).

Table 1: Dust Bins and Dust Emission Size Distribution Parameters

Dust Bins

Bin Numbers	1	2	3	4	5
Radii (μm)	0.1 - 1.0	1.0 - 1.8	1.8 - 3.0	3.0 - 6.0	6.0 - 10.0
Sp (Ukhov et al., 2020)	0.15	0.1	0.25	0.4	0.1
Sp (This Study)	0.05	0.03	0.07	0.12	0.73

The aerosol number-density or volume PSD defines the aerosol lifetime with respect to gravitational sedimentation and largely controls their radiative effect (Shevchenko et al., 2021; Osipov et al., 2015; Miller & Tegen, 1998; Highwood & Ryder, 2014; Scheuvens & Kandler, 2014; Maghami et al., 2016).

Figure 2 compares the annual average column integrated PSD from WRF-Chem simulations in (Ukhov et al., 2020) with PSD from the AERONET retrievals (Dubovik & King, 2000) for the KAUST Campus, Mezaira, and Sede Boker AERONET sites. The solid green line depicts AERONET PSD, the blue bars show PSD from (Ukhov et al., 2020), and the red bars show PSD obtained in this study (discussed below; Table 1). For all locations, the model in (Ukhov et al., 2020) reproduces the observed AERONET PSDs. The PSDs have a fine mode and coarse mode, peaking at r=0.2 μm and r=2.5 μm respectively. The AERONET retrievals and the model do not include particles with r > 10 μm. They are not approximated in the model (see Table 1) and AERONET is weakly sensitive to particles with r > 10 μm, which are much larger than the AERONET sun-photometer maximum operating wavelength of 1.02 μm. Further below we refer to the

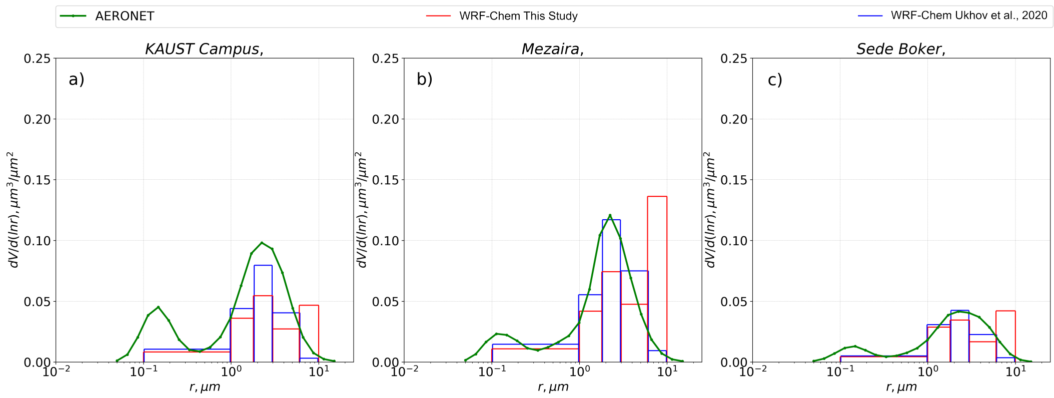

Figure 2: Annual average volume PSDs $\mu m^3 \mu m^{-2}$ calculated within WRF-Chem (bars), and obtained by AERONET inversion algorithm (green solid line) for 2016 at a) KAUST Campus, b) Mezaira and c) Sede Boker. The blue bars are from the WRF-Chem run without the DD constraints, and the red bars are from the current study with the DD constraints.

particles in the first three bins with r $<$ 3 μm as fine dust; the particles in bins 4 and 5 with 3 μm $<$ r $<$ 10 μm as coarse dust; and the particles with r $>$ 10 μm, that are not approximated in most models (but are present in the dust deposition samples), as giant dust particles.

2.4 Test of AOD Fitted Model against DD Observations

Before discussing the new model setup, the deficiencies of the previous free-running model simulations and data assimilation products constrained by only AERONET observations and tested against satellite AODs should be analyzed. To achieve this, we first compared the DD calculated in MERRA-2, CAMS, and the free-running WRF-Chem tuned using AERONET AOD as in (Ukhov et al., 2020) with the DD observations at the KAUST site. The data assimilation products, like MERRA-2 and CAMS, are often used as a proxy for observations, but none of the available assimilation systems are constrained by DD or DE measurements. Therefore, for these products, DD is based on their physical parameterizations, as in free-running WRF-Chem, and must be similarly tested against observations.

For this test, we used the DD measurements that have been conducted at the KAUST site since 2015 (Figure 3). To make a meaningful comparison of the observed and simulated DD, we measured PSD in all deposited samples (Engelbrecht et al., 2017; Shevchenko et al., 2021). The simulated (in WRF-Chem, MERRA-2, and CAMS) and observed monthly DD rates at the KAUST site throughout 2016 are shown in Figure 3, revealing a striking difference between the observed and simulated DD. The observed DD rates are more than three times higher than the simulated rates. This issue was discussed in (Engelbrecht et al., 2017; Shevchenko et al., 2021); the discrepancy occurs because we collect particles with radii up to 30 μm for observations, but in the models, we consider only particles with r $<$ 10 μm. At the same time, the DD of particles with r $<$ 5 μm in the models and reanalysis products compare well with observations. Figure 4a shows the 2016 annual average normalized (to 100%) volume PSD of deposited dust at the KAUST site (Shevchenko et al., 2021). Table 2 compares the DD rates at the KAUST campus calculated within WRF-Chem with the settings from (Ukhov et al., 2020), MERRA-2, and CAMS with 2016 observations (Shevchenko et al., 2021). The correlation coefficient (R), root mean square error (RMSE), and bias were calculated with respect to observations

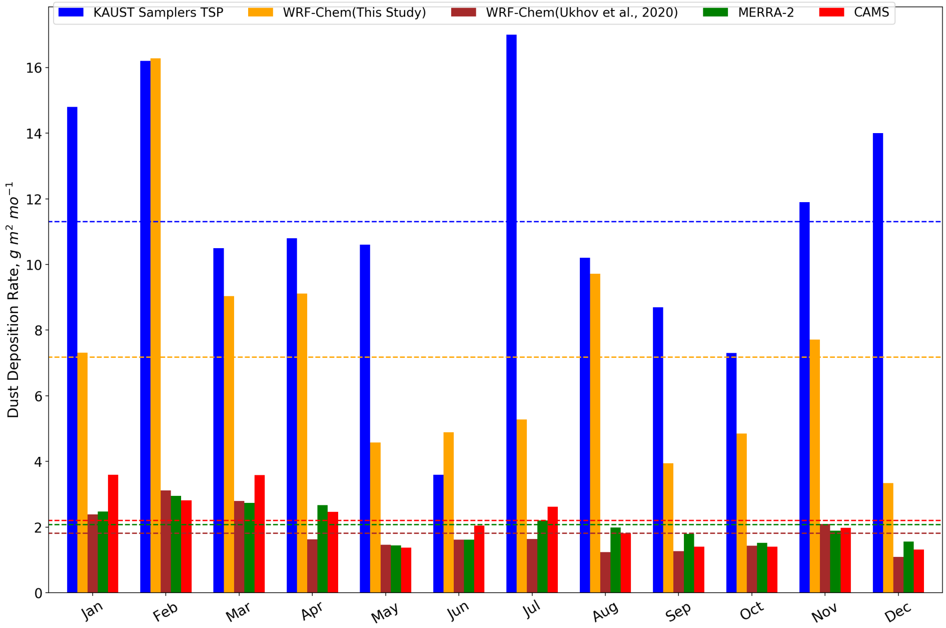

Figure 3: Monthly dust deposition rates ($g\ m^{-2} mo^{-1}$) averaged for six KAUST deposition sites (blue), simulated in WRF-Chem without the DD constraints (brown) and in the current study with DD constraints (light brown), calculated in MERRA-2 (green), and CAMS (red) at KAUST campus for 2016. Dashed lines show annual mean deposition rates for corresponding observations.

using monthly data. For WRF-Chem, R=0.70, while for MERRA-2 and CAMS R=0.25 and 0.36, respectively. The WRF-Chem DD annual bias = -9.48 $g\ m^{-2}\ mo^{-1}$. At the same time, WRF-Chem, MERRA-2, and CAMS reproduce the DD rate of particles with r $<$ 5 μm much better (see Table S1 in the supplement information). Thus, AERONET tuning helps to simulate the dust fraction with r $<$ 5 μm relatively well, but coarse (5 $<$ r $<$ 10) and giant (r $>$ 10) dust is simulated poorly.

Figure 4b presents the annual mean normalized (to 100%) volume PSD (shown in bins) of emitted and deposited dust calculated in the model (Ukhov et al., 2020), as well as dust suspended in the atmosphere at the KAUST site. Dust suspended in the atmosphere comprises a larger fraction of fine particles in bins 1, 2, and 3 than in dust emissions because these particles have a longer lifetime in the atmosphere than coarse particles in bins 4 and 5. Compared to emissions, the deposited dust has a larger fraction of the coarsest bins 4 and 5 because coarse particles deposit quickly. The fraction of coarse particles suspended in the atmosphere is 2-3 times smaller than in deposited dust. Thus, atmospheric dust loadings are less sensitive to coarse dust emission than DD. Comparing the size distributions of deposited dust in Figures 4a and b, we conclude that the WRF-Chem model with the settings from (Ukhov et al., 2020), in addition to the missing particles with r $>$ 10 μm, underestimates the emission of coarse particles with 6 μm $<$ r $<$ 10 μm in bin 5, as the observed size distribution reaches a maximum for r $>$ 10 μm but in simulation bin 4 (3-6 μm) is the most abundant. This indicates that even within the approximated dust sizes r $<$ 10 μm, the model underestimates the emission of coarse dust. In the new model setup developed in this study, we aim to fix this discrepancy and account for the effect of giant dust particles with r $>$ 10 μm by fitting AOD and DD simultaneously.

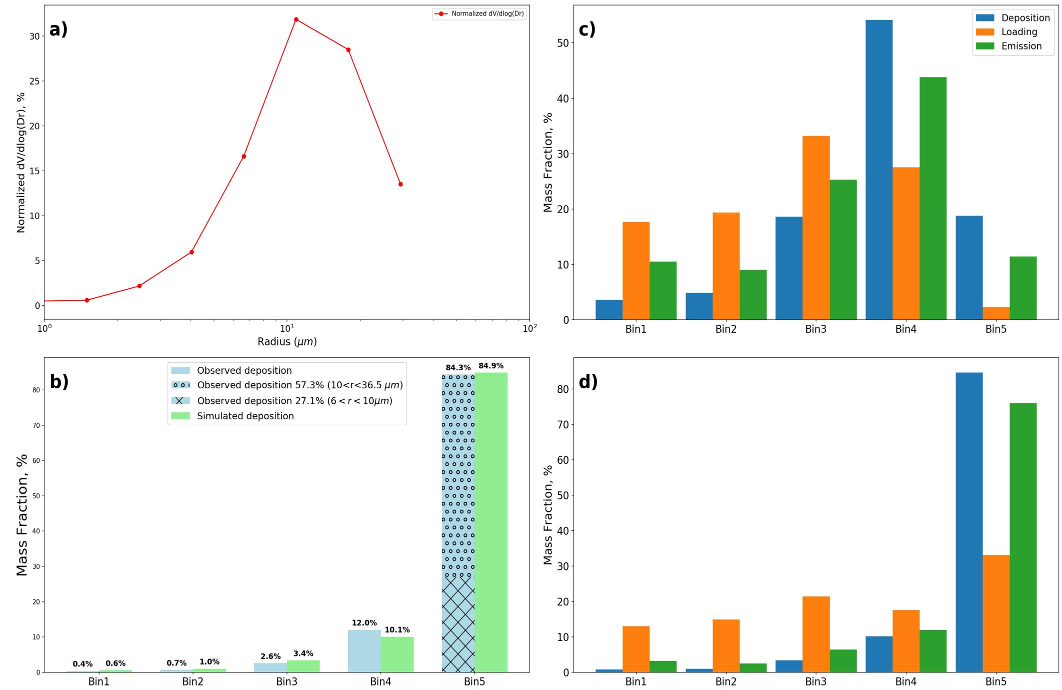

Figure 4: Annual mean normalized (to 100%) volume PSD for 2016: a) Measured in deposited samples at KAUST Campus; b) Simulated in bins in the run without DD constraints: DD (blue), DE (green), and DL (orange); c) DD simulated in bins in the run with DD constraints (blue) and integrated in bins using observed PSD in panel a; d) same as b), but in the run with the DD constraints.

Table 2: Statistical scores (R, RMSE, and Bias) of DD simulated within WRF-Chem, MERRA2, and CAMS compared to observations for 2016.

	R	RMSE	Bias
WRF-Chem (Ukhov et al., 2020)	0.70	10.10	-9.48
WRF-Chem (This Study)	0.79	5.75	-4.12
MERRA-2	0.25	9.85	-9.22
CAMS	0.36	9.19	-8.54

3 RESULTS

In this section, we first describe the new model setup constrained by AERONET AOD at three AERONET stations and DD observations at the KAUST site. We test the model results against observations and further discuss the geographical distributions of simulated SW and LW dust RF at the Earth's surface and DD over the Arabian Peninsula and the regional seas. We also develop a theoretical model to calculate the effect of DD and dust suspended in the atmosphere on the efficacy of PV panels.

3.1 Test of Model Setup with Simultaneous Fitting of AOD and DD

To simultaneously fit both AOD and DD in WRF-Chem simulations, we modified the DE size distribution, assuming that bin 5 incorporates a mass of dust particles with r > 6 μm including giant particles with r > 10 μm. The relative distribution of emitted mass in bins 1-4, which were constrained by AERONET PSD, remained intact. The new s_p settings are shown in Table 1. To fit the observed DD, we increased the emission in the largest bin 5 to 73% of the total mass. To fit the observed AOD, we chose C=1. It is suggested that the deposition rate for giant dust particles is overestimated in the models due to unaccounted asphericity of dust particles or turbulence effects (Adebiyi & Kok, 2020; Adebiyi et al., 2023). To overcome this deficiency, J. Meng et al. (2022), Adebiyi et al. (2023) decreased the density of giant particles. In our study, approximating the giant particles in bin 5 (6 μm < r < 10 μm) would effectively lower the sedimentation velocity for giant dust particles. The radiative effect of giant particles will be slightly overestimated both in SW and LW in our case, as particles in bin 5 are more optically effective per unit mass than giant dust particles both in SW and LW (this effect is quantified in section 3.2.3).

We ran the WRF-Chem-3.7.1 model for the entire year 2016. The lateral boundary and initial conditions for meteorological fields, aerosols, and chemical species were calculated using MERRA-2 reanalysis (Ukhov & Stenchikov, 2020). This provides the most consistent boundary conditions that allow us to use a moderate-size spatial domain and reduce computation time. Simulations were conducted for all months in parallel, with one week spin-up time for each month. The integration time step was 60 s.

In the chosen domain, there are three main dust emission areas (Figure 1). In Central Asia, dust is emitted predominantly between the Aral and Caspian Seas. In the Arabian Peninsula, the main dust sources are in the eastern region and a narrow zone along the west coast. In Africa, dust is generated in the Sahara and Somalian Peninsula. To represent climatology and spatial distribution of dust deposition, we divided our simulation domain into seven regions (Figure 1) based on the spatial patterns of the source function S.

To demonstrate how the model reproduces the DD and AOD, we test simulated both with observations. The bias of DD in the current simulations decreased at least two times compared with runs without DD tuning, and the correlation coefficient reached 0.79 (see Table 2). Figure 3 shows a subsequent better fit of DD and observations. Figure 5 demonstrates that the simulated AOD fits the AERONET observations at the KAUST, Mezaira, and Sede Boker sites well (see Figure 1). Table 3 compares the WRF-Chem, CAMS, and MERRA-2 daily averaged AODs with the AERONET observations at the KAUST Campus, Mezaira, and Sede Boker. Because of the finer spatial resolution, the free-running WRF-Chem outperforms the assimilation products. Table 4 summarizes the statistical scores for the simulated annual and seasonal mean AODs with respect to MODIS. WRF-Chem has the smallest RMSE and bias with respect to the MODIS AOD compared with MERRA-2 and CAMS data assimilation products. The spatial correlation of WRF-Chem AOD is close to that produced by both data-assimilation products.

Table 3: Statistical Scores (R and Bias) of daily mean AODs from CAMS, MERRA-2, and WRF-Chem with DD constraints with respect to AERONET AOD observations for 2016

	CAMS		MERRA-2		WRF-Chem	
	R	*bias*	*R*	*bias*	*R*	*bias*
KAUST Campus	0.71	0.01	0.85	-0.05	0.74	-0.04
Mezaira	0.62	0.12	0.83	0.04	0.73	0.07
Sede Boker	0.83	0.07	0.72	0.02	0.43	-0.01

Table 4: Statistical Scores (R, RMSE, and Bias) of annual and seasonal mean AODs for 2016 from CAMS, MERRA-2, and WRF-Chem with DD constraints with respect to MODIS observations

	CAMS			MERRA-2			WRF-Chem		
	R	*RMSE*	*bias*	*R*	*RMSE*	*bias*	*R*	*RMSE*	*bias*
Winter (DJF)	0.59	0.08	0.02	0.57	0.09	-0.03	0.47	0.08	-0.01
Spring (MAM)	0.70	0.13	0.05	0.72	0.13	-0.05	0.62	0.12	-0.01
Summer (JJA)	0.70	0.15	0.07	0.74	0.13	-0.05	0.68	0.17	0.000
Autumn (SON)	0.56	0.11	0.03	0.60	0.11	-0.03	0.43	0.11	-0.02
Annual mean	0.65	0.12	0.04	0.66	0.12	-0.04	0.61	0.12	-0.01

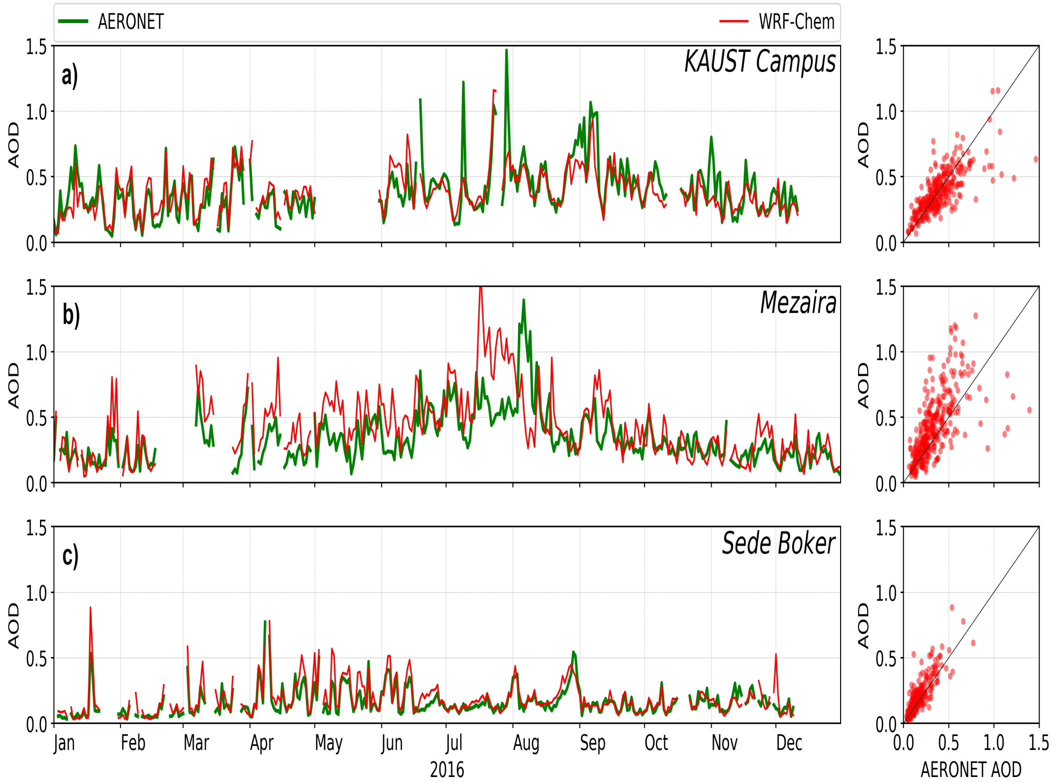

Figure 5: Observed AERONET and simulated WRF-Chem daily mean aerosol optical depth in 2016 for: a) KAUST Campus, b) Mezaira, and c) Sede Boker. The green curve shows AERONET AOD at 0.550 μm and the red curve shows model AOD at 0.6 μm. Scatter diagrams are shown on the right.

Figure 4c demonstrates that the simulated annual average volume PSD of DD (at the KAUST Campus), approximated by five bins, closely reflects that calculated using the observed PSD in Figure 4a. The coarse dust particles with 6 μm < r < 10 μm and giant dust particles with r > 10 μm contribute 27% and 57 % to observed DD, respectively. Figure 4d shows annual mean normalized (to 100%) volume PSDs of emitted dust, suspended in the atmosphere dust, and deposited dust simulated in this study. With the new settings, bin 5 contributes 73% to DE, 80% to DD, and 30% to dust atmospheric loading. The red bars in Figure 2 show the PSD of dust suspended in the atmosphere simulated in the current study when the model was simultaneously constrained by DD and AERONET AOD. With new settings, bin 5 (which also accounts for giant dust) is more pronounced, reflecting the large-radii tail of PSD that is not captured by AERONET retrieval (Figure 2). Overall, we conclude that the performance of the WRF-Chem tuned simultaneously by AOD and DD improved in comparison with our previous simulations, and it adequately represents the AOD and DD observations. Below, we use our model output to analyze the geographically distributed effects of dust in the ME in terms of its radiative impact on climate, DD rates, and deterioration of the efficacy of solar devices.

3.2 Radiative Effects of Coarse and Fine Dust

The radiative effects of dust particles suspended in the atmosphere are calculated using Mie theory because particles are sparse and distances between them are much larger than their sizes. Therefore, they do not interact optically, and their collective optical effect is a linear superposition of the effect of all individual particles. The optical properties of the individual particles are defined by their size, shape, and complex refractive index. The particles are most optically effective for the wavelengths comparable to their size. The complex part of the refractive index characterizes light absorption. Dust particles could effectively scatter and absorb solar radiation, which complicates the calculation and interpretation of their radiative effect.

3.2.1 AODs

Aerosol RF remains one of the largest uncertainties in future climate projections (Gliß et al., 2020). Dust RF depends on dust abundance, composition, and size distribution and is modulated by surface albedo (Osipov et al., 2015). In dust source regions like the ME, dust is particularly essential because of its widespread abundance. Evaluating the radiative effect of dust, we stepped ahead of the conventional approach in the analysis of AODs and RF by discriminating the effects of dust particles of different sizes. Coarse and fine dust particles have a different lifetime in the atmosphere, which controls how far from an emission source they can be transported by atmospheric airflow. In SW, finer dust particles are generally more optically active per unit mass compared to coarser particles.

In WRF-Chem, we calculated the contributions of each of the five aerosol bins (see Table 1) to optical depth and instantaneous RF. We specifically focused on the surface RF, as we were interested in the impact of dust on ground-based solar devices. We also compared the radiative effects of dust and non-dust aerosols. Figure 6 shows the visible (0.6 μm) optical depth produced by each dust bin and the total DOD. The finest dust bin 1 (0.1-1 μm), which comprises a relatively small mass, produces 45% of DOD, and bins 2 and 3 (1-3 μm) combined contribute about 42%. The optical depth of coarse dust in bin 5, which comprises the most dust mass (Figure 2), is 6% of total visible DOD.

Figure 7a shows the visible optical depth of non-dust aerosols that comprise the effects of sea salt over marine areas, biomass burning BC and OC mostly transported from Africa, and anthropogenic sulfate over the eastern Red Sea, Arabian Gulf, and Yemeni coastal areas and Oman. The high air pollution over the Arabian Sea originates from India and comprises a mixture of BC, OC, and sulfates/nitrates. The non-dust AOD is comparable with the DOD in coastal areas, but is much smaller than the DOD in the interior of the Arabian Peninsula.

Our results show a stronger dust contribution to AOD over the Arabian Sea and the Red Sea compared with previous studies (Myhre et al., 2013; Osipov et al., 2022). However, the aerosol effects are spatially variable and their contributions depend on the

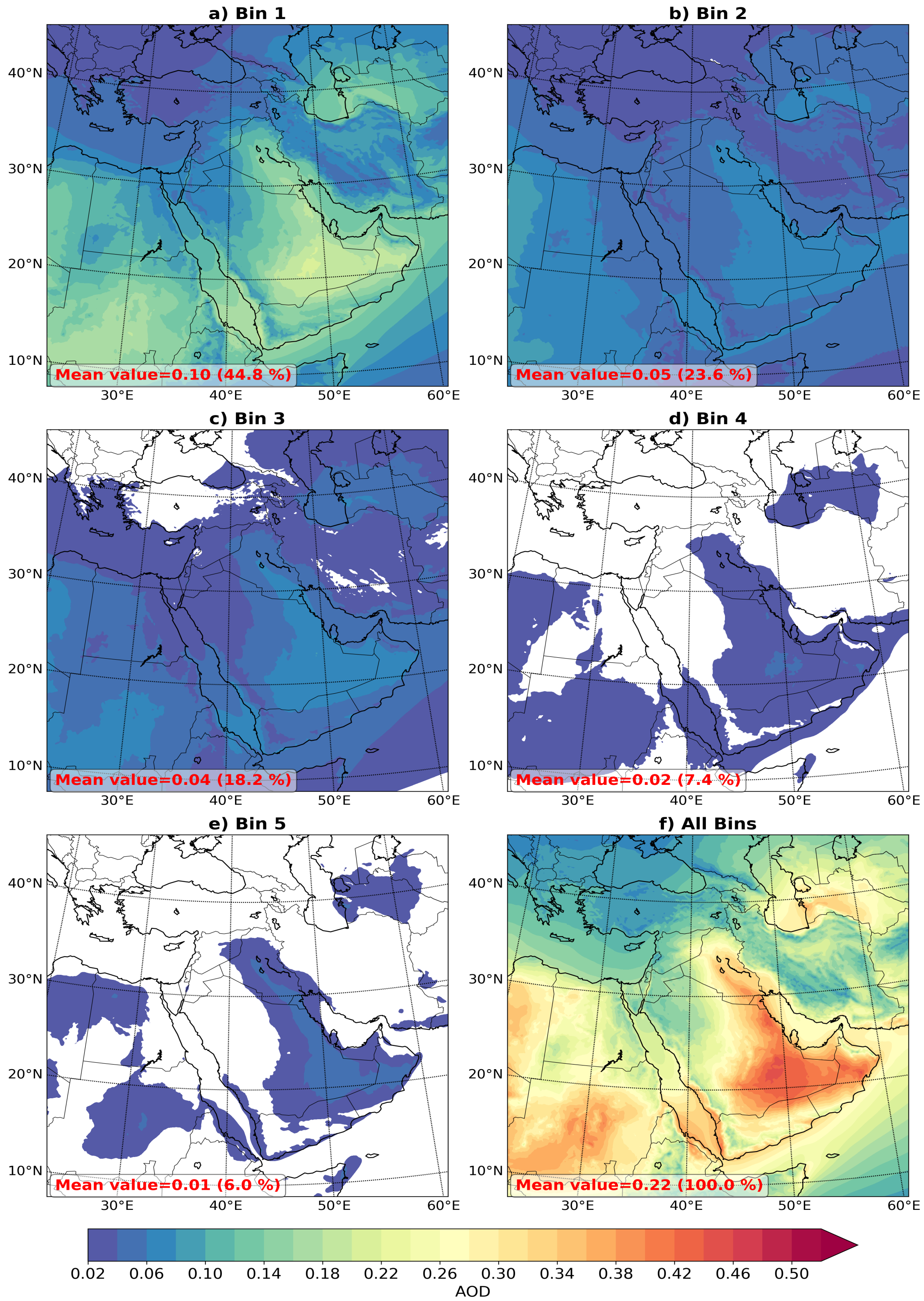

Figure 6: Annual mean visible DOD (0.6 μm) caused by individual bins and the total simulated in WRF-Chem with the DD constraints for 2016: a) Bin 1, b) Bin 2, c) Bin 3, d) Bin 4, e) Bin 5, and f) all Bins. The area average DODs and their relative contributions to each bin are shown at the bottom of each panel.

435 distribution of aerosol sources. For example, we observed that dust produces more than

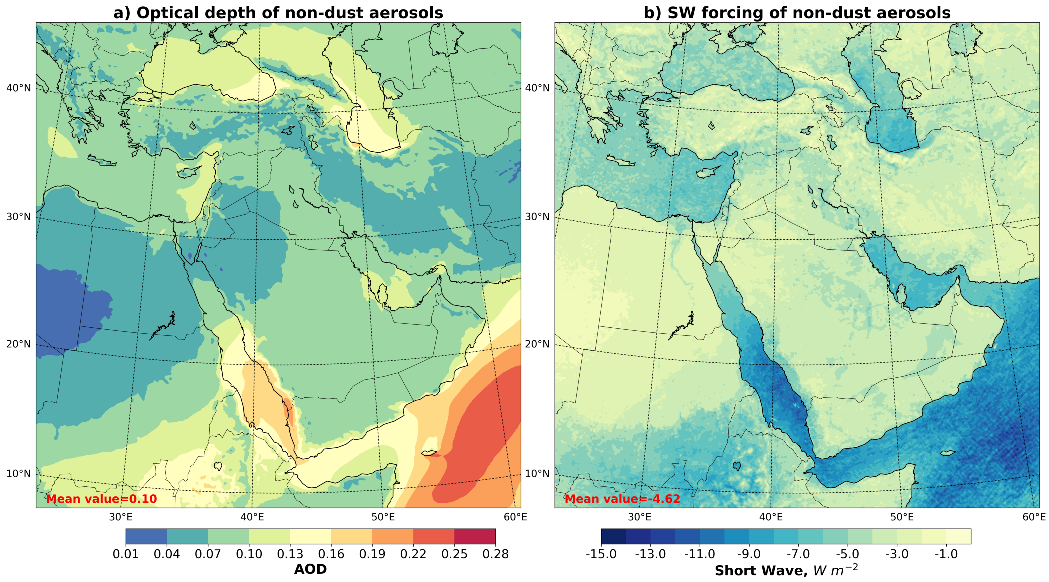

Figure 7: a) Annual mean non-dust visible optical depth, NOD at 0.6 μm calculated in WRF-Chem with the DD constraints for 2016; b) SW clear-sky radiative forcing ($W\ m^{-2}$) of non-dust aerosols at the surface calculated in WRF-Chem with the DD constraints for 2016. The area average NOD and RF are shown at the bottom of each panel.

80% of visible AOD in the interior regions of the Arabian Peninsula, where anthropogenic aerosol sources are weak compared to natural sources.

3.2.2 Aerosol Radiative Forcing

Fig. 8 presents the annual mean clear-sky direct instantaneous dust SW RF at the surface produced by each dust bin and the total. The radiative fluxes were obtained by double calls of radiative routine with and without the corresponding dust component. The radiative transfer calculations were conducted on the same meteorological fields (temperature and humidity). The RF was obtained as the difference between the net SW downward flux ($SW_{\downarrow} - SW_{\uparrow}$) in the calls with and without the corresponding dust bin. The dust total SW RF at the surface is negative, as dust absorbs and scatters SW radiation, thereby reducing solar radiation flux reaching the surface. The finest three bins with r $< 3\ \mu m$ contribute almost all of the RF. The contribution of the coarsest dust particles with r $> 6\ Wm^{-2}$ (represented by bin 5) in the total SW surface RF is about 7-8%, so the coarse dust SW radiative effect is relatively small, although it is not negligible. The total annual mean SW RF reaches -30 Wm^{-2} over the southern Red Sea. This area experiences one of the largest climatological forcings in the world (Osipov & Stenchikov, 2018). We also observe that the continental dust outflow generates high RF over the southern coast of the Arabian Peninsula and the Arabian Sea, reaching -20 Wm^{-2}. Over land, the RF peaks in the dust source areas, including Rub' al-Khali, the deserts in the eastern Arabian Peninsula, and the Red Sea coastal plain.

Fig. 9 shows clear-sky direct instantaneous dust LW RF at the surface for each bin and all bins. The LW RF, similar to the SW RF, is calculated using double calls of radiation routines. It is calculated as the difference between ($LW_{\downarrow} - LW_{\uparrow}$) flux with and without the corresponding dust component. Dust thermal radiation warms the surface, but the average magnitude over the domain LW warming is four times smaller compared to SW cooling. The largest LW effect is over land areas, caused predominantly by coarse dust, and the coarsest bin 5 contributes 26% of the LW radiative heating at the surface. However, the average over the domain LW surface heating is only 3.26 Wm^{-2}.

The instantaneous net (SW + LW) RF is shown in Fig. 10. This RF defines the effect of dust on the regional climate and reflects the spatial pattern of the SW RF. Fine bins are the major contributors. Averaged over the domain, the annual mean radiative cooling reaches 5.72 Wm^{-2}, but over the southern Red Sea it exceeds 20 Wm^{-2}. Dust bin 5 is the only bin that actually warms the surface. The SW and LW radiative effects of the coarsest bin almost cancel each other resulting in a 3.5% contribution to the net RF at the surface.

The non-dust aerosols mostly contribute to the SW RF (see Figure 7b), as their LW RF in the ME is negligible. Averaged over the domain, the SW RF of non-dust aerosols is twice as small (but still significant) compared to dust SW RF. The contribution of non-dust aerosols becomes more significant in the cities, the areas affected by industrial sulfur emissions, and over regional seas where the dust effect diminishes.

3.2.3 Test of the Radiative Effects of Coarse and Giant Dust Using Observed PSD

Following the approach used in (Adebiyi et al., 2023; Adebiyi & Kok, 2020), we used the PSD observed in the central part of the Arabian Peninsula (Pósfai et al., 2013) to calculate the contribution of coarse and giant dust particles in aerosol optical properties and RF and to test our model results discussed in the previous section. For this, we used a 1D standalone column model that employs Line-by-Line radiative transfer calculations (Mok et al., 2016; Osipov et al., 2020). A standalone modeling framework permits greater flexibility and higher accuracy of radiative transfer calculations than broadband radiative codes embedded in unwieldy and complex Global Circulation Models (GCMs). We employ a realistic PSD (Figure 11), which spans 0.05 μm < r < 30 μm. The size distribution was sampled in Riyadh on 9 April, 2007 during the Kingdom of Saudi Arabia Assessment of Rainfall Augmentation research program (Pósfai et al., 2013; Anisimov et al., 2018) after a typical mesoscale haboob dust storm event in the region (referred to hereafter as Riyadh PSD). It comprises a longer large-particle tail compared to other size distributions sampled in fair weather conditions (see Figure 16 in (Anisimov et al., 2018) and corresponding explanations). The instrument counts aerosol particles at the immediate entrance of the inlet, so the loss of large particles should be low (Pósfai et al., 2013). During the campaign, the research aircraft followed a spiral trajectory, sampling the entire dust profile in the troposphere. We took advantage of the vertical sampling to derive and employ the column-integrated PSD.

Compared with the recent airborne campaigns in the Sahara (see Figure 4 in (Adebiyi et al., 2023)), the Riyadh PSD falls within the envelope of dust size distributions obtained in SAMUM1 and SAMUM2 campaigns and is similar to AER-D size distribution with the maximum at 7 μm. The Riyadh PSD, similar to the bulk of Saharan size distributions, has a less pronounced relative contribution of the super-coarse particles (10 μm $< r < 30\mu m$) than the Fennec PSD (Ryder et al., 2019). The dust particles with r > $30\mu m$ were not measured during the Riyadh campaign.

The RF of dust, including its sensitivity to various parameters, has been studied extensively using 1D models (e.g., Figure 16 in (Osipov et al., 2015)). Instead, here we quantify the relative contribution of dust particles of various sizes to the optical depth τ and RF (defined as a difference ΔF of surface radiative fluxes calculated with and without dust effect) via diagnostics similar to the cumulative distribution function (CDF):

$$\tau_{CDF}(r^*) = \frac{\tau(r^*)}{\tau} \tag{2}$$

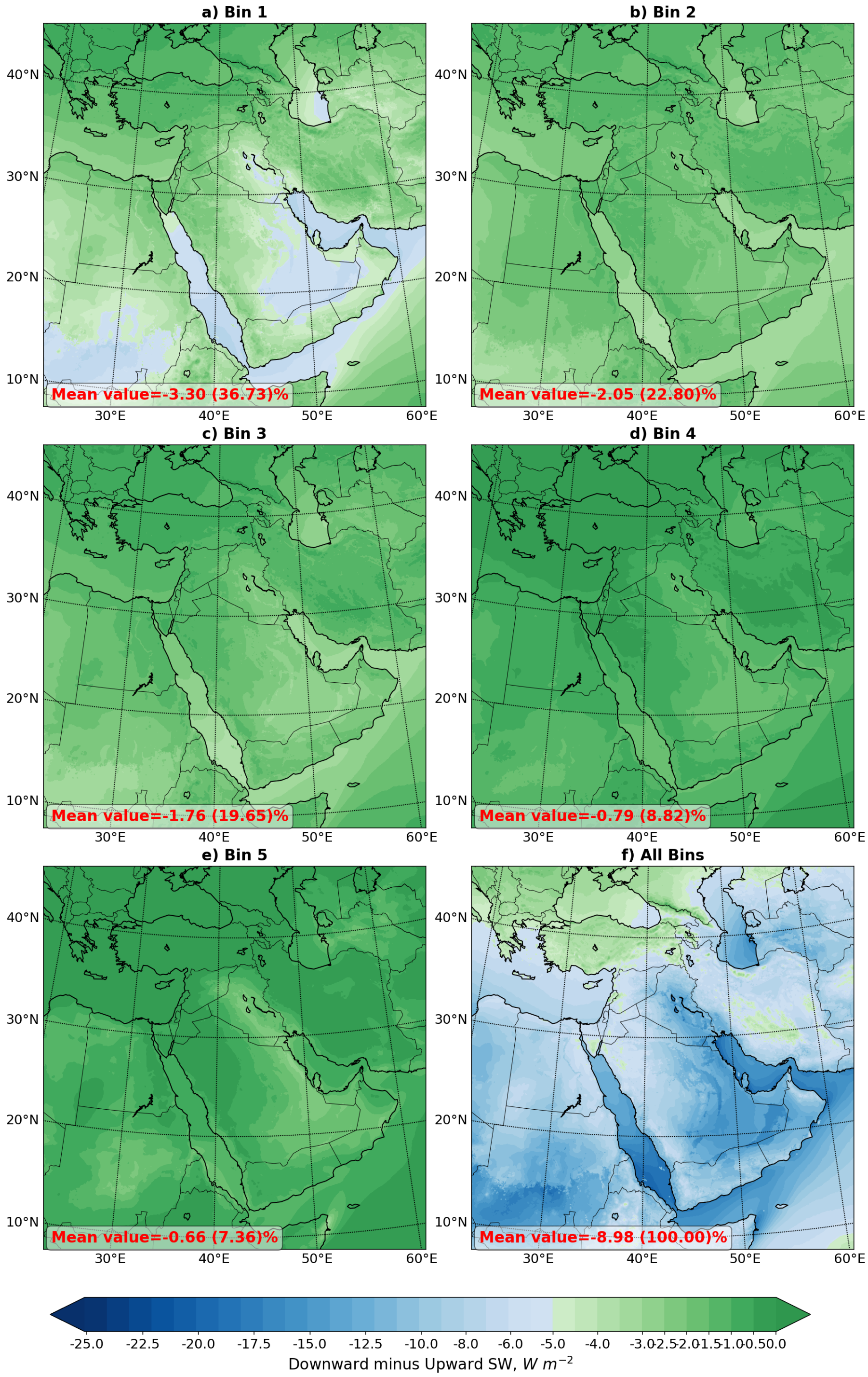

Figure 8: Annual mean clear-sky SW dust radiative forcing ($W\ m^{-2}$) at the surface caused by the individual bins and total calculated in WRF-Chem with the DD constraints for 2016: a) Bin 1, b) Bin 2, c) Bin 3, d) Bin 4, e) Bin 5, and f) all Bins. The area average forcing and relative contributions of each bin are shown at the bottom of each panel.

$$\Delta F_{CDF}(r^*) = \frac{\Delta F(r^*)}{\Delta F} \tag{3}$$

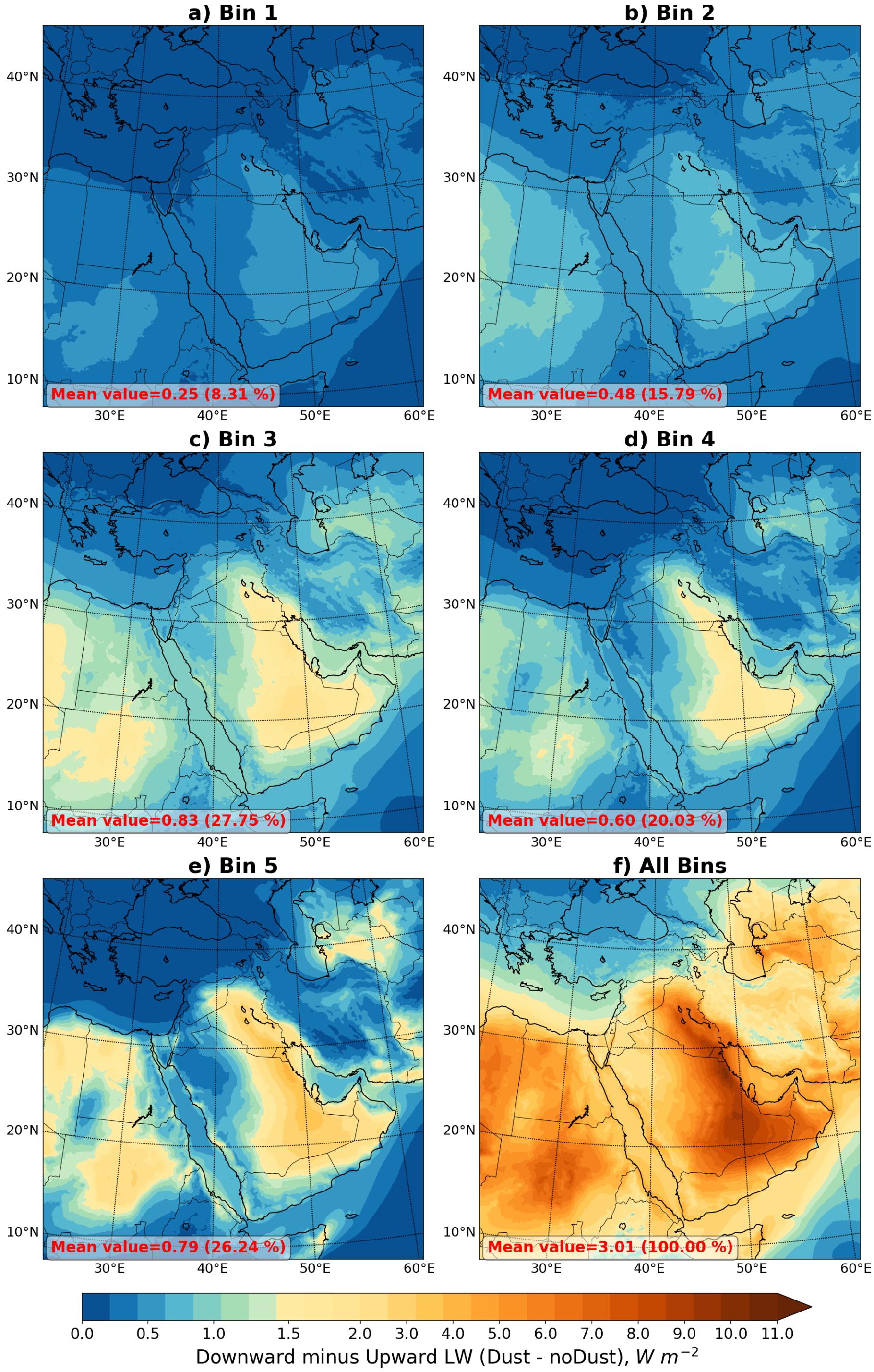

Figure 9: Annual mean clear-sky LW dust radiative forcing (Wm^{-2}) at the surface caused by the individual bins and calculated in WRF-Chem with the DD constraints for 2016: a) Bin 1, b) Bin 2, c) Bin 3, d) Bin 4, e) Bin 5, and f) all Bins. The area average forcing and relative contributions of each bin are shown at the bottom of each panel.

where $\tau(r^*)$ and $\Delta F(r^*)$ are the SW or LW optical depth and RF generated by dust particles with r < r*, respectively. In equation (2), the partial RF in the numerator (which

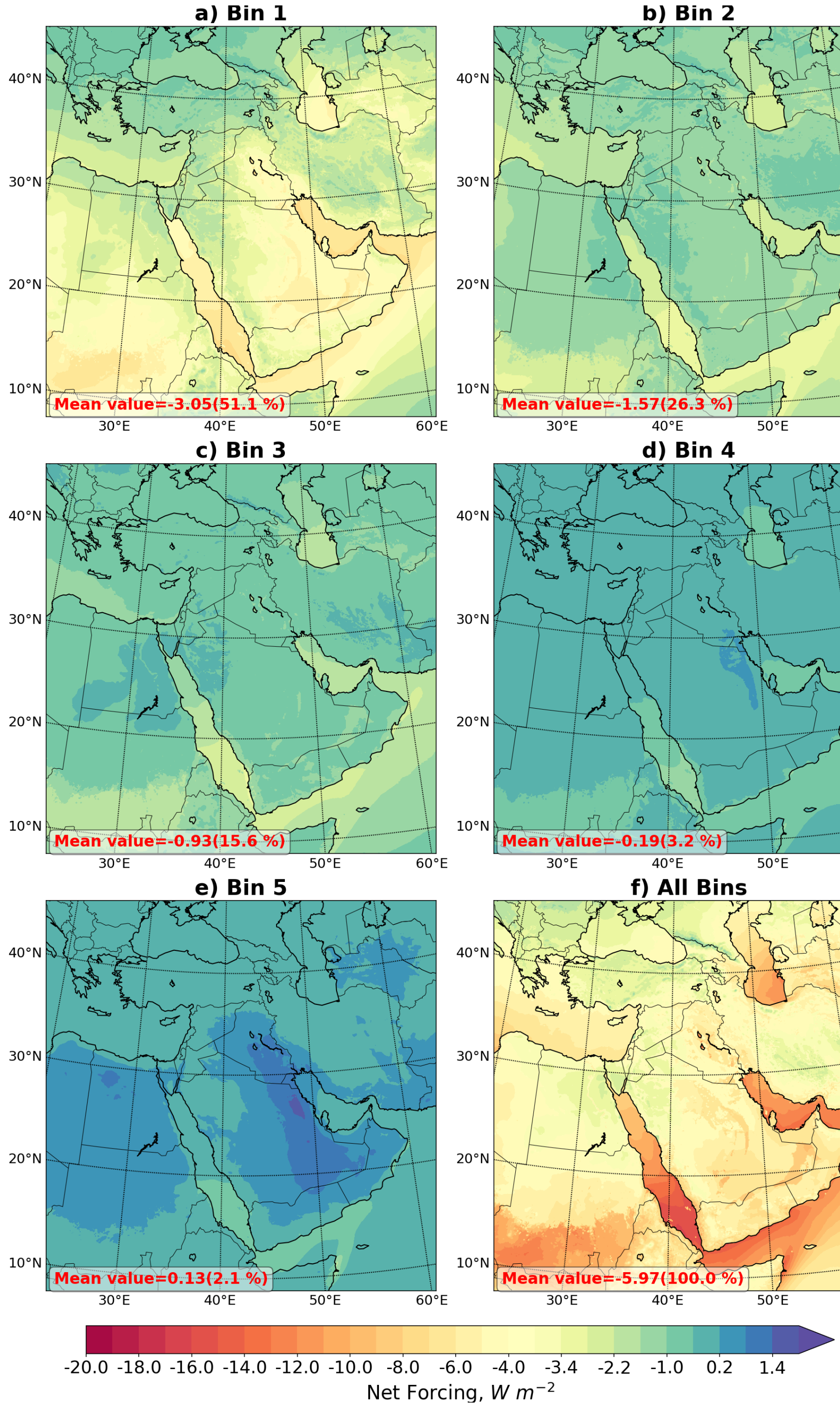

Figure 10: Annual mean clear-sky net (SW+LW) dust radiative forcing ($W\ m^{-2}$) at the surface caused by the individual bins and total calculated in WRF-Chem with the DD constraints for 2016: a) Bin 1, b) Bin 2, c) Bin 3, d) Bin 4, e) Bin 5, and f) all Bins. The area average RF and relative contributions of each bin are shown at the bottom of each panel.

accounts only for a fraction of dust particles with $r < r^*$) is normalized by the total RF

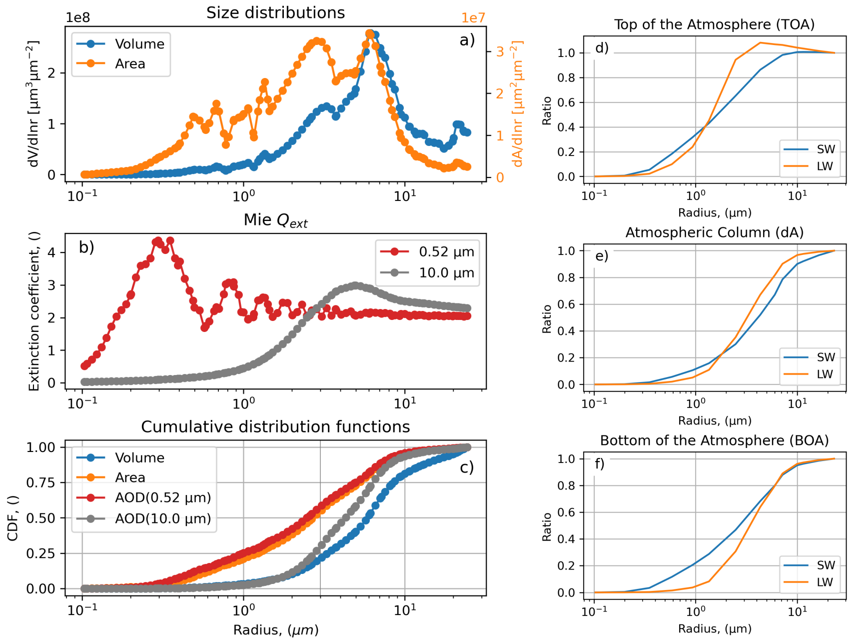

Figure 11: Size-resolved microphysical and optical properties of dust, and the RF. The left column shows: a) dust volume size distribution and surface area; b) SW and LW extinction cross-sections; and c) cumulative distribution functions of the dust total volume, surface area, and AOD (bottom). The cumulative distribution functions of volume, surface area, and AOD are normalized (to their maximum value) to show the relative contribution of all the particles in the size distribution up to the radius r. The right column shows the relative contribution of dust particles up to radius r to dust SW and LW RFs (i.e., ΔF_{CDF} in equation 2) at the d) top of the atmosphere (TOA), f) the bottom of the atmosphere (BOA) and e) dust absorption within the atmospheric column (dA).

(integrated over the entire radii range), which results in a relative contribution of dust particles up to a size r* (normalized CDF). Similarly, we define the CDFs of the aerosol optical properties: extinction coefficients ϵ, ϵ_{CDF}, scattering coefficient ϵ_S, single scattering albedo ω_{CDF}:

$$\epsilon(r^*) = \int_0^{r^*} Q(r)\frac{dN}{dr}\,dr \tag{4}$$

$$\epsilon_S(r^*) = \int_0^{r^*} Q_S(r)\frac{dN}{dr}\,dr \tag{5}$$

$$\tau(r^*) = \int_0^{\infty} \epsilon(r^*)\,dz \tag{6}$$

$$\omega_{CDF}(r^*) = \epsilon_S(r^*)/\epsilon(r^*) \tag{7}$$

$$\epsilon_{CDF}(r^*) = \frac{\int_0^{r^*} Q(r)\frac{dN}{dr}\,dr}{\int_0^{\infty} Q(r)\frac{dN}{dr}\,dr} \tag{8}$$

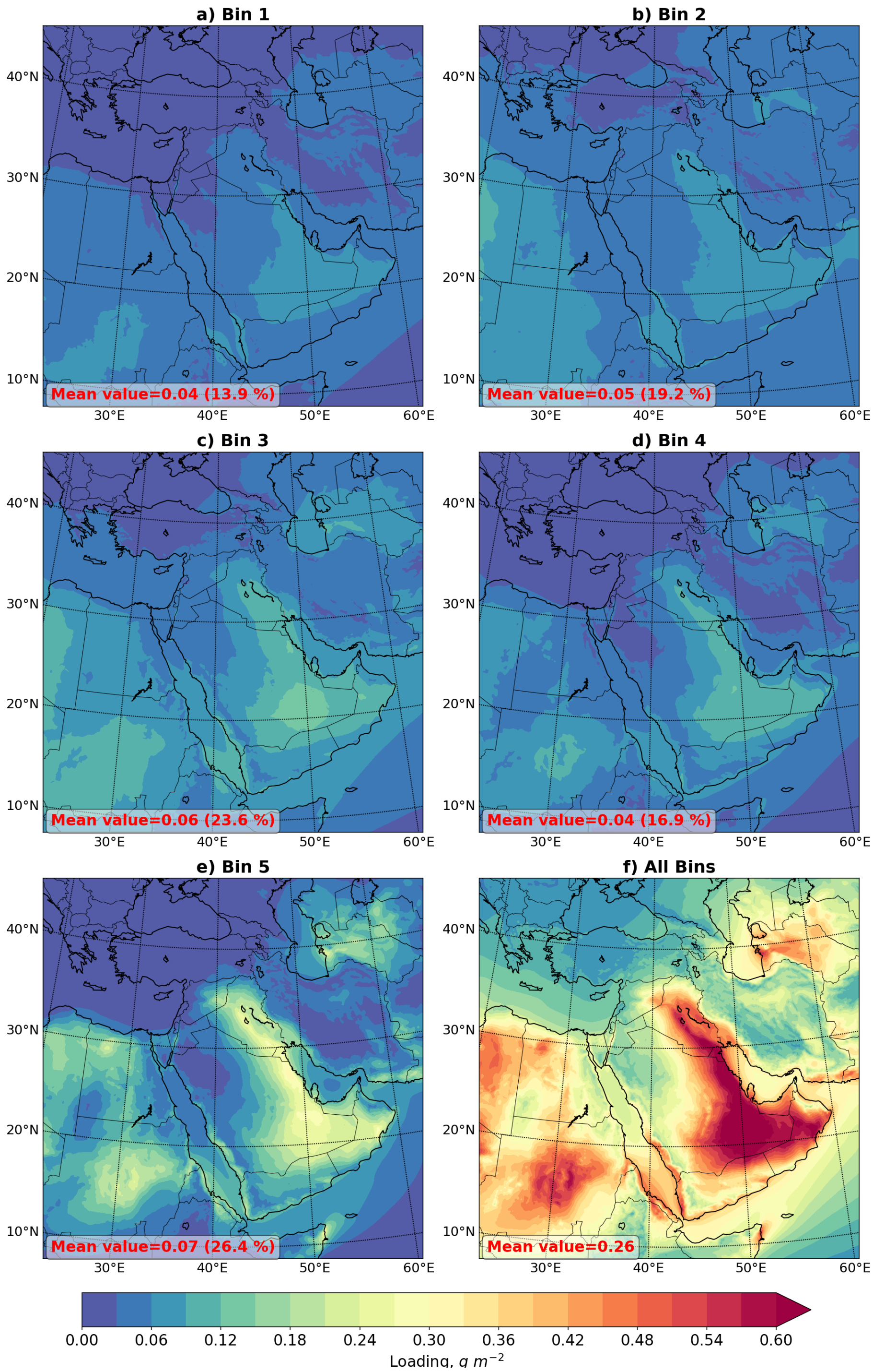

Figure 12: Annual mean column integrated dust concentration, DL ($g\ m^{-2}$) of the individual dust bins and total calculated in WRF-Chem with the DD constraints for 2016: a) Bin 1, b) Bin 2, c) Bin 3, d) Bin 4, e) Bin 5, and f) all Bins. The area average values for each bin and their relative contributions are shown at the bottom of each panel.

where $Q(r)$ and $Q_S(r)$ are the extinction and scattering cross-sections for individual particles with radius r. dN/dr is number-density dust PSD. The spectral dust optical properties (Figure S1) and corresponding CDFs (Figure S2) are available in the Supplementary section.

The standalone 1D analysis (Figure 11a-c) corroborates the conclusions of the WRF-Chem modeling. We resolve the contributions of dust particles of various sizes to the physical, optical, and radiative properties of atmospheric dust. In particular, we found that fine dust with $r < 3\mu m$ constitutes 20% of the total mass but more than 50% of the total cross-section and surface area (i.e., the properties that modulate the radiative transfer and heterogeneous chemistry on the surface of the particles), 60% of the visible DOD, and 25% of DOD in LW. Dust with r $< 10\mu m$ explains 75% of the dust loading in the column and $>$ 90% of the 0.52 μm and 10 μm AODs. Furthermore, the particles with $r > 3\mu m$ explain 75% of DOD in longwave.

Figure 11d-f confirms that giant dust particles with r $>$ 10 μm contribute less than 10% in the SW and LW ΔF_{CDF} either at the top of the atmosphere (TOA), the bottom of the atmosphere (BOA), or atmospheric absorption (dA). Dust particles with 6 $\mu m <$ r $<$ 10 μm, for which the radiative effect was virtually absent previously due to model error, account for 10% of the surface SW and LW RFs, relevant for the impact on solar panels, and 5-7% of SW and LW dA, relevant for the climate and circulation effects. Large particles with r $>$ 6 μm, that are now represented in bin 5, account for at least 40% of total dust mass suspended in the atmosphere, which is consistent with our results (see Figure 4d) showing that bin 5 accounts for about 30% of dust mass suspended in the atmosphere (at the KAUST Campus). The dust SW and LW RFs tend to cancel each other out at the surface, but SW and LW dust absorption in the atmosphere enhances each other, thus producing stronger atmospheric warming.

3.3 Effect of Fine and Coarse Dust on DE, DD, and DL

Dust is generated across almost the entire Arabian Peninsula, where the source function $S > 0$ (see Figure 1). The most intensive dust generation occurs in the eastern and south-eastern parts of the Arabian Peninsula, where S reaches its maximum value of 0.45. In the absence of rain, dry deposition and gravitational sedimentation are the primary mechanisms of dust deposition in desert regions (Mahowald et al., 2011; Adebiyi et al., 2023).

Fig. 12 shows column-integrated atmospheric DL for each bin and all bins. The distribution of all-bin loading is similar to that of DOD. The larger total loadings up to 0.6 $g\ m^{-2}$ are observed in the eastern Arabian Peninsula, the Rub Al Khali desert, and the southern Red Sea. The domain average annual mean loading in different bins varies from 0.04 gm^{-2} (in bin 1) to 0.07 gm^{-2} in bin 5. Bin 5, representing coarse and giant dust with r $>$ 6 μm, incorporates 26% of total DL (consistent with (J. Meng et al., 2022; Kok et al., 2021; Adebiyi & Kok, 2020; Adebiyi et al., 2023)), although it receives 73% of total DE. The gravitational settling of coarse dust particles in bin 5 is so rapid that few remain suspended in the atmosphere even over the regions where they are generated in large quantities (eastern Arabian Peninsula, Rub Al Khali desert), confirming that DL is less sensitive to the emission of coarse and giant particles than, for example, DD.

The mean seasonal dust emission rates averaged over the dust source regions (i.e., Arabian Peninsula, Central Asia and Iran, and East Africa, excluding the seas) is shown in Figure 13. The largest DE is in Spring and Summer. The Arabian Peninsula and East Africa emit twice as much dust compared to the Central Asia and Iran regions. In Summer, the Arabian Peninsula emits more dust than other sub-regions within the domain because the northwesterly winds, Shamal, that blow over the Arabian Peninsula cause frequent dust outbreaks (Rashki et al., 2019; Yu et al., 2016; Patlakas et al., 2019). The Central Asia and Iran sub-region exhibits the maximum emission rate in summer (28.8 $Mt\ mo^{-1}$) and minimum in winter (20.5 $Mt\ mo^{-1}$). The annual dust emission from the entire domain tripled in our current simulations in comparison with those not accounting for the generation of giant dust particles.

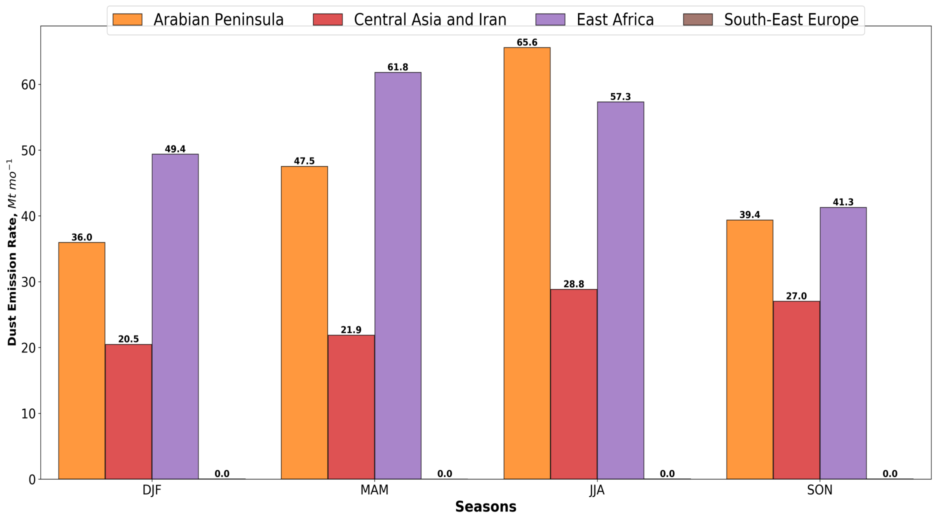

Figure 13: Seasonal mean dust emission rates ($Mt\ mo^{-1}$) calculated in WRF-Chem with the DD constraints for 2016 for four seasons (DJF, MAM, JJA, SON) integrated over the selected sub-regions: Arabian Peninsula (light brown), central Asia and Iran (red), east Africa (violet), and south-east Europe (dark brown bar is too small to be visible).

Figure S3 (see the supplementary information) shows the spatial distribution of dust deposition over the Arabian Peninsula for four seasons. Consistent with the seasonal pattern of DE, the largest seasonally integrated DD occurs in summer and spring. Overall, dust deposition rates in the eastern Arabian Peninsula are much higher than in the western Arabian Peninsula. The largest simulated deposition rates are observed in Oman, exceeding 20 $g\ m^{-2}\ mo^{-1}$, which is at least three times higher than in the Red Sea coastal plain.

Figure 14 shows the spatial distribution of the annual mean deposition over the Arabian Peninsula produced by dust from different bins. Annually, 446 Mt of dust is deposited in the Arabian Peninsula, with bin 5 being a major contributor (377 Mt). Fine particles in bins 1 and 2 (r $< 1.8\ \mu m$) are deposited almost uniformly over the entire region. Most of the coarse particles in bin 5, however, deposit close to the source regions where they were emitted, resembling the spatial patterns of the source function S (see Fig. 1). However, we also observe significant deposition of coarse and giant particles in the regional seas.

Dust deposition plays a key role in the geochemical cycles in the oceans and seas (Fan et al., 2006; Martin, 1990; Sunda & Huntsman, 1997; Watson et al., 2000; Mahowald et al., 2011). The dust released into the ocean feeds marine ecosystems and increases their productivity. The chemicals brought by dust deposition are particularly important in seas with little perennial freshwater discharge, such as the Red Sea (Jish Prakash et al., 2015).

Figure S4 (see the supplementary information) shows the seasonal spatial distribution of dust deposited in the Red Sea. The maximum deposition rate (5-6 $g\ m^{-2}\ mo^{-1}$) occurred within 10 km of the coastline due to proximity to dust sources. Away from the coast, except during summer in the southern Red Sea, the rate of dust deposition de-

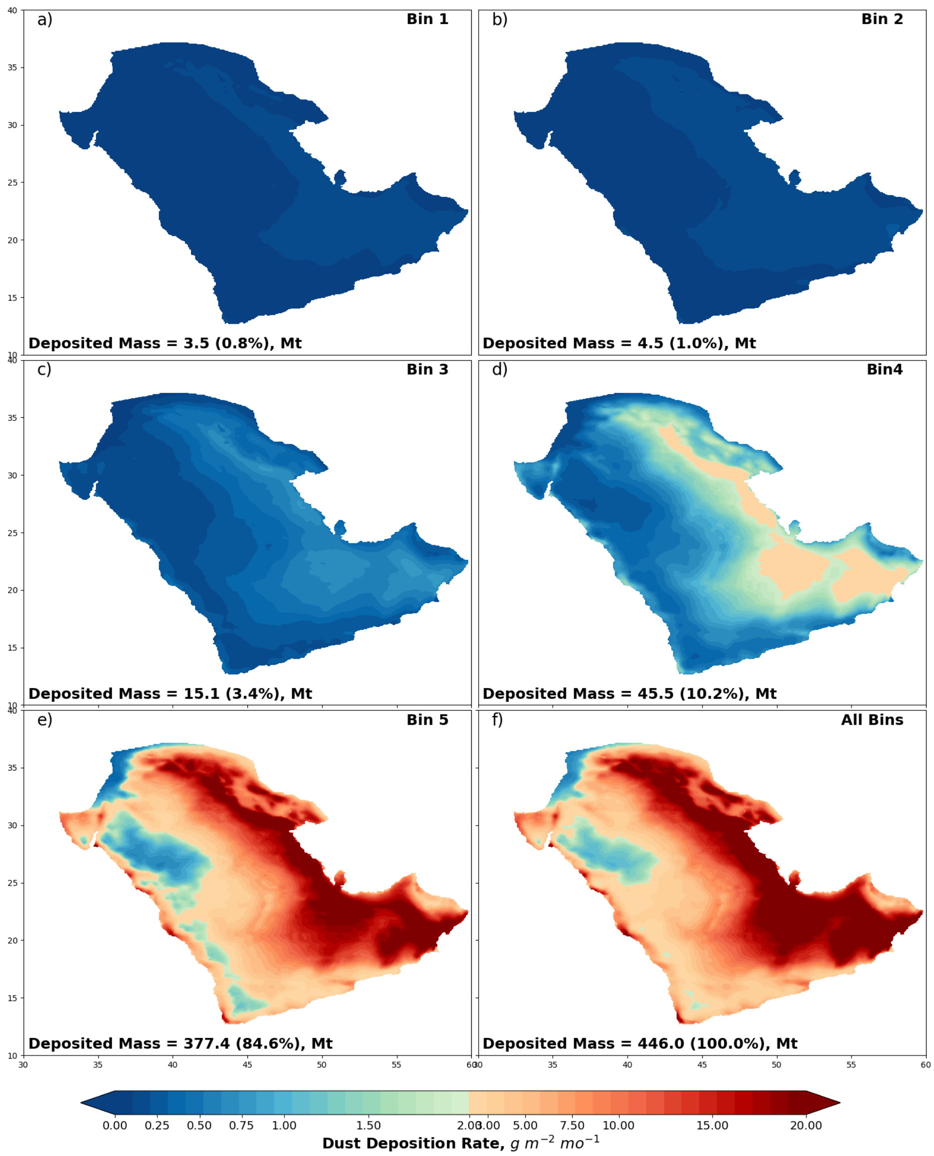

Figure 14: Annual mean dust deposition rate $g\ m^{-2}\ mo^{-1}$ calculated in WRF-Chem with the DD constraints for 2016 over the Arabian Peninsula caused by the individual and total: a) Bin 1; b) Bin 2; c) Bin 3; d) Bin 4; e) Bin 5; and f) all Bins. The spatially integrated mass of deposited dust for each bin and its relative contribution are shown in each panel at the bottom.

creases. The maximum dust deposition in the Red Sea (7.9 Mt) occurs in the months June-August (JJA; see Figure S4c) when the north African monsoonal circulation transports dust from Africa's Bodele Depression through the Tokar Mountain Gap (Kalenderski & Stenchikov, 2016). The Northerly winds, prevailing in Summer, push dust to the southern Red Sea where it is trapped by high coastal mountain ranges so that AOD reaches 1 (Osipov & Stenchikov, 2018). The minimum DD over the Red Sea is observed in Fall (SON), when it decreases to 3.2 Mt.

The annual average DD rates in the Red Sea for the individual bins and total are shown in Figure 15. The total annual DD in the Red Sea is 19.8 Mt, predominantly produced by dust in bin 5 (15.3 Mt). The deposition rate of coarse particles is 3-4 times smaller in central sea compared to the near-shore areas. The fine particles in bins 1 and 2 contribute 4% of deposited mass, which is uniformly distributed over the Red Sea area. The total DD rate varies from 7 $g\ m^{-2}\ mo^{-1}$ near the coasts to 1 $g\ m^{-2}\ mo^{-1}$ in the central Red Sea, which is hardly reachable by coarse dust. Overall, giant dust deposition in the Red Sea is 2.5 times higher when compared with simulations without DD tuning (Shevchenko et al., 2021).

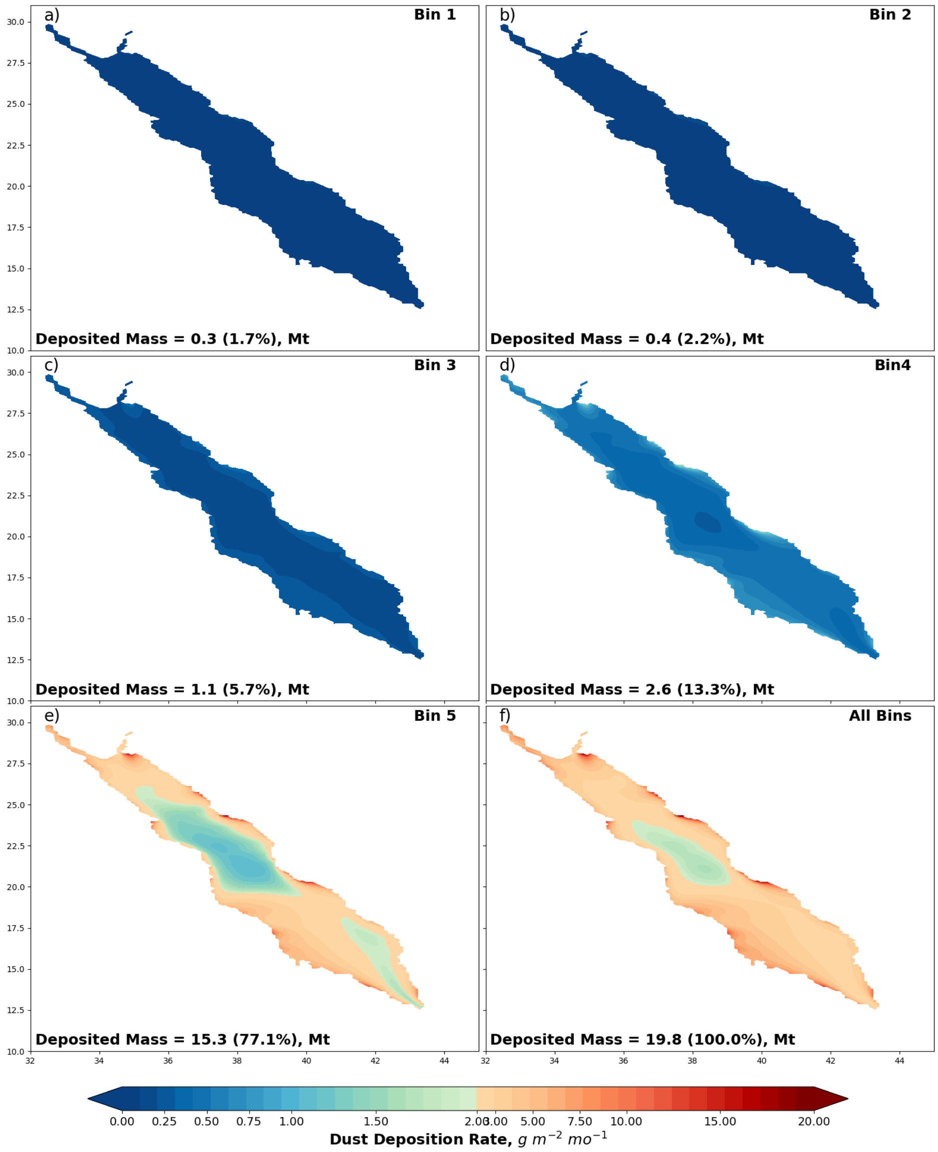

Figure 15: Annual mean dust deposition rate ($g\ m^{-2}\ mo^{-1}$) in the Red Sea calculated in WRF-Chem with the DD constraints for 2016 caused by the individual dust bins and total: a) Bin 1; b) Bin 2; c) Bin 3; d) Bin 4; e) Bin 5; and f) all Bins. The spatially integrated mass of deposited dust for each bin and its relative contribution is shown in each panel at the bottom.

The seasonal spatial deposition rate over the Arabian Gulf is shown in Figure S5 (see the supplementary information). The maximum deposition is observed in summer (JJA - Figure S5c), reaching 5.5 Mt. Deposition reduces to a minimum of 2.1 Mt in winter (DJF - Figure. S5a). The maximum dust deposition rates, similar to the Red Sea, are along the coastlines in the vicinity of the primary dust sources. The Arabian Gulf receives dust from the eastern Arabian Peninsula, Iraq, the Omani coast, and the western part of Iran.

Figure 16 shows the spatial distribution of annual dust deposition over the Arabian Gulf contributed by the different bins and total, which is 14.1 Mt. The total annual average deposition rate varies from 10 $g\ m^{-2}\ mo^{-1}$ in the north-western and western coastal areas to 1.0 $g\ m^{-2}\ mo^{-1}$ in the central Arabian Gulf (Figure 16f). This deposition rate is about 25% higher than in the Red Sea. Similarly to the Red Sea, the coarse dust particles in bin 5 contribute 76.1% to the dust deposition, and the finest bins 1 and 2 contribute only 3.5%.

Annual deposition over the Arabian Sea within our computational domain is about 14 Mt, with an average rate of 4.9 $g\ m^{-2}\ mo^{-1}$. However, in summer, there are areas with a dust deposition rate above 34.2 $g\ m^{-2}\ mo^{-1}$ located in the northwestern Arabian Sea and along its northern coastline caused by the seasonal intensification of local north-westerly winds and Indian Monsoon circulation. In addition, the Somali jet associated with the southwestern Indian monsoon transports dust from Somalia's deserts to the Arabian Sea in summer (Tindale & Pease, 1999).

Figure 17 shows seasonal deposition rates averaged over the selected regions indicating contributions of coarse dust. In all seasons over land (excluding the southeast Europe region), coarse and giant dust comprises more than 90% of the total deposited dust mass. Over the regional seas, however, fine dust contribution is more than 20%. Thus, the relative contribution of fine dust to DD is twice as large over the seas as the land areas because coarse dust particles predominantly deposit in the coastal areas.

4 Impact of Coarse and Fine Dust on Solar Devices

The Middle East receives a huge amount of solar radiation. For example, the 500× 500 km^2 area in the Saudi desert receives enough solar energy to cover the entire global energy consumption. Dust, however, could significantly hamper the efficiency of solar devices and must be accounted for.

Dust and other aerosols have two main impacts on solar devices. Firstly, aerosols suspended in the atmosphere attenuate solar radiation reducing the downward solar flux at the surface by 12 $W\ m^{-2}$ on average (see Fig. 18). Secondly, dust and other aerosols deposit on the optically active surfaces of solar devices, causing power loss due to soiling (Ilse, Figgis, Werner, et al., 2018; Ilse et al., 2016; Ilse, Figgis, Naumann, et al., 2018; Figgis et al., 2017; Baras et al., 2016; Boyle et al., 2013; Sayyah et al., 2014)

We define the effect of dust as the relative energy loss due to dust deposited on the surfaces of a solar device, e.g., solar PV panels, or because dust attenuates the incoming solar flux when suspended in the atmosphere. Considering the solar devices with a constant radiation-to-electricity conversion coefficient, we can formulate the losses as a relative decrease of incoming solar radiation caused by dust. Thus soiling losses (SL) and attenuation losses (AL) could be calculated in the following way:

$$SL = \frac{E_0 - E_s}{E_0} \times 100\% = \frac{\Delta E_s}{E_0} \times 100\% \tag{9}$$

$$AL = \frac{E_0 - E_a}{E_0} \times 100\% = \frac{\Delta E_a}{E_0} \times 100\% \tag{10}$$

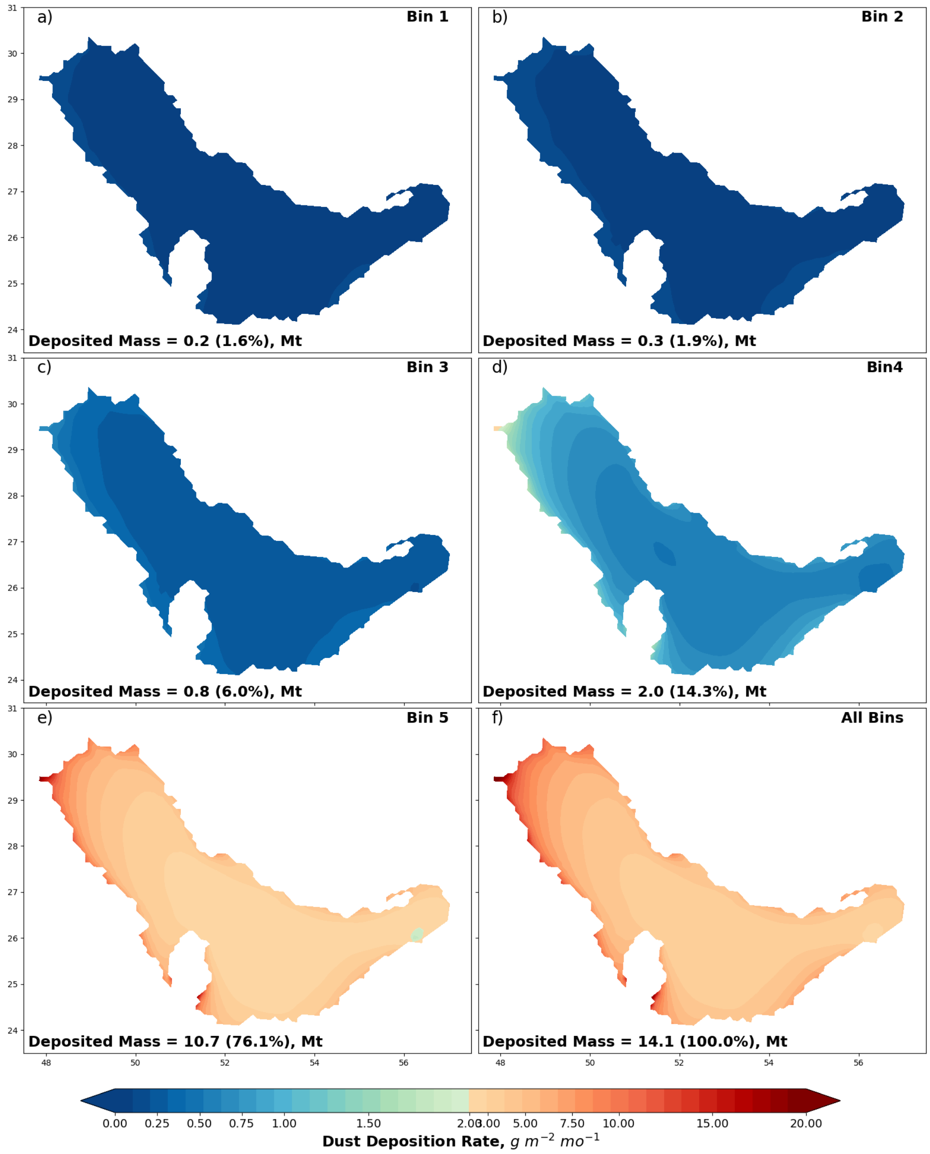

Figure 16: Annual mean dust deposition rate ($g\ m^{-2}\ mo^{-1}$) in the Arabian Gulf calculated in WRF-Chem with the DD constraints for 2016 caused by the individual dust bins and total: a) Bin 1; b) Bin 2; c) Bin 3; d) Bin 4; e) Bin 5; and f) all Bins. The spatially integrated mass of deposited dust for each bin and its relative contribution is shown in each panel at the bottom.

where E_0, E_s, and E_a are, respectively, daily solar energy received by a clean device in a clean atmosphere, the soiled device in a clean atmosphere, and a clean device in a dusty atmosphere. ΔE_s and ΔE_a are, respectively, the solar energy loss due to soiling and attenuation.

The total loss (TL) can be calculated as the sum of soiling and attenuation losses:

$$TL = SL + AL \tag{11}$$

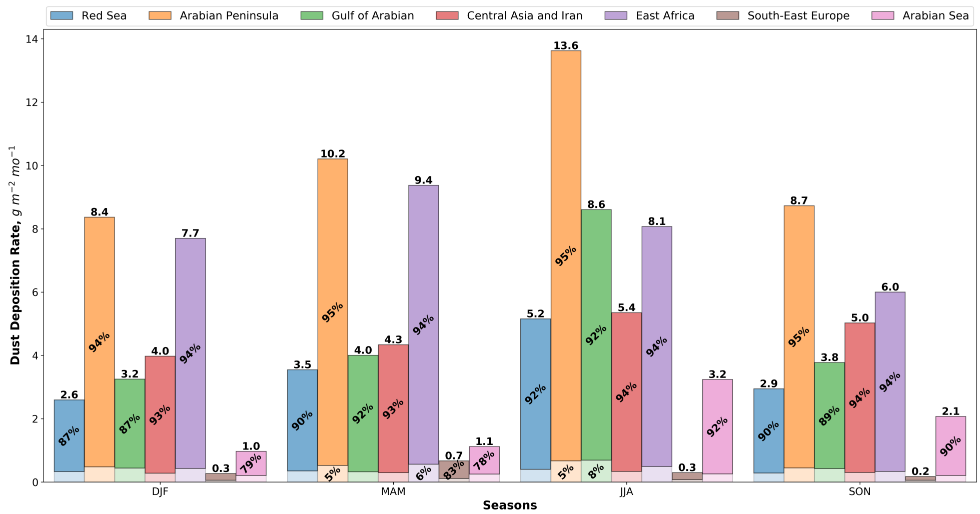

Figure 17: Seasonal mean dust deposition rate ($g\ m^{-2}\ mo^{-1}$) in the seven selected regions calculated in WRF-Chem with the DD constraints for 2016. From bottom to top, the color grading shows the contribution of fine (sum of bins 1-3) and coarse (sum of bins 4-5) dust particles (see Table 1).

Here, we use the assessments of dust radiative effect and DD rates obtained in this study to estimate SL and AL. Figure 18 demonstrates the effect of dust on the downward solar flux at the surface. The average change of solar radiation over the domain is 12.13 $W\ m^{-2}$, but locally it reaches 30 $W\ m^{-2}$. The finest three bins with r < 3 μm produce about 90% of this effect. Thus, the average daily attenuation loss in the chosen domain $AL = 4.75\%$ but locally exceeds 11 %. Specifically, for the KAUST site in summer, this is $AL = 5\%$ (see Figure 18a).

Soiling losses depend on the amount of deposited dust. Our analysis shows that coarse dust comprises most of the deposited mass. Valerino et al. (2020) conducted a comprehensive analysis, measuring soiling loss per unit deposited mass. According to their measurements conducted in Gandhinagar (Gujarat, India), soiling loss is 5-6% per 1 $g\ m^{-2}$ of material deposited on the PV surfaces. This is a useful way to assess soiling, allowing us to scale the soiling loss against corresponding deposition rates.

To interpret their results, Valerino et al. (2020) assumed that the radiative effect of aerosols deposited on the surface of a PV panel would be the same as if they were suspended in the atmosphere. This assumption led to the conclusion that fine particles produce the greatest soiling effect. However, deposited particles are densely packed on the surface of a PV panel, and the Mie theory assumptions (large distances between particles preventing their optical interactions), assumed by Valerino et al. (2020), cannot be satisfied. Here, we suggest a different physical model, assuming that deposited particles make a uniform layer over a solar panel surface. Knowing the refractive index of deposited material, we can calculate the SL per unit deposited mass of 1 $g\ m^{-2}$.

In our simulations, the main deposited material is dust with density $d = 2500\ kg\ m^{-3}$, and refractive index.

$$R_i = n + i \times \chi \tag{12}$$

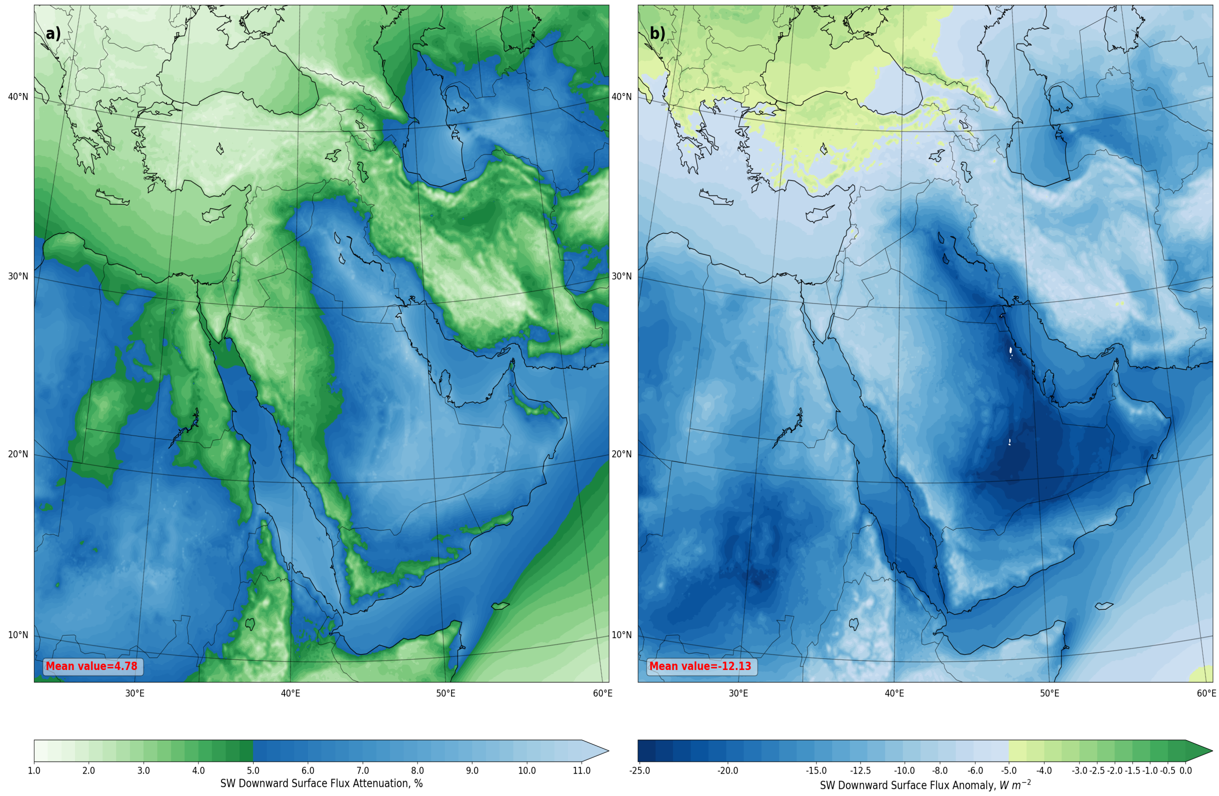

Figure 18: Annual mean dust-caused downward SW radiative flux anomaly at surface calculated in WRF-Chem with the AOD and DD constraints for 2016. a) Normalized to its annual mean value (%); b) Absolute value ($W\ m^{-2}$) The spatially averaged value is shown at the bottom of the panel.

Where the real part of the refractive index is $n = 1.55$, and the imaginary part is $\chi = 0.003$. The depth of the deposited layer with a mass of 1 $g\ m^{-2}$ $h = 0.4\ \mu m$, the following relation gives us the soiling loss (Landau et al., 2013):

$$SL = \frac{4\pi n \chi h}{\lambda} \times 100\% \tag{13}$$

where λ is a characteristic wavelength of solar light. Assuming $\lambda = 0.55\ \mu m$ for the most energetic visible light, we obtain $SL = 4.25\%$, consistent with the measurements conducted by Valerino et al. (2020). However, in this case, we have to conclude that the largest contribution to soiling is from large particles that comprise most of the deposited mass.

The deposition of dust particles on the surface of a PV panel is a complex process that depends on meteorological conditions (Ilse, Figgis, Naumann, et al., 2018), the tilt of a panel (Boyle et al., 2013), dust mineralogy (Engelbrecht et al., 2017), the presence of water, and adhesion forces between a panel and dust particles (Ilse, Figgis, Naumann, et al., 2018). The detailed analysis of these processes is beyond the scope of this paper, but we can estimate the upper limit of the soiling effect. We assume that a PV panel is oriented horizontally and all deposited material is retained on its surface. The average deposition, e.g., at the KAUST site, is about 3 $qm^{-2}week^{-1}$ (Shevchenko et al., 2021). Therefore, the average soiling loss $SL = 12.75\%$ for a weekly cleaning schedule assumes linear dependence of SL on the deposited mass and temporarily uniform accumulation of material on PV surfaces. Accounting for the attenuation losses $AL = 5\%$, we can expect that the total loss of efficiency of the solar panels on the west coast of Saudi Arabia (on a weekly cleaning schedule) would be $TL = 17 - 18\%$ for the areas similar to the KAUST campus. According to our simulations, the deposition rates on the east coast of the Arabian Peninsula are at least three times higher than on the west coast. Therefore, for those areas, the dust-related losses could be projected to TL=45% (assuming a weekly cleaning schedule).

5 Conclusions

In desert regions like the ME, dust is an important climate factor as it significantly attenuates solar radiation at the surface and heats the atmospheric column (Osipov et al., 2015). We evaluated the radiative dust effect and deposition rates in the ME using the free-running WRF-Chem model.

Observations show that large particles with r > 10 μm contribute the most mass in dust deposition. However, the deposited dust mass was underestimated by 2-3 times because the up-to-date models (free-running and used in data assimilation) underrepresented the content of coarse and giant dust in the atmosphere. Therefore, we approximate the effect of giant dust with r > 10 μm by increasing the emission of coarse particles in bin 5 with 6 μm < r < 10 μm. This approach compensates for the suspected model overestimation of the giant dust deposition rate. For the first time, we simultaneously constrained the model simulations by DD and AERONET AOD observations by using dust deposition observations collected on the Red Sea coast with passive dust deposition samplers (Shevchenko et al., 2021). We specifically quantified the effect of dust particles of different sizes on dust RF and mass deposition.

The annual mean area average reduction of SW surface flux reaches 9 $W\ m^{-2}$, but regionally solar surface cooling exceeds 30 $W\ m^{-2}$. Dust-induced LW warming partly compensates for SW cooling so that domain averaged dust annual mean net RF is reduced to - 5.72 $W\ m^{-2}$, but regionally net radiative cooling reaches 20 $W\ m^{-2}$. Annually, non-dust aerosols contribute, on average, about 20% to AOD and RF over land. In the urban centers and areas affected by sulfur emissions and sea salt intrusions, however, the non-dust aerosols' contribution to solar flux reduction increases to > 30%. Fine dust particles with radii r < 3 μm produce about 90% of the net clear-sky SW RF at the surface, while the SW contribution of the coarsest particles with r > 6 μm is < 10%. Conversely, giant and coarse particles dominate the effect on DD and DE. Accounting for giant dust particles and simultaneously fitting the DD and visible AOD observations led to a tripling of DE compared to the simulations without the DD constraints; consequently, DD increases over land 3 times and over regional seas 2.5 times. The fine dust deposition fraction (compared to the coarse dust fraction) in the seas is twice as large than over land because most of the coarse dust particles deposit within the narrow coastal area.

Dust suspended in the atmosphere significantly affects the functioning of solar devices by reducing the downward solar flux and efficacy of solar panels by an average of 5% over the domain. Dust deposition on solar devices is another factor that affects their functionality. Based on the annual average dust deposition rate, the soiling losses could reach 12% per week on the west coast and could be up to three times higher on the East Coast. Fine dust is predominantly responsible for solar light attenuation, but coarse dust particles play a major role in deposition and soiling.

Fitting visible AOD helps to constrain the emission of fine dust, whereas fitting DD constrains the emission of coarse dust. Approximating the giant dust with coarse dust leads to marginally stronger cooling in SW and a slight overestimation of warming in LW (see Figure 11). The SW and LW effects of giant dust almost cancel each other out at the surface, but their SW and LW absorption in the atmosphere enhance their heating of the atmospheric column. Overall, our results are consistent with recent studies (J. Meng et al., 2022; Kok et al., 2017; Adebiyi et al., 2023) and highlight that coarse dust particles underrepresented in the up-to-date models contribute to atmospheric loading by about 25%. At the same time, we found that DD and DE triple in the experiments constrained by AOD and DD, while the radiative effect of giant dust does not exceed 10%. Accounting for giant dust, as suggested in this study, allows us to reach an agreement between the model results and the available observations. Dust deposition data appear to be a valuable asset that, together with AOD, allows model performance to be rectified. Expansion of the network of dust deposition observations is necessary to improve dust modeling and forecasting further.

Acknowledgments

The research reported in this publication was supported by funding from King Abdullah University of Science and Technology (KAUST) through the Competitive Research Grant (URF/1/2180-01-01) “Combined Radiative and Air Quality Effects of Anthropogenic Air Pollution and Dust over the Arabian Peninsula,” and the ACWA Power industrial grant RGC/3/5274-01-01 "Development of a Soiling Map for the GCC region." This research used the resources of the Supercomputing Laboratory at KAUST.

References

Abdou, W. A., Diner, D. J., Martonchik, J. V., Bruegge, C. J., Kahn, R. A., Gaitley, B. J., … Holben, B. (2005). Comparison of coincident multiangle imaging spectroradiometer and moderate resolution imaging spectroradiometer aerosol optical depths over land and ocean scenes containing aerosol robotic network sites. *Journal of Geophysical Research: Atmospheres*, *110*(D10).

Adebiyi, A., Kok, J., Murray, B., Ryder, C., Stuut, J., Kahn, R., … others (2023). *A review of coarse mineral dust in the earth system* (Vol. 60). Elsevier.

Adebiyi, A., & Kok, J. F. (2020). Climate models miss most of the coarse dust in the atmosphere. *Science advances*, *6*(15), eaaz9507.

Anisimov, A., Axisa, D., Kucera, P. A., Mostamandi, S., & Stenchikov, G. (2018). Observations and cloud-resolving modeling of haboob dust storms over the arabian peninsula. *Journal of Geophysical Research: Atmospheres*, *123*(21), 12–147.

Balkanski, Y., Schulz, M., Claquin, T., & Guibert, S. (2007). Reevaluation of mineral aerosol radiative forcings suggests a better agreement with satellite and aeronet data. *Atmospheric Chemistry and Physics*, *7*(1), 81–95.

Baras, A., Jones, R. K., Alqahtani, A., Alodan, M., & Abdullah, K. (2016). Measured soiling loss and its economic impact for pv plants in central saudi arabia. In *2016 saudi arabia smart grid (sasg)* (pp. 1–7).

Bergametti, G., & Forêt, G. (2014). *Dust deposition.* Springer.

Bergin, M. H., Ghoroi, C., Dixit, D., Schauer, J. J., & Shindell, D. T. (2017). Large reductions in solar energy production due to dust and particulate air pollution. *Environmental Science & Technology Letters*, *4*(8), 339–344.

Boucher, O., Pham, M., & Venkataraman, C. (2002). *Simulation of the atmospheric sulfur cycle in the laboratoire de météorologie dynamique general circulation model: Model description, model evaluation, and global and european budgets.* Inst. Pierre Simon Laplace des Sciences de l'Environnement Global.

Boyle, L., Flinchpaugh, H., & Hannigan, M. (2013). Impact of natural soiling on the transmission of pv cover plates. In *2013 ieee 39th photovoltaic specialists conference (pvsc)* (pp. 3276–3278).

Boyle, L., Flinchpaugh, H., & Hannigan, M. (2015). Natural soiling of photovoltaic cover plates and the impact on transmission. *Renewable Energy*, *77*, 166–173.

Bozzo, A., Remy, S., Benedetti, A., Flemming, J., Bechtold, P., Rodwell, M., & Morcrette, J.-J. (2017). *Implementation of a cams-based aerosol climatology in the ifs.* European Centre for Medium-Range Weather Forecasts.

Buchard, V., Randles, C., Da Silva, A., Darmenov, A., Colarco, P., Govindaraju, R., … others (2017). The merra-2 aerosol reanalysis, 1980 onward. part ii: Evaluation and case studies. *Journal of Climate*, *30*(17), 6851–6872.

Cakmur, R., Miller, R., Perlwitz, J., Geogdzhayev, I., Ginoux, P., Koch, D., … Zender, C. (2006). Constraining the magnitude of the global dust cycle by minimizing the difference between a model and observations. *Journal of Geophysical Research: Atmospheres*, *111*(D6).

Chadwick, O. A., Derry, L. A., Vitousek, P. M., Huebert, B. J., & Hedin, L. O. (1999). Changing sources of nutrients during four million years of ecosystem development. *Nature*, *397*(6719), 491–497.

Chin, M., Diehl, T., Tan, Q., Prospero, J. M., Kahn, R. A., Remer, L. A., … Zhao, X.-P. (2014). Multi-decadal aerosol variations from 1980 to 2009: a perspective from observations and a global model. *Atmospheric Chemistry and Physics*, *14*(7), 3657–3690. Retrieved from `https://www.atmos-chem-phys.net/14/3657/2014/` doi: 10.5194/acp-14-3657-2014

Chin, M., Ginoux, P., Kinne, S., Torres, O., Holben, B. N., Duncan, B. N., … Nakajima, T. (2002). Tropospheric aerosol optical thickness from the gocart model and comparisons with satellite and sun photometer measurements. *Journal of the atmospheric sciences*, *59*(3), 461–483.

Chin, M., Rood, R. B., Lin, S.-J., Müller, J.-F., & Thompson, A. M. (2000). Atmospheric sulfur cycle simulated in the global model gocart: Model description and global properties. *Journal of Geophysical Research: Atmospheres*, *105*(D20), 24671–24687.

Climate.com. (2018). *Climate of middle east.* Author. Retrieved from `http://climateof.com/middleeast/index.asp`

Darmenova, K., Sokolik, I. N., Shao, Y., Marticorena, B., & Bergametti, G. (2009). Development of a physically based dust emission module within the weather research and forecasting (wrf) model: Assessment of dust emission parameterizations and input parameters for source regions in central and east asia. *Journal of Geophysical Research: Atmospheres*, *114*(D14).

DeMott, P. J., Prenni, A. J., Liu, X., Kreidenweis, S. M., Petters, M. D., Twohy, C. H., ... Rogers, D. (2010). Predicting global atmospheric ice nuclei distributions and their impacts on climate. *Proceedings of the National Academy of Sciences*, *107*(25), 11217–11222.

Dubovik, O., & King, M. D. (2000). A flexible inversion algorithm for retrieval of aerosol optical properties from sun and sky radiance measurements. *Journal of Geophysical Research: Atmospheres*, *105*(D16), 20673–20696.

El-Shobokshy, M. S., & Hussein, F. M. (1993). Degradation of photovoltaic cell performance due to dust deposition on to its surface. *Renewable energy*, *3*(6-7), 585–590.

Engelbrecht, J. P., Stenchikov, G., Prakash, P. J., Lersch, T., Anisimov, A., & Shevchenko, I. (2017). Physical and chemical properties of deposited airborne particulates over the arabian red sea coastal plain. *Atmospheric Chemistry and Physics*, *17*(18), 11467–11490.

Fan, S.-M., Moxim, W. J., & Levy, H. (2006). Aeolian input of bioavailable iron to the ocean. *Geophysical Research Letters*, *33*(7).

Figgis, B., Ennaoui, A., Ahzi, S., & Rémond, Y. (2017). Review of pv soiling particle mechanics in desert environments. *Renewable and Sustainable Energy Reviews*, *76*, 872–881.

Forster, P., Ramaswamy, V., Artaxo, P., Berntsen, T., Betts, R., Fahey, D. W., ... others (2007). Changes in atmospheric constituents and in radiative forcing. chapter 2. In *Climate change 2007. the physical science basis.* WMO.

Ginoux, P., Chin, M., Tegen, I., Prospero, J. M., Holben, B., Dubovik, O., & Lin, S.-J. (2001). Sources and distributions of dust aerosols simulated with the gocart model. *Journal of Geophysical Research: Atmospheres*, *106*(D17), 20255–20273.

Ginoux, P., Prospero, J. M., Gill, T. E., Hsu, N. C., & Zhao, M. (2012). Global-scale attribution of anthropogenic and natural dust sources and their emission rates based on modis deep blue aerosol products. *Reviews of Geophysics*, *50*(3).

Gliß, J., Mortier, A., & Schulz, M. (2020). Multi-model evaluation of aerosol optical properties in the aerocom phase iii control experiment, using ground and space based observations from aeronet, modis, aatsr and a merged satellite product as well as surface in-situ observations from gaw sites. In *Egu general assembly conference abstracts* (p. 18390).

Grell, G. A., & Dévényi, D. (2002). A generalized approach to parameterizing convection combining ensemble and data assimilation techniques. *Geophysical Research Letters*, *29*(14), 38–1.

Grell, G. A., Peckham, S. E., Schmitz, R., McKeen, S. A., Frost, G., Skamarock, W. C., & Eder, B. (2005). Fully coupled "online" chemistry within the wrf model. *Atmospheric Environment*, *39*(37), 6957–6975.

Hamidi, M., Kavianpour, M. R., & Shao, Y. (2013). Synoptic analysis of dust storms in the middle east. *Asia-Pacific Journal of Atmospheric Sciences*, *49*(3), 279–286.

Highwood, E., & Ryder, C. (2014). *Mineral dust: A key player in the earth sys-*

tem edited by p knippertz and jb stuut. Dordrecht: Springer) Radiative effects of dust.

Hong, S., Dudhia, J., & Noh, Y. (2003). A new vertical diffusion package with explicit treatment of the entrainment processes, extended abstract. In *International workshop on numerical weather forecast models, japan.*

Huneeus, N., Schulz, M., Balkanski, Y., Griesfeller, J., Prospero, J., Kinne, S., ... others (2011). Global dust model intercomparison in aerocom phase i. *Atmospheric Chemistry and Physics*, *11*(15), 7781–7816.

Iacono, M., Levinson, D., & El-Geneidy, A. (2008). Models of transportation and land use change: A guide to the territory. *Journal of Planning Literature*, *22*(4), 323–340.

Ilse, K., Figgis, B. W., Naumann, V., Hagendorf, C., & Bagdahn, J. (2018). Fundamentals of soiling processes on photovoltaic modules. *Renewable and Sustainable Energy Reviews*, *98*, 239–254.

Ilse, K., Figgis, B. W., Werner, M., Naumann, V., Hagendorf, C., Pöllmann, H., & Bagdahn, J. (2018). Comprehensive analysis of soiling and cementation processes on pv modules in qatar. *Solar Energy Materials and Solar Cells*, *186*, 309–323.

Ilse, K., Werner, M., Naumann, V., Figgis, B. W., Hagendorf, C., & Bagdahn, J. (2016). Microstructural analysis of the cementation process during soiling on glass surfaces in arid and semi-arid climates. *physica status solidi (RRL)–Rapid Research Letters*, *10*(7), 525–529.

Janssens-Maenhout, G., Pagliari, V., Guizzardi, D., & Muntean, M. (2013). Global emission inventories in the emission database for global atmospheric research (edgar)–manual (i). *Gridding: EDGAR emissions distribution on global gridmaps, Publications Office of the European Union, Luxembourg*.

Jish Prakash, P., Stenchikov, G., Kalenderski, S., Osipov, S., & Bangalath, H. (2015). The impact of dust storms on the arabian peninsula and the red sea. *Atmospheric Chemistry and Physics*, *15*(1), 199–222.

Jish Prakash, P., Stenchikov, G., Tao, W., Yapici, T., Warsama, B., & Engelbrecht, J. P. (2016). Arabian red sea coastal soils as potential mineral dust sources. *Atmospheric Chemistry and Physics*, *16*(18), 11991–12004.

Kalenderski, S., & Stenchikov, G. (2016). High-resolution regional modeling of summertime transport and impact of african dust over the red sea and arabian peninsula. *Journal of Geophysical Research: Atmospheres*, *121*(11), 6435–6458.

Kalenderski, S., Stenchikov, G. L., & Zhao, C. (2013). Modeling a typical wintertime dust event over the arabian peninsula and the red sea. *Atmospheric Chemistry and Physics*.

Knippertz, P., & Stuut, J.-B. W. (2014). Mineral dust. *Mineral dust—A key player in the Earth system*, 121–147.

Kok, J. F. (2011). Does the size distribution of mineral dust aerosols depend on the wind speed at emission? *Atmospheric Chemistry and Physics*, *11*(19), 10149–10156.

Kok, J. F., Adebiyi, A. A., Albani, S., Balkanski, Y., Checa-Garcia, R., Chin, M., ... others (2021). Contribution of the world's main dust source regions to the global cycle of desert dust. *Atmospheric Chemistry and Physics*, *21*(10), 8169–8193.

Kok, J. F., Ridley, D., Zhou, Q., Miller, R., Zhao, C., Heald, C., ... Haustein, K. (2017). *Smaller desert dust cooling effect estimated from analysis of dust size and abundance* (Vol. 10) (No. 4). Nature Geoscience.

Landau, L. D., Bell, J. S., Kearsley, M., Pitaevskii, L., Lifshitz, E., & Sykes, J. (2013). *Electrodynamics of continuous media* (Vol. 8). elsevier.

Levy, R., Hsu, C., et al. (2015). Modis atmosphere l2 aerosol product. *NASA MODIS Adaptive Processing System, Goddard Space Flight Center, USA, doi*,

10.
Madronich, S. (1987). Photodissociation in the atmosphere: 1. actinic flux and the effects of ground reflections and clouds. *Journal of Geophysical Research: Atmospheres*, *92*(D8), 9740–9752.
Maghami, M. R., Hizam, H., Gomes, C., Radzi, M. A., Rezadad, M. I., & Hajighorbani, S. (2016). Power loss due to soiling on solar panel: A review. *Renewable and Sustainable Energy Reviews*, *59*, 1307–1316.
Mahowald, N., Ward, D. S., Kloster, S., Flanner, M. G., Heald, C. L., Heavens, N. G., ... Chuang, P. Y. (2011). Aerosol impacts on climate and biogeochemistry. *Annual review of environment and resources*, *36*, 45–74.
Mallet, M., Tulet, P., Serça, D., Solmon, F., Dubovik, O., Pelon, J., ... Thouron, O. (2009). Impact of dust aerosols on the radiative budget, surface heat fluxes, heating rate profiles and convective activity over west africa during march 2006. *Atmospheric Chemistry and Physics*, *9*(18), 7143–7160.
Mani, M., & Pillai, R. (2010a). Impact of dust on solar photovoltaic (pv) performance: Research status, challenges and recommendations. *Renewable and Sustainable Energy Reviews*, *14*(9), 3124 - 3131. Retrieved from `http://www.sciencedirect.com/science/article/pii/S1364032110002455` doi: https://doi.org/10.1016/j.rser.2010.07.065
Mani, M., & Pillai, R. (2010b). Impact of dust on solar photovoltaic (pv) performance: Research status, challenges and recommendations. *Renewable and sustainable energy reviews*, *14*(9), 3124–3131.
Marticorena, B., & Bergametti, G. (1995). Modeling the atmospheric dust cycle: 1. design of a soil-derived dust emission scheme. *Journal of geophysical research: atmospheres*, *100*(D8), 16415–16430.
Martin, J. H. (1990). Glacial-interglacial co2 change: The iron hypothesis. *Paleoceanography*, *5*(1), 1–13.
McConnell, C., Formenti, P., Highwood, E., & Harrison, M. (2010). Using aircraft measurements to determine the refractive index of saharan dust during the dodo experiments. *Atmospheric Chemistry and Physics*, *10*(6), 3081–3098.
Meng, J., Huang, Y., Leung, D. M., Li, L., Adebiyi, A. A., Ryder, C. L., ... Kok, J. F. (2022). Improved parameterization for the size distribution of emitted dust aerosols reduces model underestimation of super coarse dust. *Geophysical research letters*, *49*(8), e2021GL097287.
Meng, Z., & Lu, B. (2007). Dust events as a risk factor for daily hospitalization for respiratory and cardiovascular diseases in minqin, china. *Atmospheric environment*, *41*(33), 7048–7058.
Miller, R., & Tegen, I. (1998). Climate response to soil dust aerosols. *Journal of climate*, *11*(12), 3247–3267.
Mlawer, E., & Clough, S. (1998). Shortwave and longwave enhancements in the rapid radiative transfer model. In *Proceedings of the 7th atmospheric radiation measurement (arm) science team meeting* (pp. 409–413).
Mlawer, E. J., Taubman, S. J., Brown, P. D., Iacono, M. J., & Clough, S. A. (1997). Radiative transfer for inhomogeneous atmospheres: Rrtm, a validated correlated-k model for the longwave. *Journal of Geophysical Research: Atmospheres*, *102*(D14), 16663–16682.
Mok, J., Krotkov, N. A., Arola, A., Torres, O., Jethva, H., Andrade, M., ... others (2016). Impacts of brown carbon from biomass burning on surface uv and ozone photochemistry in the amazon basin. *Scientific reports*, *6*(1), 1–9.
Morcrette, J.-J., Boucher, O., Jones, L., Salmond, D., Bechtold, P., Beljaars, A., ... others (2009). Aerosol analysis and forecast in the european centre for medium-range weather forecasts integrated forecast system: Forward modeling. *Journal of Geophysical Research: Atmospheres*, *114*(D6).
Mostamandi, S., Predybaylo, E., Osipov, S., Zolina, O., Gulev, S., Parajuli, S., & Stenchikov, G. (2022). Sea breeze geoengineering to increase rainfall over the

arabian red sea coastal plains. *Journal of Hydrometeorology*, *23*(1), 3–24.

Myhre, G., Myhre, C., Samset, B., & Storelvmo, T. (2013). Aerosols and their relation to global climate and climate sensitivity. *Nature Education Knowledge*, *4*(5), 7.

Osipov, S., Chowdhury, S., Crowley, J. N., Tadic, I., Drewnick, F., Borrmann, S., … others (2022). Severe atmospheric pollution in the middle east is attributable to anthropogenic sources. *Communications Earth & Environment*, *3*(1), 1–10.

Osipov, S., & Stenchikov, G. (2018). Simulating the regional impact of dust on the middle east climate and the red sea. *Journal of Geophysical Research: Oceans*, *123*(2), 1032–1047.

Osipov, S., Stenchikov, G., Brindley, H., & Banks, J. (2015). Diurnal cycle of the dust instantaneous direct radiative forcing over the arabian peninsula. *Atmospheric Chemistry and Physics*, *15*(16), 9537–9553.

Osipov, S., Stenchikov, G., Tsigaridis, K., LeGrande, A. N., & Bauer, S. E. (2020). The role of the so radiative effect in sustaining the volcanic winter and soothing the toba impact on climate. *Journal of Geophysical Research: Atmospheres*, *125*(2), e2019JD031726.

Parajuli, S. P., Stenchikov, G. L., Ukhov, A., Mostamandi, S., Kucera, P. A., Axisa, D., … Zhu, Y. (2022). Effect of dust on rainfall over the red sea coast based on wrf-chem model simulations. *Atmospheric Chemistry and Physics*, *22*(13), 8659–8682.

Patlakas, P., Stathopoulos, C., Flocas, H., Kalogeri, C., & Kallos, G. (2019). Regional climatic features of the arabian peninsula. *Atmosphere*, *10*(4), 220.

Pósfai, M., Axisa, D., Tompa, É., Freney, E., Bruintjes, R., & Buseck, P. R. (2013). Interactions of mineral dust with pollution and clouds: An individual-particle tem study of atmospheric aerosol from saudi arabia. *Atmospheric Research*, *122*, 347–361.

Prospero, J. M., Blades, E., Naidu, R., Mathison, G., Thani, H., & Lavoie, M. C. (2008). Relationship between african dust carried in the atlantic trade winds and surges in pediatric asthma attendances in the caribbean. *International Journal of Biometeorology*, *52*(8), 823–832.

Randles, C., Da Silva, A., Buchard, V., Colarco, P., Darmenov, A., Govindaraju, R., … others (2017). The merra-2 aerosol reanalysis, 1980 onward. part i: System description and data assimilation evaluation. *Journal of climate*, *30*(17), 6823–6850.

Rao, A., Pillai, R., Mani, M., & Ramamurthy, P. (2014). Influence of dust deposition on photovoltaic panel performance. *Energy Procedia*, *54*, 690 - 700. Retrieved from `http://www.sciencedirect.com/science/article/pii/S1876610214011874` (4th International Conference on Advances in Energy Research (ICAER 2013)) doi: https://doi.org/10.1016/j.egypro.2014.07.310

Rashki, A., Kaskaoutis, D., Mofidi, A., Minvielle, F., Chiapello, I., Legrand, M., … Francois, P. (2019). Effects of monsoon, shamal and levar winds on dust accumulation over the arabian sea during summer–the july 2016 case. *Aeolian Research*, *36*, 27–44.

Remer, L. A., Kaufman, Y., Tanré, D., Mattoo, S., Chu, D., Martins, J. V., … others (2005). The modis aerosol algorithm, products, and validation. *Journal of atmospheric sciences*, *62*(4), 947–973.

Rienecker, M. M., Suarez, M., Todling, R., Bacmeister, J., Takacs, L., Liu, H., … others (2008). *The geos-5 data assimilation system: Documentation of versions 5.0. 1, 5.1. 0, and 5.2. 0* (Tech. Rep.). NASA Goddard Space Flight Center, Greenbelt, Maryland.

Ryder, C. L., Highwood, E. J., Walser, A., Seibert, P., Philipp, A., & Weinzierl, B. (2019). Coarse and giant particles are ubiquitous in saharan dust export regions and are radiatively significant over the sahara. *Atmospheric Chemistry and Physics*, *19*(24), 15353–15376.

Sayyah, A., Horenstein, M. N., & Mazumder, M. K. (2014). Energy yield loss caused by dust deposition on photovoltaic panels. *Solar Energy*, *107*, 576–604.

Scheuvens, D., & Kandler, K. (2014). On composition, morphology, and size distribution of airborne mineral dust. *Mineral Dust*, 15–49.

Shao, Y. (2001). A model for mineral dust emission. *Journal of Geophysical Research: Atmospheres*, *106*(D17), 20239–20254.

Shao, Y., Fink, A. H., & Klose, M. (2010). Numerical simulation of a continental-scale saharan dust event. *Journal of Geophysical Research: Atmospheres*, *115*(D13).

Shevchenko, I., Engelbrecht, J. P., Mostamandi, S., & Stenchikov, G. (2021, July). Evaluation of minerals being deposited in the red sea using gravimetric, size distribution, and mineralogical analysis of dust deposition samples collected along the red sea coastal plain. *Aeolian Research*, *52*, 100717. Retrieved from `https://doi.org/10.1016/j.aeolia.2021.100717` doi: 10.1016/j.aeolia.2021.100717

Skamarock, W. C., Klemp, J. B., Dudhia, J., Gill, D. O., Barker, D. M., Wang, W., & Powers, J. G. (2005). *A description of the advanced research wrf version 2* (Tech. Rep.). National Center For Atmospheric Research Boulder Co Mesoscale and Microscale ....

Solomos, S., Kallos, G., Kushta, J., Astitha, M., Tremback, C., Nenes, A., & Levin, Z. (2011). An integrated modeling study on the effects of mineral dust and sea salt particles on clouds and precipitation. *Atmospheric Chemistry and Physics*, *11*(2), 873–892.

Stockwell, W. R., Kirchner, F., Kuhn, M., & Seefeld, S. (1997). A new mechanism for regional atmospheric chemistry modeling. *Journal of Geophysical Research: Atmospheres*, *102*(D22), 25847–25879.

Sulaiman, S. A., Singh, A. K., Mokhtar, M. M. M., & Bou-Rabee, M. A. (2014). Influence of dirt accumulation on performance of pv panels. *Energy Procedia*, *50*, 50 - 56. Retrieved from `http://www.sciencedirect.com/science/article/pii/S1876610214007425` (Technologies and Materials for Renewable Energy, Environment and Sustainability (TMREES14 – EUMISD)) doi: https://doi.org/10.1016/j.egypro.2014.06.006

Sunda, W. G., & Huntsman, S. A. (1997). Interrelated influence of iron, light and cell size on marine phytoplankton growth. *Nature*, *390*(6658), 389–392.

Swap, R., Ulanski, S., Cobbett, M., & Garstang, M. (1996). Temporal and spatial characteristics of saharan dust outbreaks. *Journal of Geophysical Research: Atmospheres*, *101*(D2), 4205–4220.

Talbot, R., Harriss, R., Browell, E., Gregory, G., Sebacher, D., & Beck, S. (1986). Distribution and geochemistry of aerosols in the tropical north atlantic troposphere: Relationship to saharan dust. *Journal of Geophysical Research: Atmospheres*, *91*(D4), 5173–5182.

Tegen, I., Harrison, S. P., Kohfeld, K., Prentice, I. C., Coe, M., & Heimann, M. (2002). Impact of vegetation and preferential source areas on global dust aerosol: Results from a model study. *Journal of Geophysical Research: Atmospheres*, *107*(D21), AAC–14.

Textor, C., Schulz, M., Guibert, S., Kinne, S., Balkanski, Y., Bauer, S., ... others (2006). Analysis and quantification of the diversities of aerosol life cycles within aerocom. *Atmospheric Chemistry and Physics*, *6*(7), 1777–1813.

Tindale, N., & Pease, P. (1999). Aerosols over the arabian sea: Atmospheric transport pathways and concentrations of dust and sea salt. *Deep Sea Research Part II: Topical Studies in Oceanography*, *46*(8-9), 1577–1595.

Todd, M. C., Bou Karam, D., Cavazos, C., Bouet, C., Heinold, B., Baldasano, J. M., ... others (2008). Quantifying uncertainty in estimates of mineral dust flux: An intercomparison of model performance over the bodélé depression, northern chad. *Journal of Geophysical Research: Atmospheres*, *113*(D24).

Ukhov, A., Ahmadov, R., Grell, G., & Stenchikov, G. (2021). Improving dust simulations in wrf-chem v4. 1.3 coupled with the gocart aerosol module. *Geoscientific Model Development*, *14*(1), 473–493.

Ukhov, A., Mostamandi, S., da Silva, A., Flemming, J., Alshehri, Y., Shevchenko, I., & Stenchikov, G. (2020). Assessment of natural and anthropogenic aerosol air pollution in the middle east using merra-2, cams data assimilation products, and high-resolution wrf-chem model simulations. *Atmospheric Chemistry and Physics*, *20*(15), 9281–9310.

Ukhov, A., & Stenchikov, G. (2020, March). *Merra2bc. interpolation utility for boundary and initial conditions used in wrf-chem.* Zenodo. Retrieved from `https://doi.org/10.5281/zenodo.3695911`

Uno, I., Wang, Z., Chiba, M., Chun, Y., Gong, S. L., Hara, Y., … others (2006). Dust model intercomparison (dmip) study over asia: Overview. *Journal of Geophysical Research: Atmospheres*, *111*(D12).

Valerino, M., Bergin, M., Ghoroi, C., Ratnaparkhi, A., & Smestad, G. P. (2020). Low-cost solar pv soiling sensor validation and size resolved soiling impacts: a comprehensive field study in western india. *Solar Energy*, *204*, 307–315.

Watson, A. J., Bakker, D., Ridgwell, A., Boyd, P., & Law, C. (2000). Effect of iron supply on southern ocean co2 uptake and implications for glacial atmospheric co2. *Nature*, *407*(6805), 730–733.

Yu, Y., Notaro, M., Kalashnikova, O. V., & Garay, M. J. (2016). Climatology of summer shamal wind in the middle east. *Journal of Geophysical Research: Atmospheres*, *121*(1), 289–305.

Zender, C. S., Bian, H., & Newman, D. (2003). Mineral dust entrainment and deposition (dead) model: Description and 1990s dust climatology. *Journal of Geophysical Research: Atmospheres*, *108*(D14).

Zender, C. S., Miller, R., & Tegen, I. (2004). Quantifying mineral dust mass budgets: Terminology, constraints, and current estimates. *Eos, Transactions American Geophysical Union*, *85*(48), 509–512.

Zhao, C., Chen, S., Leung, L. R., Qian, Y., Kok, J., Zaveri, R. A., & Huang, J. (2013). Uncertainty in modeling dust mass balance and radiative forcing from size parameterization. *Atmospheric Chemistry and Physics*, *13*(21), 10733–10753.

Zhao, C., Hu, Z., Qian, Y., Ruby Leung, L., Huang, J., Huang, M., … others (2014). Simulating black carbon and dust and their radiative forcing in seasonal snow: a case study over north china with field campaign measurements. *Atmospheric Chemistry and Physics*, *14*(20), 11475–11491.

Zhao, C., Liu, X., Leung, L., Johnson, B., McFarlane, S. A., Gustafson Jr, W., … Easter, R. (2010). The spatial distribution of mineral dust and its shortwave radiative forcing over north africa: modeling sensitivities to dust emissions and aerosol size treatments. *Atmospheric Chemistry and Physics*, *10*(18), 8821–8838.

Zhao, C., Liu, X., Ruby Leung, L., & Hagos, S. (2011). Radiative impact of mineral dust on monsoon precipitation variability over west africa. *Atmospheric Chemistry and Physics*, *11*(5), 1879–1893.

Zhu, X., Prospero, J., & Millero, F. J. (1997). Diel variability of soluble fe (ii) and soluble total fe in north african dust in the trade winds at barbados. *Journal of Geophysical Research: Atmospheres*, *102*(D17), 21297–21305.

Fine and Coarse Dust Effects on Radiative Forcing, Mass Deposition, and Solar Devices over the Middle East

Suleiman Mostamandi[1], Alexander Ukhov[1], Johann Engelbrecht[1,2], Illia Shevchenko[1], Sergey Osipov[1], Georgiy Stenchikov[1]

[1]King Abdullah University of Science and Technology, Thuwal, Saudi Arabia
[2]Desert Research Institute, Reno, Nevada, USA

Key Points:

- Models and reanalysis products underestimate coarse dust emission and dust deposition by 2-3 times
- Fine dust affects radiation, but coarse dust dominates mass deposition rates
- Atmospheric dust dims solar radiation, and coarse dust causes soiling of solar panels

Key Words: Emission, Air quality, Arabian Peninsula, PV, Soiling, WRF-Chem

Corresponding author: Georgiy Stenchikov, `georgiy.stenchikov@kaust.edu.sa`

Abstract

In desert regions like the Middle East (ME), dust has a profound impact on the environment, climate, air quality, and human health. In addition, dust affects the efficiency of solar energy devices by reducing the downward solar flux and settling on their optically active surfaces. The size of dust particles determines the extent of these effects. Our size-segregated dust deposition (DD) measurements show that coarse dust particles with geometric radius r > 10 μm comprise the majority of the deposited mass, but these particles are not represented in the current models that are tuned to fit the observed aerosol visible optical depth (AOD) but not dust emission (DE) or DD. As a result, the current models and reanalysis products severely underestimate DD and DE. This is the first study to constrain the dust simulations by both AOD and DD measurements to quantify the effect of coarse and fine dust on radiative fluxes and DD/DE rates using the WRF-Chem model. We found that, on average, coarse dust contributes less than 10% to dust shortwave (SW) radiative forcing (RF) at the surface but comprises more than 70% of DE. Coarse dust warms the atmosphere more effectively than fine dust in longwave (LW), comprising 30% of LW RF at the surface, although the LW effect is 2-3 times smaller than the SW effect. Aerosol annual mean net radiative cooling at the surface over the Arabian Peninsula and regional seas locally reaches 25 $W\ m^{-2}$. Airborne fine dust particles with radii r < 3 μm are mainly responsible for the significant dimming (5-10%) of solar radiation, cooling the surface and hampering solar energy production. However, dust mass deposition is primarily linked to coarse particles, causing accumulation of soiling losses at the rate of 2-5% per day. Therefore, incorporating coarse dust in model simulations and data assimilation would improve the overall description of the dust mass balance and its impact on environmental systems and solar devices.

1 Introduction

Mineral dust is a critical player in the earth system, with a broad impact on the environment and different aspects of weather, climate, planetary radiative budget, cloud microphysics, and atmospheric chemistry (Knippertz & Stuut, 2014; Anisimov et al., 2018; Z. Meng & Lu, 2007; Prospero et al., 2008; Ukhov et al., 2020; Parajuli et al., 2022). Dust fertilizes oceans by providing nutrients to surface waters and, ultimately, the seabed (Talbot et al., 1986; Watson et al., 2000; Swap et al., 1996; Zhu et al., 1997). The total annual dust deposition in the Red Sea reaches 8.6 Mt (Shevchenko et al., 2021), and major dust storms are estimated to contribute 6 Mt to this total (Jish Prakash et al., 2015). Dust can negatively impact infrastructure and technology by attenuating the solar radiation reaching the earth's surface due to dust scattering and absorption, therefore reducing the output of photovoltaic (PV) systems. Furthermore, dust deposition on solar panels diminishes their efficacy (Mani & Pillai, 2010a; Rao et al., 2014; Sulaiman et al., 2014; Valerino et al., 2020).

With its large deserts, the Middle East (ME) is one of the most significant mineral dust sources on Earth (Zender et al., 2004; Knippertz & Stuut, 2014; Ukhov et al., 2020). The region is characterized by hot, dry summers and mild winters with intermittent rains (Climate.com, 2018; Mostamandi et al., 2022). In summer, northern wind (Shamal) dominates (Yu et al., 2016; Hamidi et al., 2013; Anisimov et al., 2018); whereas in winter, southern wind, related to monsoon circulation, prevails. Column dust loading (DL) is controlled by dust emission (DE), dust transport (DT), and dust deposition (DD) (Knippertz & Stuut, 2014). DE is difficult to measure in situ and also to calculate in meteorological and climate models coupled with aerosol chemical transport models (Zender et al., 2004; Uno et al., 2006; Todd et al., 2008; Ginoux et al., 2012). The main mechanisms of dust generation in the ME are cold fronts, haboobs, and gust winds, but they are not all well represented in the up-to-date atmospheric chemical transport models. To resolve haboobs, for example, a grid spacing of at least 3-km is required to allow resolving deep convection (Anisimov et al., 2018; Kalenderski & Stenchikov, 2016). Unfortunately, calculations at this level of resolution require enormous computational resources and are not yet practical for long-term simulations. Insufficient model spatial resolution is compensated by adjusting the DE to fit the observed aerosol optical depth (AOD) (Anisimov et al., 2018; Z. Meng & Lu, 2007; Ukhov et al., 2020; Parajuli et al., 2022). However, DE is intrinsically related to DD because all emitted dust eventually settles to the surface. Thus, averaged annually and over the globe, DE = DD.

In addition to absorbing and scattering radiation, dust affects clouds, acting as cloud condensation nuclei (CCN) and ice nuclei (IN), and causes indirect radiation forcing (RF) (DeMott et al., 2010; Parajuli et al., 2022). Deposited dust alters surface albedo and harms vegetation (Chadwick et al., 1999). DL and dust optical depth (DOD) over the ME are higher than in other parts of the world (Jish Prakash et al., 2015; Kalenderski et al., 2013). Osipov et al. (2015) and Kalenderski and Stenchikov (2016) showed that mineral dust over the ME contributes more than 80% to AOD. Non-dust aerosols like sulfate (SO_4), sea salt (SS), black carbon (BC), organic carbon (OC), and volatile organic compounds (VOCs) comprise, on average, about 20% of AOD. We assume that the optical depth of non-dust aerosols is NOD=AOD-DOD. Osipov et al. (2022) indicated an even larger fractional contribution (about 30%) of anthropogenic fine particulates with geometric diameter less than 1 μm to AOD. In this study, we characterize particles by their geometric radii instead of using aerodynamic radii; for dust, aerodynamic radii are almost 50% smaller than geometric radii (Adebiyi et al., 2023).

Dust impacts regional radiative balance, thus affecting climate (Forster et al., 2007; Zhao et al., 2014; Ukhov et al., 2020). Kalenderski et al. (2013) simulated reduction of solar radiation at the earth's surface during a dust storm reaching 100 $W\ m^{-2}$. Osipov and Stenchikov (2018) calculated that the dust radiative effect has a profound thermal and dynamic impact on the Red Sea. Over the last two decades, the dust effects on the environment have been extensively studied (Marticorena & Bergametti, 1995; Ginoux et al., 2001; Shao, 2001; Zender et al., 2003; Darmenova et al., 2009; Shao et al., 2010; Zhao et al., 2010; Solomos et al., 2011; Mahowald et al., 2011; Cakmur et al., 2006; Kok et al., 2021; Adebiyi et al., 2023; Adebiyi & Kok, 2020). Although up-to-date models capture many features of dust generation and transport, the spatial distribution of dust and its RF remains uncertain (Zhao et al., 2013). For example, the simulated global DE in AeroCom models varies from 500 $Mt\ year^{-1}$ to 5000 $Mt\ year^{-1}$ (Textor et al., 2006; Huneeus et al., 2011; Kalenderski & Stenchikov, 2016).

The discrepancies in simulated dust emissions can be attributed to the fact that models are tuned to fit the observed visible AOD, and DE is a tuning parameter. Among different models, varying dust sources, particle size distribution (PSD), optical properties, and chemical composition are the major factors that exacerbate differences in the emissions (Ginoux et al., 2012; Tegen et al., 2002; Zender et al., 2003; Balkanski et al., 2007; Darmenova et al., 2009; McConnell et al., 2010; Kok, 2011; Zhao et al., 2010, 2011).

Dust size distribution and composition are key factors that control dust optical properties and the rate of gravitational sedimentation (Mallet et al., 2009; Bergametti & Forêt, 2014; Zhao et al., 2013; Mahowald et al., 2011; Kok et al., 2021; Adebiyi & Kok, 2020). However, the dust microphysical modules often do not consider giant (r > 10 μm) dust particles, which could be radiatively significant (Ryder et al., 2019; Kok et al., 2021; Adebiyi et al., 2023). The amount and size distribution of emitted dust depends on the surface wind, soil morphology, and moisture content. Kok (2011) analyzed six sets of size-resolved dust emission measurements and found that the size distribution of emitted fine dust with r < 5 μm is independent of wind speed (Kok, 2011; Kok et al., 2017). Adebiyi et al. (2023) suggested that the up-to-date models significantly underestimate coarse DL in the atmosphere because the models deposit coarse dust too rapidly.

Reducing the efficacy of solar energy devices is another aspect of dust impacts on human activities. Deserts receive a record amount of solar radiation, but a high concentration of dust in the atmosphere attenuates solar radiation at the Earth's surface. Dust deposited on PV panel surfaces causes soiling losses that accumulate at a rate of 0.1 to 1% per day (Ilse, Figgis, Naumann, et al., 2018; Valerino et al., 2020). Ilse, Figgis, Werner, et al. (2018) analyzed soiling and cementation processes on PV panels in Qatar, finding that dust deposition on PV surface causes energy losses exceeding 1% per day. Boyle et al. (2013, 2015) showed that 1 $g\ m^{-2}$ of dust deposited on a PV panel reduces power output by 4-6%. Ilse, Figgis, Naumann, et al. (2018) detected that the highest soiling rate is in the ME (0.95 % per day), and the lowest is in South America. Bergin et al. (2017) combined field measurements and global modeling to estimate the effect of aerosols on solar electricity generation, showing that about 17 to 25% of solar energy could be lost due to soiling in regions with abundant dust and anthropogenic aerosols. It was suggested that soiling losses associated with fine dust particles are larger than those caused by coarse particles (El-Shobokshy & Hussein, 1993; Sayyah et al., 2014; El-Shobokshy & Hussein, 1993; Ilse, Figgis, Werner, et al., 2018). Baras et al. (2016) conducted three years of soiling measurements in Rumah, Saudi Arabia, and proposed an 8-day cleaning cycle to increase the efficiency of PV panels. Mani and Pillai (2010b) found that weekly cleaning is necessary for the dry subtropics ($15-25°$N), which experience rare rainfall; in low latitudes with frequent rainfall, natural cleaning is usually sufficient. However, while heavy rains clean solar panels, light rains can increase surface contamination (Valerino et al., 2020; Ilse, Figgis, Naumann, et al., 2018). In regions with an arid and semi-arid climate, for example, dew can cause particle cementation on PV panel surfaces (Ilse, Figgis, Naumann, et al., 2018). Valerino et al. (2020) showed that high relative humidity almost doubles the soiling rate.

Thus both AOD and DD play an important role in shaping the dust impact on climate and solar devices. To achieve an agreement with observations, DE is usually tuned to fit the observed AOD in visible wavelengths in models. Because giant dust particles with r > 10 μm are often not considered in the models, the emission of dust particles with r < 10 μm is artificially increased to fit visible AOD, while the longwave (LW) effect of giant particles is underestimated (Zhao et al., 2014; Ukhov et al., 2020; Kalenderski et al., 2013; Adebiyi & Kok, 2020). At the same time, the simulated DD (and consequently DE) rates are much lower than observed (Engelbrecht et al., 2017; Shevchenko et al., 2021). DOD characterizes the amount of dust suspended in the atmosphere, and it alone is insufficient to constrain the dust mass balance because it is defined by DT, DD, and DE.

In this study, we combine model simulations, data assimilation products, and DD and AOD observations to quantify the dust impact in the ME. For the first time, we constrain the model dust simulations with both AOD and DD measurements. Considering the dust impact on solar devices, we account for both attenuation of incoming solar radiation by dust suspended in the atmosphere and soiling caused by DD, discriminating the effects of fine and coarse dust particles. Along with AOD observations, we utilize size-segregated DD measurements conducted at King Abdullah University of Science and Technology (KAUST, Saudi Arabia) (Jish Prakash et al., 2016; Engelbrecht et al., 2017; Shevchenko et al., 2021). We quantify the contributions of different dust sizes to RF and DD rate, aiming to answer the following questions:

1. What is the temporal and spatial distribution of dust mass deposition over the ME land areas and regional seas?
2. What are the comparative contributions of fine and coarse dust to radiative forcing and mass deposition rates over the ME?
3. What is the comparative impact of fine and coarse dust suspended in the atmosphere and deposited on surfaces on solar energy devices?

2 Methodology

First, we analyzed the model output obtained using the up-to-date model constrained only by AOD observations to reveal the deficiencies in the current models and reanalysis products. The size-segregated DD measurements, which we collected at the Red Sea coastal plain, allowed us to improve the model DE and calculate the effects of coarse and fine dust on DL, DD, RF, and the efficacy of solar devices. Below, in this section, we briefly discuss the data sets and the model used in this study.

2.1 Observations and Data Assimilation Products

The CIMEL robotic sun-photometer at the KAUST Campus has collected observations since the start of 2012. This instrument is part of the National Aeronautics and Space Administration (NASA) AErosol RObotic NETwork (AERONET, `http://aeronet.gsfc.nasa.gov`). The sun-photometer measures in clear-sky conditions direct sun and sky radiances at eight wavelengths (340, 380, 440, 500, 550, 670, 870, 940, and 1020 nm) every 15 min during daylight, providing spectral AODs and aerosol column integrated size distribution (Dubovik & King, 2000). AERONET data are available from `https://aeronet.gsfc.nasa.gov/cgi-bin/data_display_aod_v3?`. In addition to the KAUST site, this study uses AERONET observations from sites at Sede Boker and Mezaira (Fig. 1).

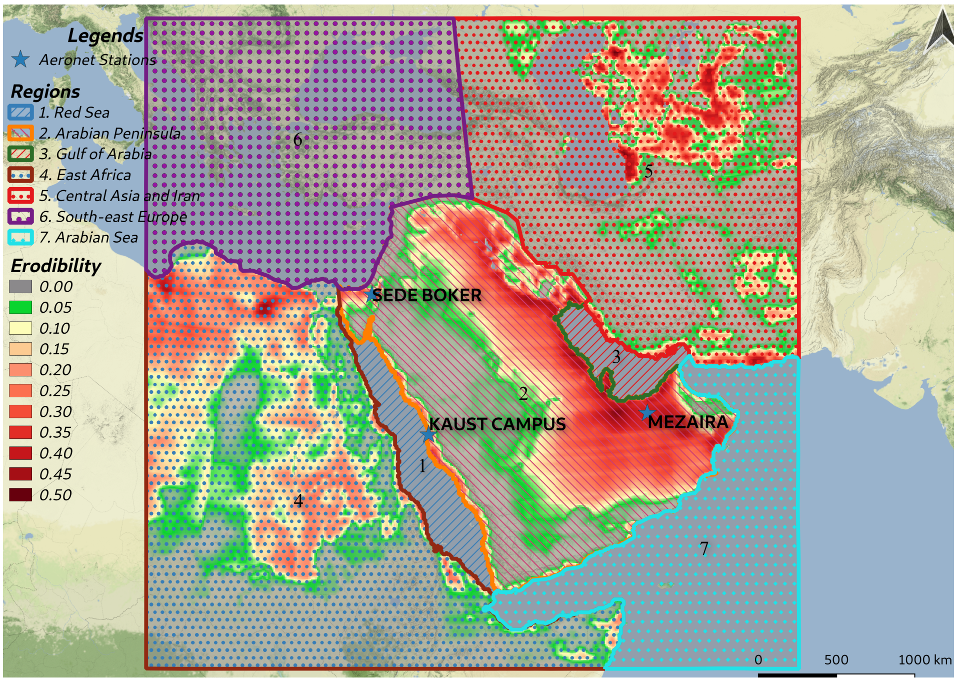

Figure 1: The square area depicts the simulation domain. Shading shows dust source function S. Contours show selected regions: 1 - The Red Sea, 0.46×10^6 km^2; 2 - Arabian Peninsula, 3.63×10^6 km^2; 3 - Arabian Gulf, 0.24×10^6 km^2; 4 - East Africa, 5.10×10^6 km^2; 5 - Central Asia and Iran, 4.51×10^6 km^2; 6 - South-East Europe, 3.37×10^6 km^2; and 7 - Arabian Sea, 2.09×10^6 km^2. Blue stars indicate the locations of AERONET stations used in the current study.

We used satellite observations to estimate the spatial-temporal distribution of modeled AOD. The Moderate Resolution Imaging Spectroradiometer (MODIS) instruments are aboard the NASA EOS (Earth Observing System) Terra and Aqua satellites. MODIS provides AOD over the global continents and oceans with a spatial resolution of $10 \times 10\ km^2$ (Remer et al., 2005; Abdou et al., 2005). We used AOD retrieval obtained using a "deep-blue" algorithm that is capable of providing aerosol optical thickness over bright land areas, such as most deserts (Levy et al., 2015).

To measure the amount of deposited dust, we used passive dust samplers, which collect settling dust in a sponge layer over a “frisbee plate” on a monthly basis. The dust was washed down from the frisbee and sponge with distilled water. After lyophilization, the samples were weighed and then subjected to XRD analysis to obtain their mineralogical composition. We measured particle size distribution in the samples using a Malvern Mastersizer 3000 Laser Diffraction Particle Size Analyzer (LPSA). The installation details, geographical coordinates of the deposition samplers, and observational data from December 2014-December 2019 can be found in (Shevchenko et al., 2021).

We also used reanalysis and data assimilation products as a data source. MERRA-2 reanalysis (`https://gmao.gsfc.nasa.gov/reanalysis/MERRA-2`) provides meteorological and atmospheric composition fields on a $0.625° \times 0.5°$ latitude-longitude grid and 72 terrain-following hybrid σ-p model levels (Randles et al., 2017; Buchard et al., 2017). MERRA-2 uses the Goddard Earth Observing System, version 5 (GEOS-5) atmospheric model (Rienecker et al., 2008), which is interactively coupled with the GOCART aerosol model (Chin et al., 2002, 2000). Anthropogenic emissions in MERRA-2 are based on the EDGAR-4.2 emission inventory (Janssens-Maenhout et al., 2013). MERRA-2 assimilates AERONET AODs and MODIS radiances (Randles et al., 2017). The European Center for Medium-Range Weather Forecast (ECMWF) Copernicus Atmosphere Monitoring Service (CAMS) provides operational daily analysis and forecast of AOD for aerosol species using an Integrated Forecast System (IFS) (Bozzo et al., 2017). The aerosol model implemented in CAMS is based on the modified version of the Laboratoire d’Optique Atmospherique (LMD) model (Boucher et al., 2002; Morcrette et al., 2009).

2.2 Model

In this study, we used a free-running regional meteorological and chemical transport model, WRF-Chem-3.7.1 (Skamarock et al., 2005; Grell et al., 2005), which has been configured for the ME. The model settings and the domain are similar to those we previously used in (Ukhov et al., 2020). The model domain (Fig. 1) covers the ME, Arabian Peninsula, Eastern Mediterranean, and parts of Central Asia with a $10 \times 10\ km^2$ horizontal grid and 50 hybrid vertical levels (See Figure 1). We employed the Yonsei University planetary boundary layer Scheme (YSU) (Hong et al., 2003). To account for atmospheric convection, we used the Grell 3D ensemble convective parameterization scheme (Grell & Dévényi, 2002).

To calculate atmospheric chemistry, we used the Regional Atmospheric Chemistry Mechanism (RACM) (Stockwell et al., 1997). The photolysis rates were calculated online according to (Madronich, 1987). Dust microphysics was calculated within the GOCART (Chin et al., 2000, 2002, 2014) model, which approximates the dust size distributions into five bins (Table 1).

The Rapid Radiative Transfer Model (RRTMG) for both SW and LW radiation is used for radiative transfer calculations (Iacono et al., 2008; E. Mlawer & Clough, 1998; E. J. Mlawer et al., 1997). In the course of this study, we found that WRF-Chem with GOCART microphysics erroneously disregards the radiative effect of dust particles with $r > 5\ \mu m$. However, GOCART considers particles with $0.1\ \mu m < r < 10\ \mu m$. We modified the code to rectify this error. It had a marginal effect in our previous simulations as bin 5 was poorly populated. However, it had a much stronger effect in the current study, as we significantly increased DE in bin 5 to account for the effect of giant dust particles (see below).

The dust emission scheme we employed in our simulations (Ginoux et al., 2001) assumes that dust emission mass flux, F_p ($\mu g\ m^{-2}\ s^{-1}$) in each dust-bin p=1,2,...,5 is defined by the relation:

$$F_p = \begin{cases} CSs_p u_{10m}^2(u_{10m} - u_t), & u_{10m} > u_t \\ 0, & u_{10m} < u_t \end{cases} \tag{1}$$

where C has the dimension of [$\mu g\ s^2\ m^{-5}$] and is a spatially uniform factor that controls the magnitude of dust emission flux; S is the dimensionless spatially varying dust source function (Ginoux et al., 2001) that characterizes the spatial distribution of dust emission sources ($0 < S < 1$); u_{10m} is the horizontal wind speed at 10 m above ground level; u_t is the threshold velocity, which depends on particle size and surface wetness; s_p is a fraction of dust mass emitted into dust-bin p, and $\sum s_p = 1$. s_p (p=1,2,3,4,5) defines the size distribution of emitted dust.

2.3 Model Tuning Using AERONET AOD and PSD

In (Ukhov et al., 2020), following the common practice (Kalenderski & Stenchikov, 2016; Jish Prakash et al., 2015; Zhao et al., 2010), we tuned dust emissions to fit the AOD from the AERONET stations located within the domain. For this purpose, the factor C from Eq. (1) was adjusted to obtain the best agreement between simulated and observed AOD at the KAUST Campus, the Mezaira, and Sede Boker AERONET sites (C = 0.525). We also tuned s_p from (1) to better reproduce the Aerosol Volume Size Distribution (PSD) provided by the AERONET inversion algorithm (Ukhov et al., 2020, 2021) (see Table 1).

Table 1: Dust Bins and Dust Emission Size Distribution Parameters

Dust Bins

Bin Numbers	1	2	3	4	5
Radii (μm)	0.1 - 1.0	1.0 - 1.8	1.8 - 3.0	3.0 - 6.0	6.0 - 10.0
Sp (Ukhov et al., 2020)	0.15	0.1	0.25	0.4	0.1
Sp (This Study)	0.05	0.03	0.07	0.12	0.73

The aerosol number-density or volume PSD defines the aerosol lifetime with respect to gravitational sedimentation and largely controls their radiative effect (Shevchenko et al., 2021; Osipov et al., 2015; Miller & Tegen, 1998; Highwood & Ryder, 2014; Scheuvens & Kandler, 2014; Maghami et al., 2016).

Figure 2 compares the annual average column integrated PSD from WRF-Chem simulations in (Ukhov et al., 2020) with PSD from the AERONET retrievals (Dubovik & King, 2000) for the KAUST Campus, Mezaira, and Sede Boker AERONET sites. The solid green line depicts AERONET PSD, the blue bars show PSD from (Ukhov et al., 2020), and the red bars show PSD obtained in this study (discussed below; Table 1). For all locations, the model in (Ukhov et al., 2020) reproduces the observed AERONET PSDs. The PSDs have a fine mode and coarse mode, peaking at r=0.2 μm and r=2.5 μm respectively. The AERONET retrievals and the model do not include particles with r > 10 μm. They are not approximated in the model (see Table 1) and AERONET is weakly sensitive to particles with r > 10 μm, which are much larger than the AERONET sun-photometer maximum operating wavelength of 1.02 μm. Further below we refer to the

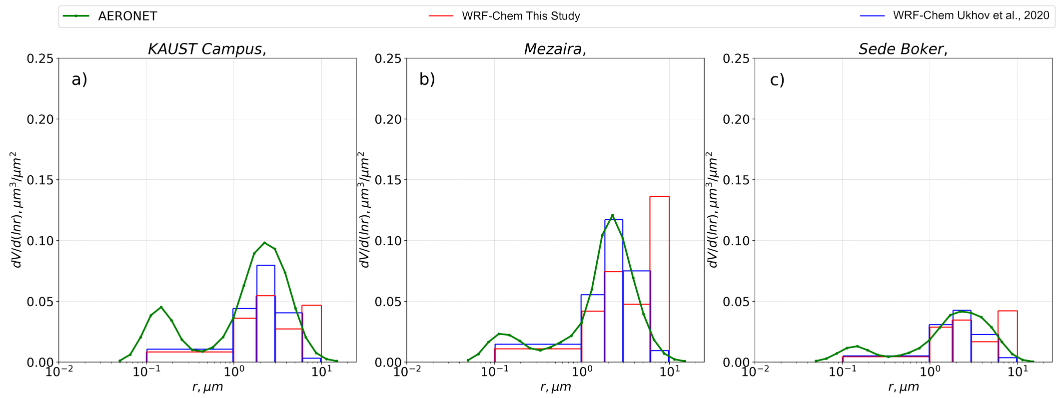

Figure 2: Annual average volume PSDs $\mu m^3 \mu m^{-2}$ calculated within WRF-Chem (bars), and obtained by AERONET inversion algorithm (green solid line) for 2016 at a) KAUST Campus, b) Mezaira and c) Sede Boker. The blue bars are from the WRF-Chem run without the DD constraints, and the red bars are from the current study with the DD constraints.

particles in the first three bins with r < 3 μm as fine dust; the particles in bins 4 and 5 with 3 μm < r < 10 μm as coarse dust; and the particles with r > 10 μm, that are not approximated in most models (but are present in the dust deposition samples), as giant dust particles.

2.4 Test of AOD Fitted Model against DD Observations

Before discussing the new model setup, the deficiencies of the previous free-running model simulations and data assimilation products constrained by only AERONET observations and tested against satellite AODs should be analyzed. To achieve this, we first compared the DD calculated in MERRA-2, CAMS, and the free-running WRF-Chem tuned using AERONET AOD as in (Ukhov et al., 2020) with the DD observations at the KAUST site. The data assimilation products, like MERRA-2 and CAMS, are often used as a proxy for observations, but none of the available assimilation systems are constrained by DD or DE measurements. Therefore, for these products, DD is based on their physical parameterizations, as in free-running WRF-Chem, and must be similarly tested against observations.

For this test, we used the DD measurements that have been conducted at the KAUST site since 2015 (Figure 3). To make a meaningful comparison of the observed and simulated DD, we measured PSD in all deposited samples (Engelbrecht et al., 2017; Shevchenko et al., 2021). The simulated (in WRF-Chem, MERRA-2, and CAMS) and observed monthly DD rates at the KAUST site throughout 2016 are shown in Figure 3, revealing a striking difference between the observed and simulated DD. The observed DD rates are more than three times higher than the simulated rates. This issue was discussed in (Engelbrecht et al., 2017; Shevchenko et al., 2021); the discrepancy occurs because we collect particles with radii up to 30 μm for observations, but in the models, we consider only particles with r < 10 μm. At the same time, the DD of particles with r < 5 μm in the models and reanalysis products compare well with observations. Figure 4a shows the 2016 annual average normalized (to 100%) volume PSD of deposited dust at the KAUST site (Shevchenko et al., 2021). Table 2 compares the DD rates at the KAUST campus calculated within WRF-Chem with the settings from (Ukhov et al., 2020), MERRA-2, and CAMS with 2016 observations (Shevchenko et al., 2021). The correlation coefficient (R), root mean square error (RMSE), and bias were calculated with respect to observations

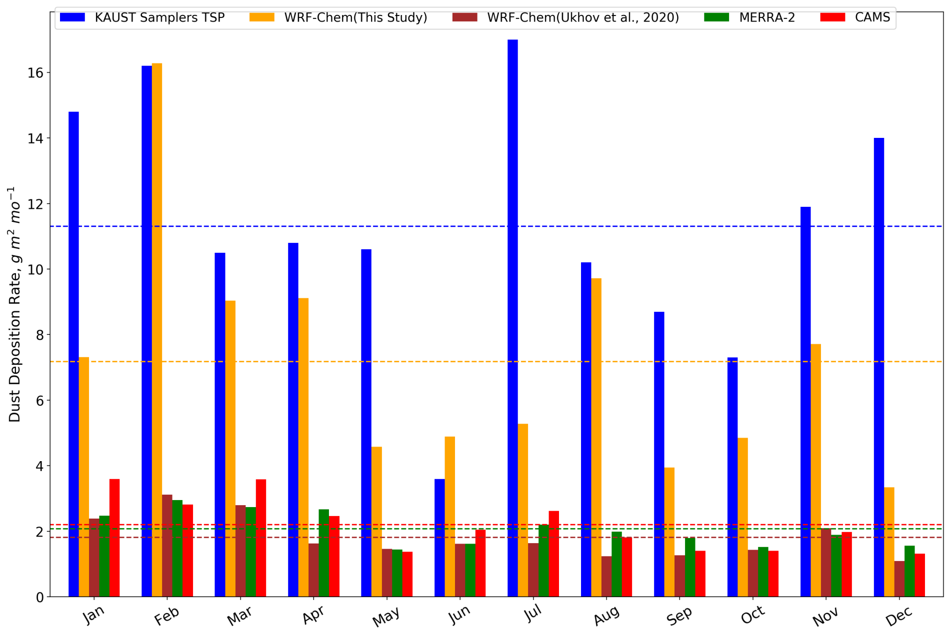

Figure 3: Monthly dust deposition rates ($g\ m^{-2} mo^{-1}$) averaged for six KAUST deposition sites (blue), simulated in WRF-Chem without the DD constraints (brown) and in the current study with DD constraints (light brown), calculated in MERRA-2 (green), and CAMS (red) at KAUST campus for 2016. Dashed lines show annual mean deposition rates for corresponding observations.

using monthly data. For WRF-Chem, R=0.70, while for MERRA-2 and CAMS R=0.25 and 0.36, respectively. The WRF-Chem DD annual bias = -9.48 $g\ m^{-2}\ mo^{-1}$. At the same time, WRF-Chem, MERRA-2, and CAMS reproduce the DD rate of particles with r $< 5\ \mu m$ much better (see Table S1 in the supplement information). Thus, AERONET tuning helps to simulate the dust fraction with r $< 5\ \mu m$ relatively well, but coarse (5 $<$ r $<$ 10) and giant (r $>$ 10) dust is simulated poorly.

Figure 4b presents the annual mean normalized (to 100%) volume PSD (shown in bins) of emitted and deposited dust calculated in the model (Ukhov et al., 2020), as well as dust suspended in the atmosphere at the KAUST site. Dust suspended in the atmosphere comprises a larger fraction of fine particles in bins 1, 2, and 3 than in dust emissions because these particles have a longer lifetime in the atmosphere than coarse particles in bins 4 and 5. Compared to emissions, the deposited dust has a larger fraction of the coarsest bins 4 and 5 because coarse particles deposit quickly. The fraction of coarse particles suspended in the atmosphere is 2-3 times smaller than in deposited dust. Thus, atmospheric dust loadings are less sensitive to coarse dust emission than DD. Comparing the size distributions of deposited dust in Figures 4a and b, we conclude that the WRF-Chem model with the settings from (Ukhov et al., 2020), in addition to the missing particles with r $> 10\ \mu m$, underestimates the emission of coarse particles with 6 $\mu m <$ r $<$ 10 μm in bin 5, as the observed size distribution reaches a maximum for r $> 10\ \mu m$ but in simulation bin 4 (3-6 μm) is the most abundant. This indicates that even within the approximated dust sizes r $< 10\ \mu m$, the model underestimates the emission of coarse dust. In the new model setup developed in this study, we aim to fix this discrepancy and account for the effect of giant dust particles with r $> 10\ \mu m$ by fitting AOD and DD simultaneously.

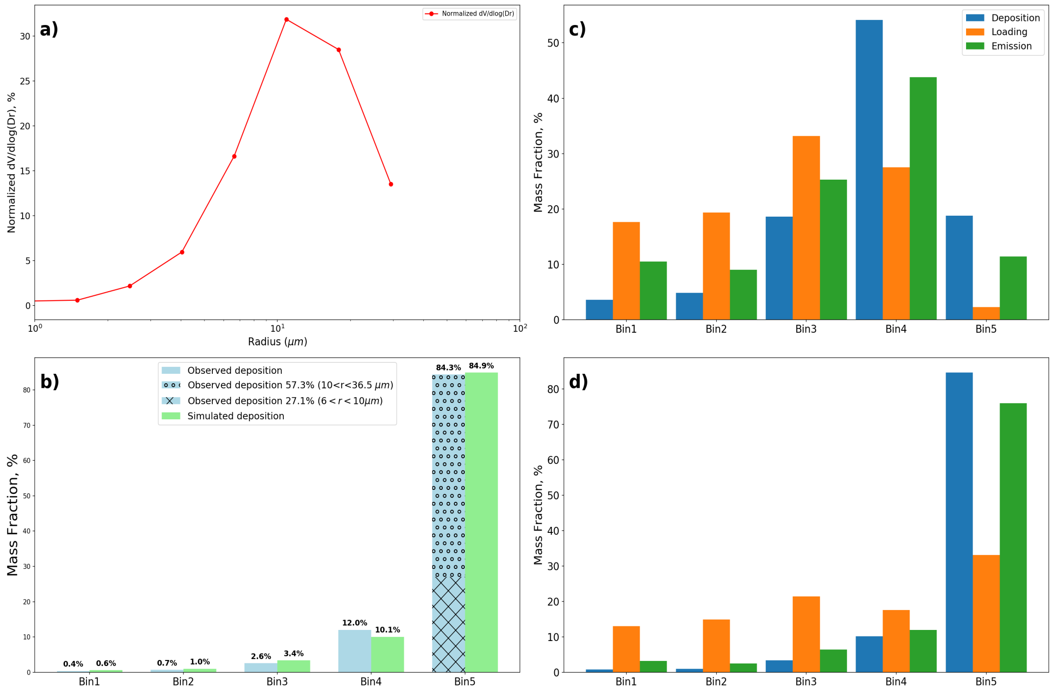

Figure 4: Annual mean normalized (to 100%) volume PSD for 2016: a) Measured in deposited samples at KAUST Campus; b) Simulated in bins in the run without DD constraints: DD (blue), DE (green), and DL (orange); c) DD simulated in bins in the run with DD constraints (blue) and integrated in bins using observed PSD in panel a; d) same as b), but in the run with the DD constraints.

Table 2: Statistical scores (R, RMSE, and Bias) of DD simulated within WRF-Chem, MERRA2, and CAMS compared to observations for 2016.

	R	RMSE	Bias
WRF-Chem (Ukhov et al., 2020)	0.70	10.10	-9.48
WRF-Chem (This Study)	0.79	5.75	-4.12
MERRA-2	0.25	9.85	-9.22
CAMS	0.36	9.19	-8.54

3 RESULTS

In this section, we first describe the new model setup constrained by AERONET AOD at three AERONET stations and DD observations at the KAUST site. We test the model results against observations and further discuss the geographical distributions of simulated SW and LW dust RF at the Earth's surface and DD over the Arabian Peninsula and the regional seas. We also develop a theoretical model to calculate the effect of DD and dust suspended in the atmosphere on the efficacy of PV panels.

3.1 Test of Model Setup with Simultaneous Fitting of AOD and DD

To simultaneously fit both AOD and DD in WRF-Chem simulations, we modified the DE size distribution, assuming that bin 5 incorporates a mass of dust particles with r > 6 μm including giant particles with r > 10 μm. The relative distribution of emitted mass in bins 1-4, which were constrained by AERONET PSD, remained intact. The new s_p settings are shown in Table 1. To fit the observed DD, we increased the emission in the largest bin 5 to 73% of the total mass. To fit the observed AOD, we chose C=1. It is suggested that the deposition rate for giant dust particles is overestimated in the models due to unaccounted asphericity of dust particles or turbulence effects (Adebiyi & Kok, 2020; Adebiyi et al., 2023). To overcome this deficiency, J. Meng et al. (2022), Adebiyi et al. (2023) decreased the density of giant particles. In our study, approximating the giant particles in bin 5 (6 μm < r < 10 μm) would effectively lower the sedimentation velocity for giant dust particles. The radiative effect of giant particles will be slightly overestimated both in SW and LW in our case, as particles in bin 5 are more optically effective per unit mass than giant dust particles both in SW and LW (this effect is quantified in section 3.2.3).

We ran the WRF-Chem-3.7.1 model for the entire year 2016. The lateral boundary and initial conditions for meteorological fields, aerosols, and chemical species were calculated using MERRA-2 reanalysis (Ukhov & Stenchikov, 2020). This provides the most consistent boundary conditions that allow us to use a moderate-size spatial domain and reduce computation time. Simulations were conducted for all months in parallel, with one week spin-up time for each month. The integration time step was 60 s.

In the chosen domain, there are three main dust emission areas (Figure 1). In Central Asia, dust is emitted predominantly between the Aral and Caspian Seas. In the Arabian Peninsula, the main dust sources are in the eastern region and a narrow zone along the west coast. In Africa, dust is generated in the Sahara and Somalian Peninsula. To represent climatology and spatial distribution of dust deposition, we divided our simulation domain into seven regions (Figure 1) based on the spatial patterns of the source function S.

To demonstrate how the model reproduces the DD and AOD, we test simulated both with observations. The bias of DD in the current simulations decreased at least two times compared with runs without DD tuning, and the correlation coefficient reached 0.79 (see Table 2). Figure 3 shows a subsequent better fit of DD and observations. Figure 5 demonstrates that the simulated AOD fits the AERONET observations at the KAUST, Mezaira, and Sede Boker sites well (see Figure 1). Table 3 compares the WRF-Chem, CAMS, and MERRA-2 daily averaged AODs with the AERONET observations at the KAUST Campus, Mezaira, and Sede Boker. Because of the finer spatial resolution, the free-running WRF-Chem outperforms the assimilation products. Table 4 summarizes the statistical scores for the simulated annual and seasonal mean AODs with respect to MODIS. WRF-Chem has the smallest RMSE and bias with respect to the MODIS AOD compared with MERRA-2 and CAMS data assimilation products. The spatial correlation of WRF-Chem AOD is close to that produced by both data-assimilation products.

Table 3: Statistical Scores (R and Bias) of daily mean AODs from CAMS, MERRA-2, and WRF-Chem with DD constraints with respect to AERONET AOD observations for 2016

	CAMS		MERRA-2		WRF-Chem	
	R	*bias*	*R*	*bias*	*R*	*bias*
KAUST Campus	0.71	0.01	0.85	-0.05	0.74	-0.04
Mezaira	0.62	0.12	0.83	0.04	0.73	0.07
Sede Boker	0.83	0.07	0.72	0.02	0.43	-0.01

Table 4: Statistical Scores (R, RMSE, and Bias) of annual and seasonal mean AODs for 2016 from CAMS, MERRA-2, and WRF-Chem with DD constraints with respect to MODIS observations

	CAMS			MERRA-2			WRF-Chem		
	R	*RMSE*	*bias*	*R*	*RMSE*	*bias*	*R*	*RMSE*	*bias*
Winter (DJF)	0.59	0.08	0.02	0.57	0.09	-0.03	0.47	0.08	-0.01
Spring (MAM)	0.70	0.13	0.05	0.72	0.13	-0.05	0.62	0.12	-0.01
Summer (JJA)	0.70	0.15	0.07	0.74	0.13	-0.05	0.68	0.17	0.000
Autumn (SON)	0.56	0.11	0.03	0.60	0.11	-0.03	0.43	0.11	-0.02
Annual mean	0.65	0.12	0.04	0.66	0.12	-0.04	0.61	0.12	-0.01

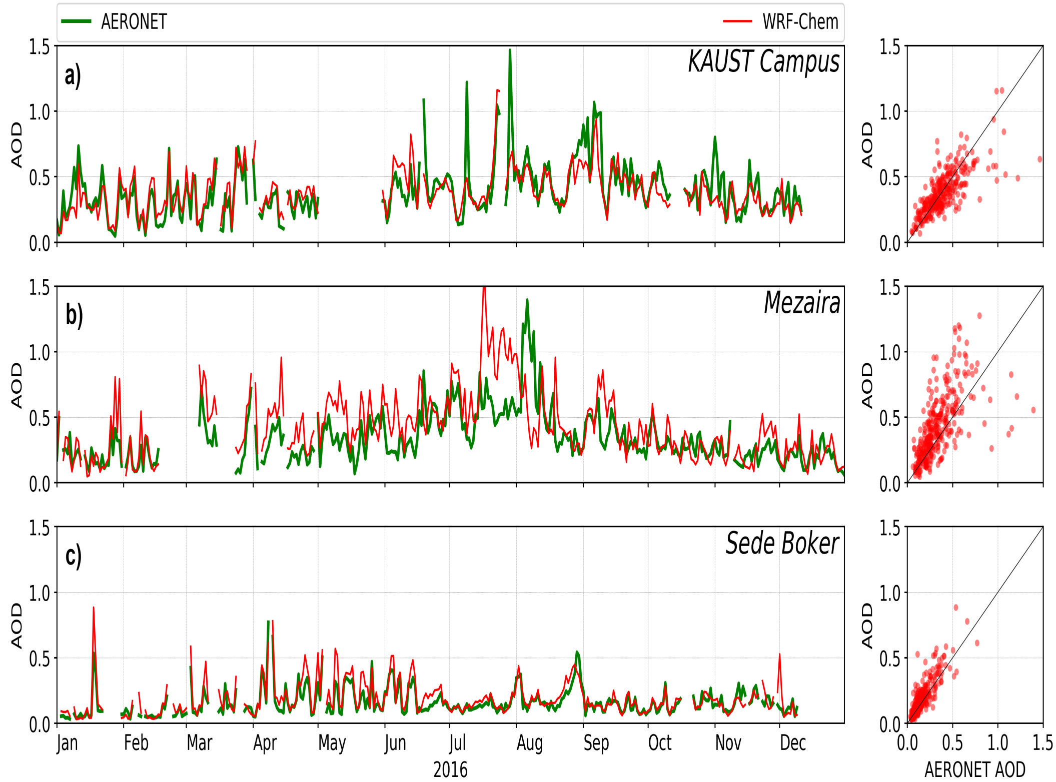

Figure 5: Observed AERONET and simulated WRF-Chem daily mean aerosol optical depth in 2016 for: a) KAUST Campus, b) Mezaira, and c) Sede Boker. The green curve shows AERONET AOD at 0.550 μm and the red curve shows model AOD at 0.6 μm. Scatter diagrams are shown on the right.

Figure 4c demonstrates that the simulated annual average volume PSD of DD (at the KAUST Campus), approximated by five bins, closely reflects that calculated using the observed PSD in Figure 4a. The coarse dust particles with 6 μm < r < 10 μm and giant dust particles with r > 10 μm contribute 27% and 57 % to observed DD, respectively. Figure 4d shows annual mean normalized (to 100%) volume PSDs of emitted dust, suspended in the atmosphere dust, and deposited dust simulated in this study. With the new settings, bin 5 contributes 73% to DE, 80% to DD, and 30% to dust atmospheric loading. The red bars in Figure 2 show the PSD of dust suspended in the atmosphere simulated in the current study when the model was simultaneously constrained by DD and AERONET AOD. With new settings, bin 5 (which also accounts for giant dust) is more pronounced, reflecting the large-radii tail of PSD that is not captured by AERONET retrieval (Figure 2). Overall, we conclude that the performance of the WRF-Chem tuned simultaneously by AOD and DD improved in comparison with our previous simulations, and it adequately represents the AOD and DD observations. Below, we use our model output to analyze the geographically distributed effects of dust in the ME in terms of its radiative impact on climate, DD rates, and deterioration of the efficacy of solar devices.

3.2 Radiative Effects of Coarse and Fine Dust

The radiative effects of dust particles suspended in the atmosphere are calculated using Mie theory because particles are sparse and distances between them are much larger than their sizes. Therefore, they do not interact optically, and their collective optical effect is a linear superposition of the effect of all individual particles. The optical properties of the individual particles are defined by their size, shape, and complex refractive index. The particles are most optically effective for the wavelengths comparable to their size. The complex part of the refractive index characterizes light absorption. Dust particles could effectively scatter and absorb solar radiation, which complicates the calculation and interpretation of their radiative effect.

3.2.1 AODs

Aerosol RF remains one of the largest uncertainties in future climate projections (Gliß et al., 2020). Dust RF depends on dust abundance, composition, and size distribution and is modulated by surface albedo (Osipov et al., 2015). In dust source regions like the ME, dust is particularly essential because of its widespread abundance. Evaluating the radiative effect of dust, we stepped ahead of the conventional approach in the analysis of AODs and RF by discriminating the effects of dust particles of different sizes. Coarse and fine dust particles have a different lifetime in the atmosphere, which controls how far from an emission source they can be transported by atmospheric airflow. In SW, finer dust particles are generally more optically active per unit mass compared to coarser particles.

In WRF-Chem, we calculated the contributions of each of the five aerosol bins (see Table 1) to optical depth and instantaneous RF. We specifically focused on the surface RF, as we were interested in the impact of dust on ground-based solar devices. We also compared the radiative effects of dust and non-dust aerosols. Figure 6 shows the visible (0.6 μm) optical depth produced by each dust bin and the total DOD. The finest dust bin 1 (0.1-1 μm), which comprises a relatively small mass, produces 45% of DOD, and bins 2 and 3 (1-3 μm) combined contribute about 42%. The optical depth of coarse dust in bin 5, which comprises the most dust mass (Figure 2), is 6% of total visible DOD.

Figure 7a shows the visible optical depth of non-dust aerosols that comprise the effects of sea salt over marine areas, biomass burning BC and OC mostly transported from Africa, and anthropogenic sulfate over the eastern Red Sea, Arabian Gulf, and Yemeni coastal areas and Oman. The high air pollution over the Arabian Sea originates from India and comprises a mixture of BC, OC, and sulfates/nitrates. The non-dust AOD is comparable with the DOD in coastal areas, but is much smaller than the DOD in the interior of the Arabian Peninsula.

Our results show a stronger dust contribution to AOD over the Arabian Sea and the Red Sea compared with previous studies (Myhre et al., 2013; Osipov et al., 2022). However, the aerosol effects are spatially variable and their contributions depend on the

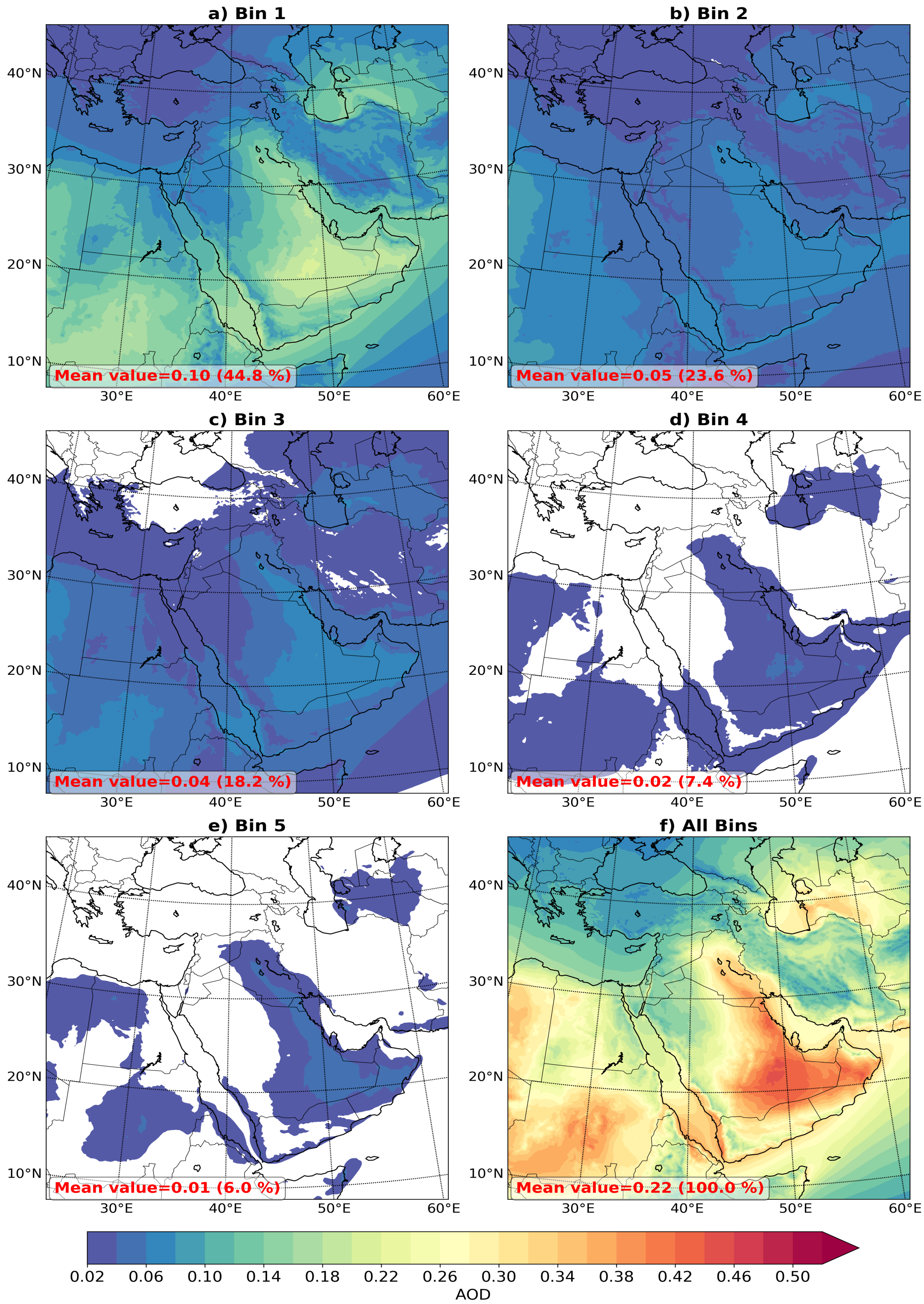

Figure 6: Annual mean visible DOD (0.6 μm) caused by individual bins and the total simulated in WRF-Chem with the DD constraints for 2016: a) Bin 1, b) Bin 2, c) Bin 3, d) Bin 4, e) Bin 5, and f) all Bins. The area average DODs and their relative contributions to each bin are shown at the bottom of each panel.

distribution of aerosol sources. For example, we observed that dust produces more than

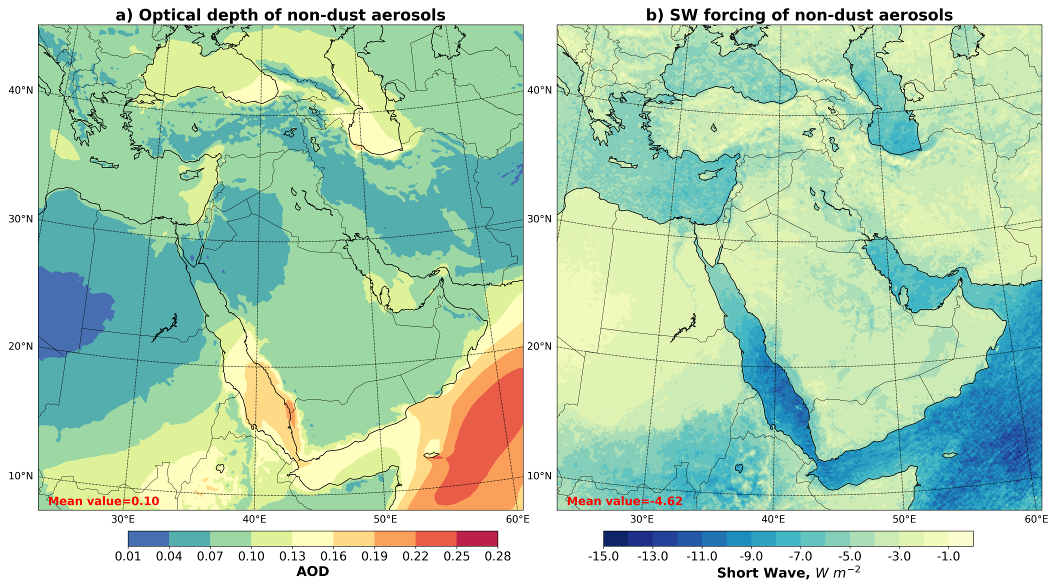

Figure 7: a) Annual mean non-dust visible optical depth, NOD at 0.6 μm calculated in WRF-Chem with the DD constraints for 2016; b) SW clear-sky radiative forcing ($W\ m^{-2}$) of non-dust aerosols at the surface calculated in WRF-Chem with the DD constraints for 2016. The area average NOD and RF are shown at the bottom of each panel.

80% of visible AOD in the interior regions of the Arabian Peninsula, where anthropogenic aerosol sources are weak compared to natural sources.

3.2.2 Aerosol Radiative Forcing

Fig. 8 presents the annual mean clear-sky direct instantaneous dust SW RF at the surface produced by each dust bin and the total. The radiative fluxes were obtained by double calls of radiative routine with and without the corresponding dust component. The radiative transfer calculations were conducted on the same meteorological fields (temperature and humidity). The RF was obtained as the difference between the net SW downward flux ($SW_{\downarrow} - SW_{\uparrow}$) in the calls with and without the corresponding dust bin. The dust total SW RF at the surface is negative, as dust absorbs and scatters SW radiation, thereby reducing solar radiation flux reaching the surface. The finest three bins with r $< 3\ \mu m$ contribute almost all of the RF. The contribution of the coarsest dust particles with r $> 6\ Wm^{-2}$ (represented by bin 5) in the total SW surface RF is about 7-8%, so the coarse dust SW radiative effect is relatively small, although it is not negligible. The total annual mean SW RF reaches -30 Wm^{-2} over the southern Red Sea. This area experiences one of the largest climatological forcings in the world (Osipov & Stenchikov, 2018). We also observe that the continental dust outflow generates high RF over the southern coast of the Arabian Peninsula and the Arabian Sea, reaching -20 Wm^{-2}. Over land, the RF peaks in the dust source areas, including Rub' al-Khali, the deserts in the eastern Arabian Peninsula, and the Red Sea coastal plain.

Fig. 9 shows clear-sky direct instantaneous dust LW RF at the surface for each bin and all bins. The LW RF, similar to the SW RF, is calculated using double calls of radiation routines. It is calculated as the difference between ($LW_{\downarrow} - LW_{\uparrow}$) flux with and without the corresponding dust component. Dust thermal radiation warms the surface, but the average magnitude over the domain LW warming is four times smaller compared to SW cooling. The largest LW effect is over land areas, caused predominantly by coarse dust, and the coarsest bin 5 contributes 26% of the LW radiative heating at the surface. However, the average over the domain LW surface heating is only 3.26 Wm^{-2}.

The instantaneous net (SW + LW) RF is shown in Fig. 10. This RF defines the effect of dust on the regional climate and reflects the spatial pattern of the SW RF. Fine bins are the major contributors. Averaged over the domain, the annual mean radiative cooling reaches 5.72 Wm^{-2}, but over the southern Red Sea it exceeds 20 Wm^{-2}. Dust bin 5 is the only bin that actually warms the surface. The SW and LW radiative effects of the coarsest bin almost cancel each other resulting in a 3.5% contribution to the net RF at the surface.

The non-dust aerosols mostly contribute to the SW RF (see Figure 7b), as their LW RF in the ME is negligible. Averaged over the domain, the SW RF of non-dust aerosols is twice as small (but still significant) compared to dust SW RF. The contribution of non-dust aerosols becomes more significant in the cities, the areas affected by industrial sulfur emissions, and over regional seas where the dust effect diminishes.

3.2.3 Test of the Radiative Effects of Coarse and Giant Dust Using Observed PSD

Following the approach used in (Adebiyi et al., 2023; Adebiyi & Kok, 2020), we used the PSD observed in the central part of the Arabian Peninsula (Pósfai et al., 2013) to calculate the contribution of coarse and giant dust particles in aerosol optical properties and RF and to test our model results discussed in the previous section. For this, we used a 1D standalone column model that employs Line-by-Line radiative transfer calculations (Mok et al., 2016; Osipov et al., 2020). A standalone modeling framework permits greater flexibility and higher accuracy of radiative transfer calculations than broadband radiative codes embedded in unwieldy and complex Global Circulation Models (GCMs). We employ a realistic PSD (Figure 11), which spans 0.05 μm < r < 30 μm. The size distribution was sampled in Riyadh on 9 April, 2007 during the Kingdom of Saudi Arabia Assessment of Rainfall Augmentation research program (Pósfai et al., 2013; Anisimov et al., 2018) after a typical mesoscale haboob dust storm event in the region (referred to hereafter as Riyadh PSD). It comprises a longer large-particle tail compared to other size distributions sampled in fair weather conditions (see Figure 16 in (Anisimov et al., 2018) and corresponding explanations). The instrument counts aerosol particles at the immediate entrance of the inlet, so the loss of large particles should be low (Pósfai et al., 2013). During the campaign, the research aircraft followed a spiral trajectory, sampling the entire dust profile in the troposphere. We took advantage of the vertical sampling to derive and employ the column-integrated PSD.

Compared with the recent airborne campaigns in the Sahara (see Figure 4 in (Adebiyi et al., 2023)), the Riyadh PSD falls within the envelope of dust size distributions obtained in SAMUM1 and SAMUM2 campaigns and is similar to AER-D size distribution with the maximum at 7 μm. The Riyadh PSD, similar to the bulk of Saharan size distributions, has a less pronounced relative contribution of the super-coarse particles (10 μm $< r < 30\mu m$) than the Fennec PSD (Ryder et al., 2019). The dust particles with r > $30\mu m$ were not measured during the Riyadh campaign.

The RF of dust, including its sensitivity to various parameters, has been studied extensively using 1D models (e.g., Figure 16 in (Osipov et al., 2015)). Instead, here we quantify the relative contribution of dust particles of various sizes to the optical depth τ and RF (defined as a difference ΔF of surface radiative fluxes calculated with and without dust effect) via diagnostics similar to the cumulative distribution function (CDF):

$$\tau_{CDF}(r^*) = \frac{\tau(r^*)}{\tau} \tag{2}$$

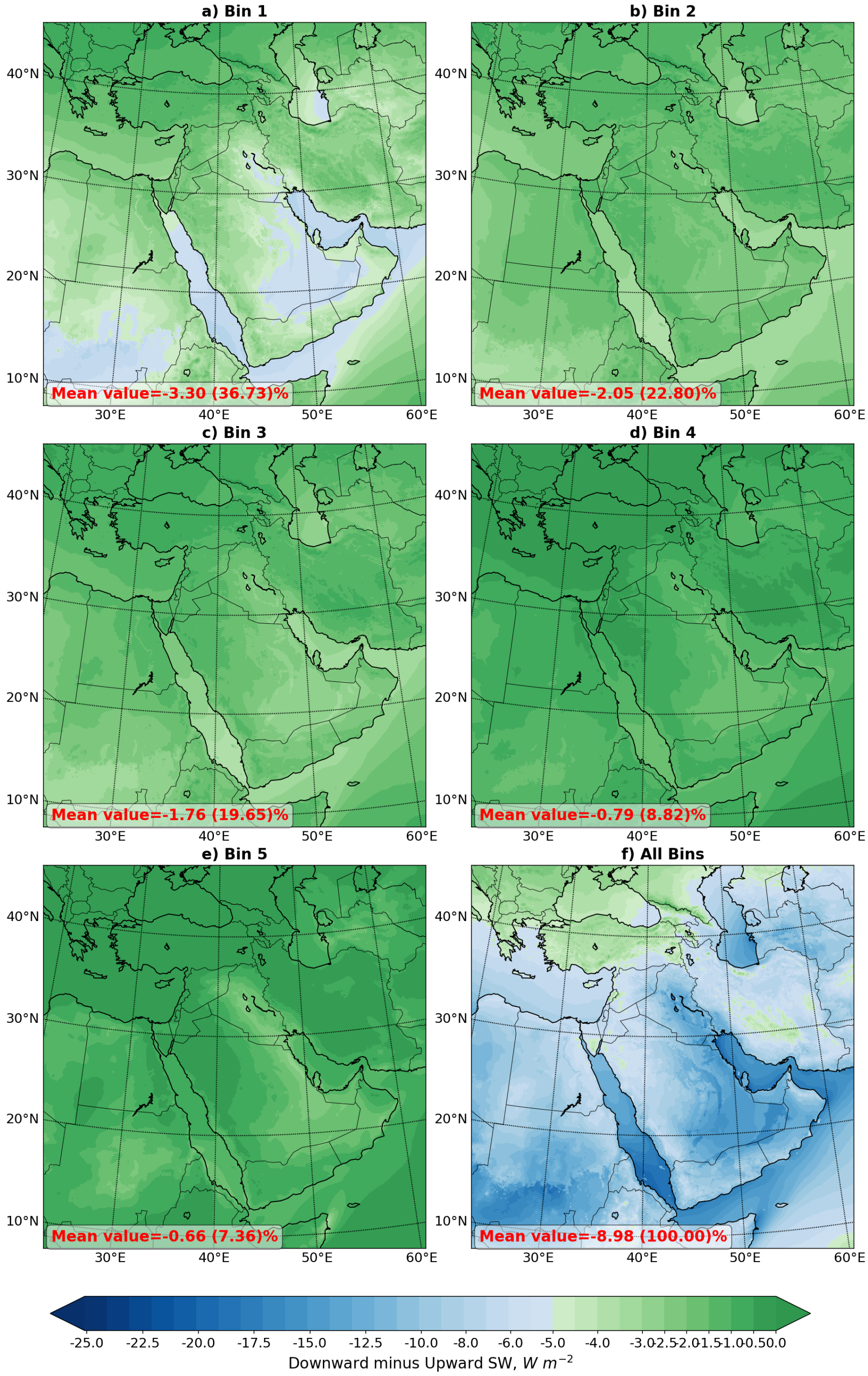

Figure 8: Annual mean clear-sky SW dust radiative forcing ($W\ m^{-2}$) at the surface caused by the individual bins and total calculated in WRF-Chem with the DD constraints for 2016: a) Bin 1, b) Bin 2, c) Bin 3, d) Bin 4, e) Bin 5, and f) all Bins. The area average forcing and relative contributions of each bin are shown at the bottom of each panel.

$$\Delta F_{CDF}(r^*) = \frac{\Delta F(r^*)}{\Delta F} \tag{3}$$

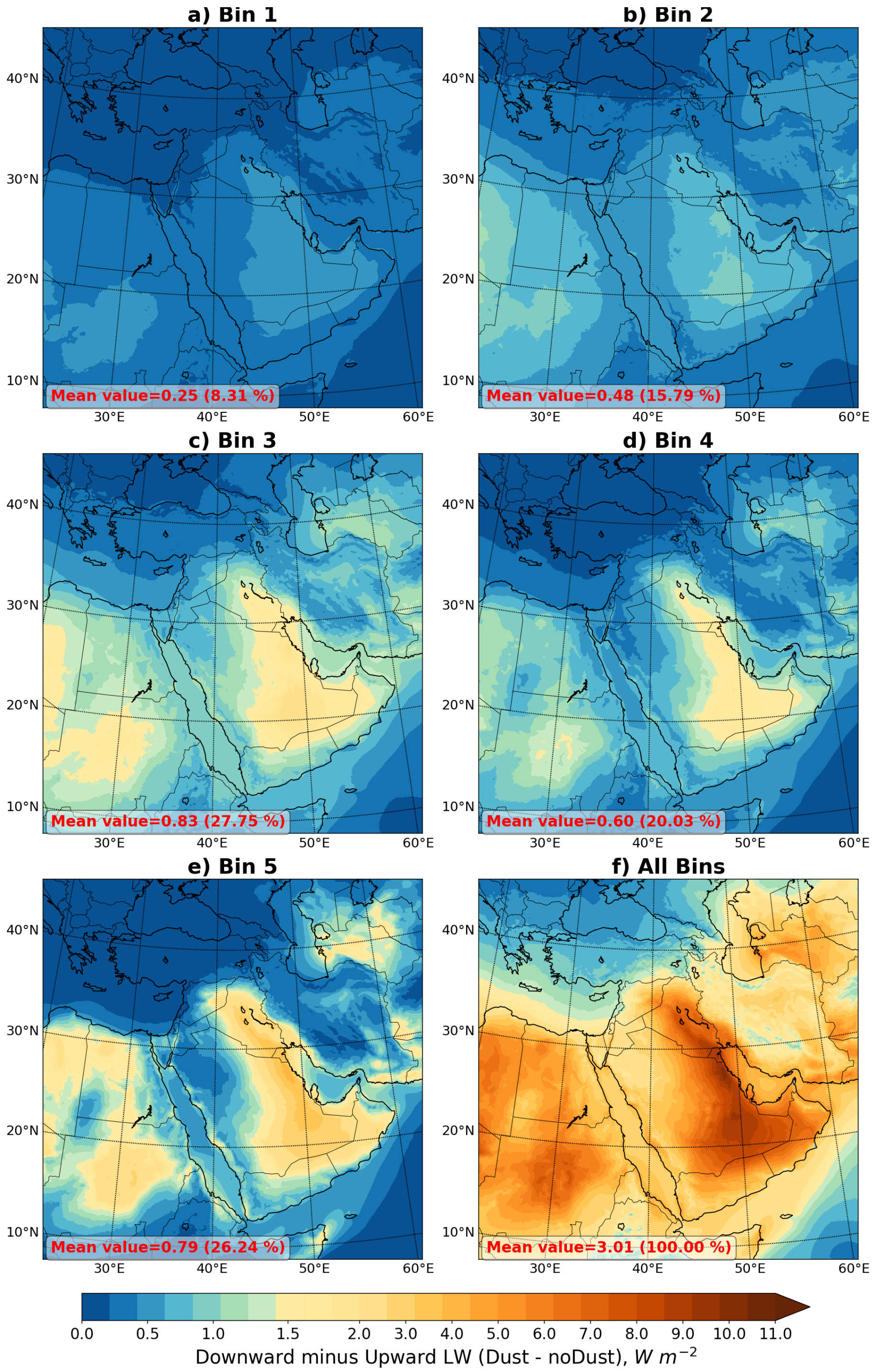

Figure 9: Annual mean clear-sky LW dust radiative forcing (Wm^{-2}) at the surface caused by the individual bins and calculated in WRF-Chem with the DD constraints for 2016: a) Bin 1, b) Bin 2, c) Bin 3, d) Bin 4, e) Bin 5, and f) all Bins. The area average forcing and relative contributions of each bin are shown at the bottom of each panel.

where $\tau(r^*)$ and $\Delta F(r^*)$ are the SW or LW optical depth and RF generated by dust particles with r < r*, respectively. In equation (2), the partial RF in the numerator (which

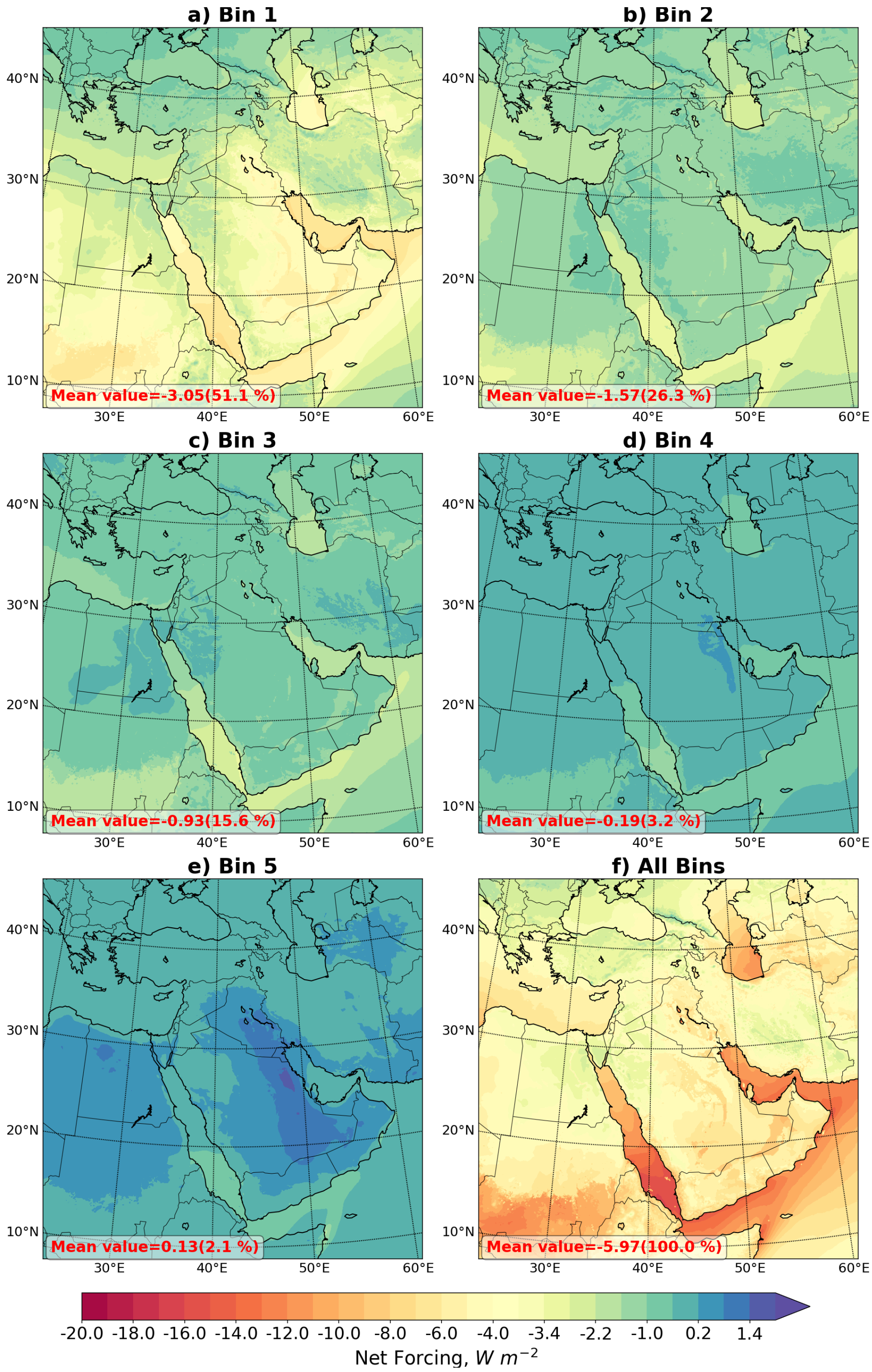

Figure 10: Annual mean clear-sky net (SW+LW) dust radiative forcing ($W\ m^{-2}$) at the surface caused by the individual bins and total calculated in WRF-Chem with the DD constraints for 2016: a) Bin 1, b) Bin 2, c) Bin 3, d) Bin 4, e) Bin 5, and f) all Bins. The area average RF and relative contributions of each bin are shown at the bottom of each panel.

accounts only for a fraction of dust particles with $r < r^*$) is normalized by the total RF

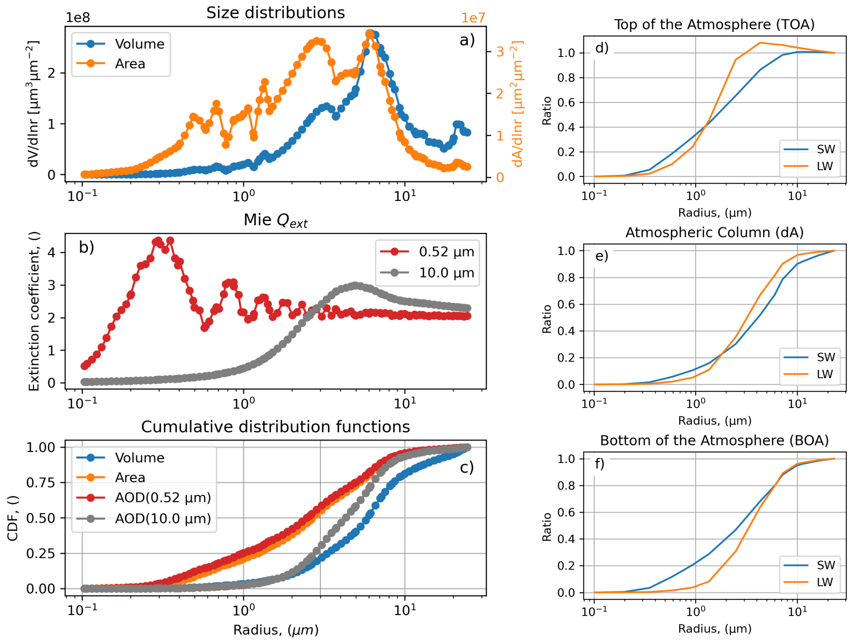

Figure 11: Size-resolved microphysical and optical properties of dust, and the RF. The left column shows: a) dust volume size distribution and surface area; b) SW and LW extinction cross-sections; and c) cumulative distribution functions of the dust total volume, surface area, and AOD (bottom). The cumulative distribution functions of volume, surface area, and AOD are normalized (to their maximum value) to show the relative contribution of all the particles in the size distribution up to the radius r. The right column shows the relative contribution of dust particles up to radius r to dust SW and LW RFs (i.e., ΔF_{CDF} in equation 2) at the d) top of the atmosphere (TOA), f) the bottom of the atmosphere (BOA) and e) dust absorption within the atmospheric column (dA).

(integrated over the entire radii range), which results in a relative contribution of dust particles up to a size r* (normalized CDF). Similarly, we define the CDFs of the aerosol optical properties: extinction coefficients ϵ, ϵ_{CDF}, scattering coefficient ϵ_S, single scattering albedo ω_{CDF}:

$$\epsilon(r^*) = \int_0^{r^*} Q(r)\frac{dN}{dr}\,dr \tag{4}$$

$$\epsilon_S(r^*) = \int_0^{r^*} Q_S(r)\frac{dN}{dr}\,dr \tag{5}$$

$$\tau(r^*) = \int_0^{\infty} \epsilon(r^*)\,dz \tag{6}$$

$$\omega_{CDF}(r^*) = \epsilon_S(r^*)/\epsilon(r^*) \tag{7}$$

$$\epsilon_{CDF}(r^*) = \frac{\int_0^{r^*} Q(r)\frac{dN}{dr}\,dr}{\int_0^{\infty} Q(r)\frac{dN}{dr}\,dr} \tag{8}$$

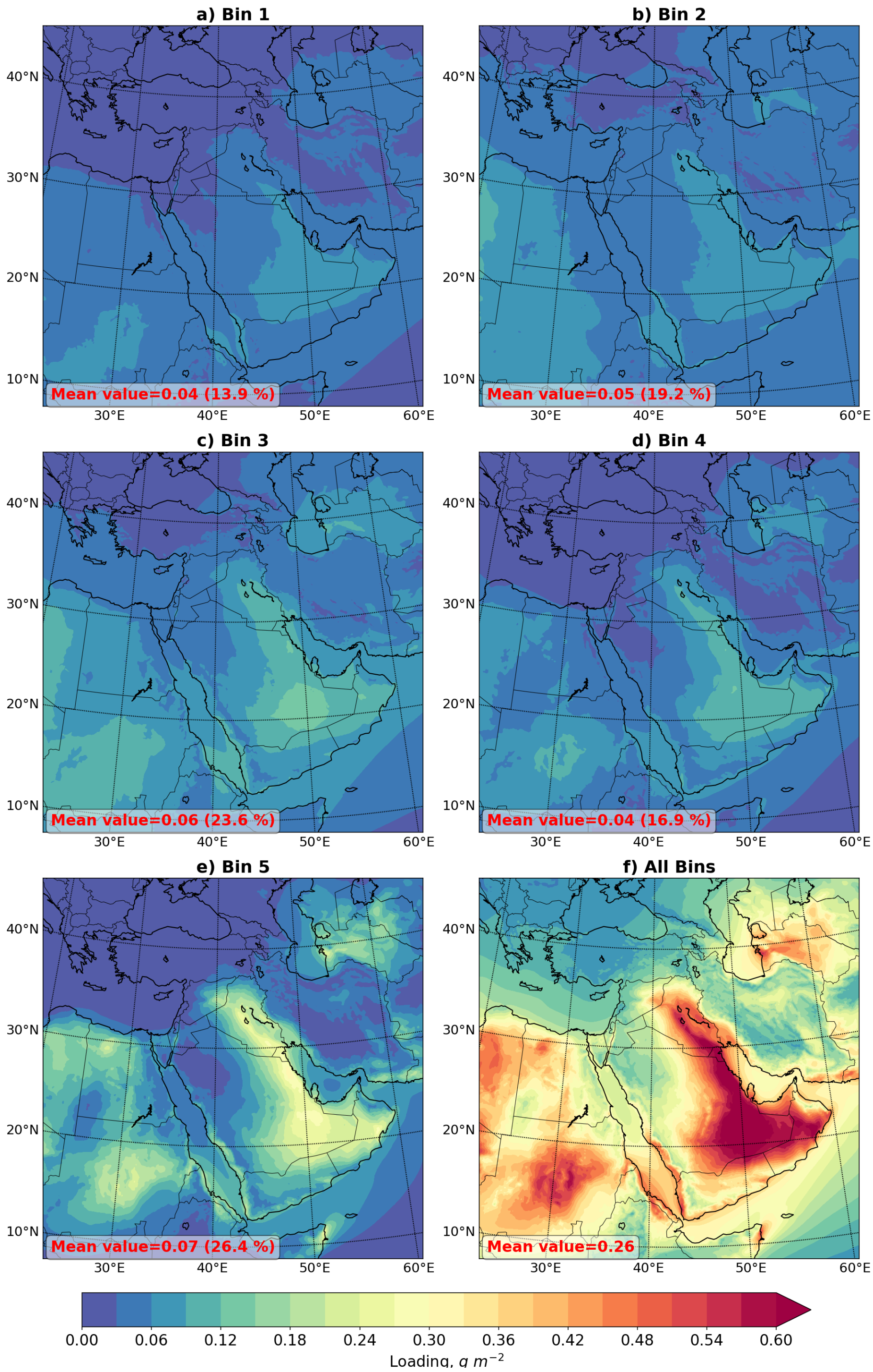

Figure 12: Annual mean column integrated dust concentration, DL ($g\ m^{-2}$) of the individual dust bins and total calculated in WRF-Chem with the DD constraints for 2016: a) Bin 1, b) Bin 2, c) Bin 3, d) Bin 4, e) Bin 5, and f) all Bins. The area average values for each bin and their relative contributions are shown at the bottom of each panel.

where $Q(r)$ and $Q_S(r)$ are the extinction and scattering cross-sections for individual particles with radius r. dN/dr is number-density dust PSD. The spectral dust optical properties (Figure S1) and corresponding CDFs (Figure S2) are available in the Supplementary section.

The standalone 1D analysis (Figure 11a-c) corroborates the conclusions of the WRF-Chem modeling. We resolve the contributions of dust particles of various sizes to the physical, optical, and radiative properties of atmospheric dust. In particular, we found that fine dust with $r < 3\mu m$ constitutes 20% of the total mass but more than 50% of the total cross-section and surface area (i.e., the properties that modulate the radiative transfer and heterogeneous chemistry on the surface of the particles), 60% of the visible DOD, and 25% of DOD in LW. Dust with r $< 10\mu m$ explains 75% of the dust loading in the column and > 90% of the 0.52 μm and 10 μm AODs. Furthermore, the particles with $r > 3\mu m$ explain 75% of DOD in longwave.

Figure 11d-f confirms that giant dust particles with r > 10 μm contribute less than 10% in the SW and LW ΔF_{CDF} either at the top of the atmosphere (TOA), the bottom of the atmosphere (BOA), or atmospheric absorption (dA). Dust particles with 6 $\mu m <$ r < 10 μm, for which the radiative effect was virtually absent previously due to model error, account for 10% of the surface SW and LW RFs, relevant for the impact on solar panels, and 5-7% of SW and LW dA, relevant for the climate and circulation effects. Large particles with r > 6 μm, that are now represented in bin 5, account for at least 40% of total dust mass suspended in the atmosphere, which is consistent with our results (see Figure 4d) showing that bin 5 accounts for about 30% of dust mass suspended in the atmosphere (at the KAUST Campus). The dust SW and LW RFs tend to cancel each other out at the surface, but SW and LW dust absorption in the atmosphere enhances each other, thus producing stronger atmospheric warming.

3.3 Effect of Fine and Coarse Dust on DE, DD, and DL

Dust is generated across almost the entire Arabian Peninsula, where the source function $S > 0$ (see Figure 1). The most intensive dust generation occurs in the eastern and south-eastern parts of the Arabian Peninsula, where S reaches its maximum value of 0.45. In the absence of rain, dry deposition and gravitational sedimentation are the primary mechanisms of dust deposition in desert regions (Mahowald et al., 2011; Adebiyi et al., 2023).

Fig. 12 shows column-integrated atmospheric DL for each bin and all bins. The distribution of all-bin loading is similar to that of DOD. The larger total loadings up to 0.6 $g\ m^{-2}$ are observed in the eastern Arabian Peninsula, the Rub Al Khali desert, and the southern Red Sea. The domain average annual mean loading in different bins varies from 0.04 gm^{-2} (in bin 1) to 0.07 gm^{-2} in bin 5. Bin 5, representing coarse and giant dust with r > 6 μm, incorporates 26% of total DL (consistent with (J. Meng et al., 2022; Kok et al., 2021; Adebiyi & Kok, 2020; Adebiyi et al., 2023)), although it receives 73% of total DE. The gravitational settling of coarse dust particles in bin 5 is so rapid that few remain suspended in the atmosphere even over the regions where they are generated in large quantities (eastern Arabian Peninsula, Rub Al Khali desert), confirming that DL is less sensitive to the emission of coarse and giant particles than, for example, DD.

The mean seasonal dust emission rates averaged over the dust source regions (i.e., Arabian Peninsula, Central Asia and Iran, and East Africa, excluding the seas) is shown in Figure 13. The largest DE is in Spring and Summer. The Arabian Peninsula and East Africa emit twice as much dust compared to the Central Asia and Iran regions. In Summer, the Arabian Peninsula emits more dust than other sub-regions within the domain because the northwesterly winds, Shamal, that blow over the Arabian Peninsula cause frequent dust outbreaks (Rashki et al., 2019; Yu et al., 2016; Patlakas et al., 2019). The Central Asia and Iran sub-region exhibits the maximum emission rate in summer (28.8 $Mt\ mo^{-1}$) and minimum in winter (20.5 $Mt\ mo^{-1}$). The annual dust emission from the entire domain tripled in our current simulations in comparison with those not accounting for the generation of giant dust particles.

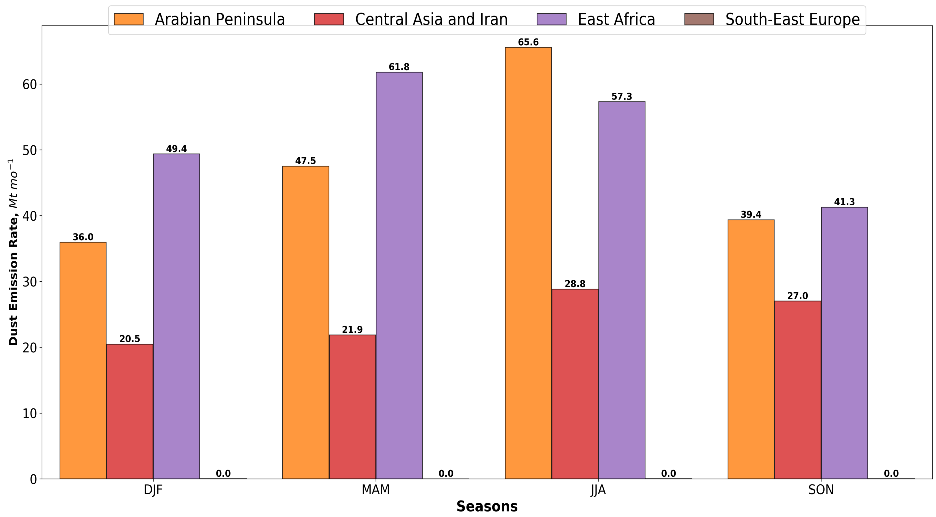

Figure 13: Seasonal mean dust emission rates ($Mt\ mo^{-1}$) calculated in WRF-Chem with the DD constraints for 2016 for four seasons (DJF, MAM, JJA, SON) integrated over the selected sub-regions: Arabian Peninsula (light brown), central Asia and Iran (red), east Africa (violet), and south-east Europe (dark brown bar is too small to be visible).

Figure S3 (see the supplementary information) shows the spatial distribution of dust deposition over the Arabian Peninsula for four seasons. Consistent with the seasonal pattern of DE, the largest seasonally integrated DD occurs in summer and spring. Overall, dust deposition rates in the eastern Arabian Peninsula are much higher than in the western Arabian Peninsula. The largest simulated deposition rates are observed in Oman, exceeding 20 $g\ m^{-2}\ mo^{-1}$, which is at least three times higher than in the Red Sea coastal plain.

Figure 14 shows the spatial distribution of the annual mean deposition over the Arabian Peninsula produced by dust from different bins. Annually, 446 Mt of dust is deposited in the Arabian Peninsula, with bin 5 being a major contributor (377 Mt). Fine particles in bins 1 and 2 (r $< 1.8\ \mu m$) are deposited almost uniformly over the entire region. Most of the coarse particles in bin 5, however, deposit close to the source regions where they were emitted, resembling the spatial patterns of the source function S (see Fig. 1). However, we also observe significant deposition of coarse and giant particles in the regional seas.

Dust deposition plays a key role in the geochemical cycles in the oceans and seas (Fan et al., 2006; Martin, 1990; Sunda & Huntsman, 1997; Watson et al., 2000; Mahowald et al., 2011). The dust released into the ocean feeds marine ecosystems and increases their productivity. The chemicals brought by dust deposition are particularly important in seas with little perennial freshwater discharge, such as the Red Sea (Jish Prakash et al., 2015).

Figure S4 (see the supplementary information) shows the seasonal spatial distribution of dust deposited in the Red Sea. The maximum deposition rate (5-6 $g\ m^{-2}\ mo^{-1}$) occurred within 10 km of the coastline due to proximity to dust sources. Away from the coast, except during summer in the southern Red Sea, the rate of dust deposition de-

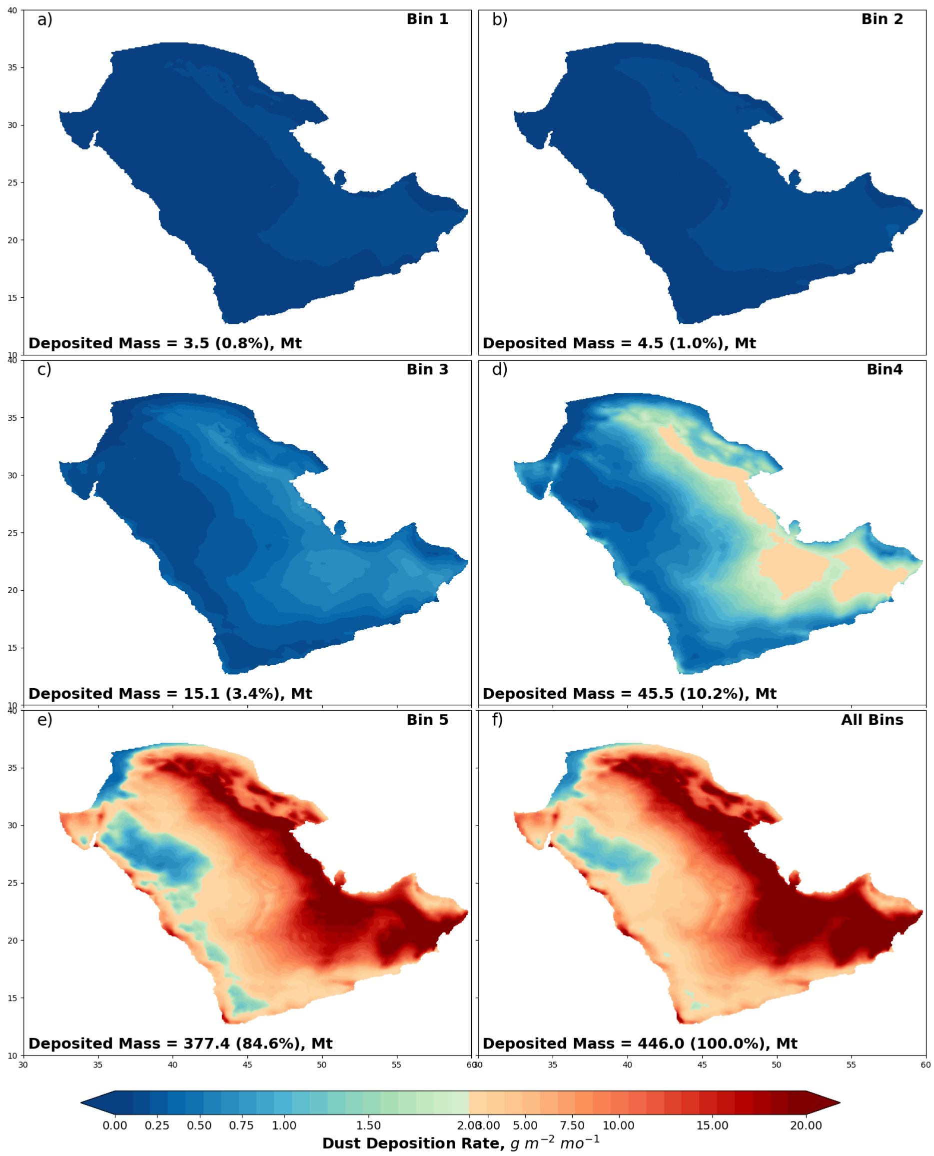

Figure 14: Annual mean dust deposition rate $g\ m^{-2}\ mo^{-1}$ calculated in WRF-Chem with the DD constraints for 2016 over the Arabian Peninsula caused by the individual and total: a) Bin 1; b) Bin 2; c) Bin 3; d) Bin 4; e) Bin 5; and f) all Bins. The spatially integrated mass of deposited dust for each bin and its relative contribution are shown in each panel at the bottom.

creases. The maximum dust deposition in the Red Sea (7.9 Mt) occurs in the months June-August (JJA; see Figure S4c) when the north African monsoonal circulation transports dust from Africa's Bodele Depression through the Tokar Mountain Gap (Kalenderski & Stenchikov, 2016). The Northerly winds, prevailing in Summer, push dust to the southern Red Sea where it is trapped by high coastal mountain ranges so that AOD reaches 1 (Osipov & Stenchikov, 2018). The minimum DD over the Red Sea is observed in Fall (SON), when it decreases to 3.2 Mt.

The annual average DD rates in the Red Sea for the individual bins and total are shown in Figure 15. The total annual DD in the Red Sea is 19.8 Mt, predominantly produced by dust in bin 5 (15.3 Mt). The deposition rate of coarse particles is 3-4 times smaller in central sea compared to the near-shore areas. The fine particles in bins 1 and 2 contribute 4% of deposited mass, which is uniformly distributed over the Red Sea area. The total DD rate varies from 7 $g\ m^{-2}\ mo^{-1}$ near the coasts to 1 $g\ m^{-2}\ mo^{-1}$ in the central Red Sea, which is hardly reachable by coarse dust. Overall, giant dust deposition in the Red Sea is 2.5 times higher when compared with simulations without DD tuning (Shevchenko et al., 2021).

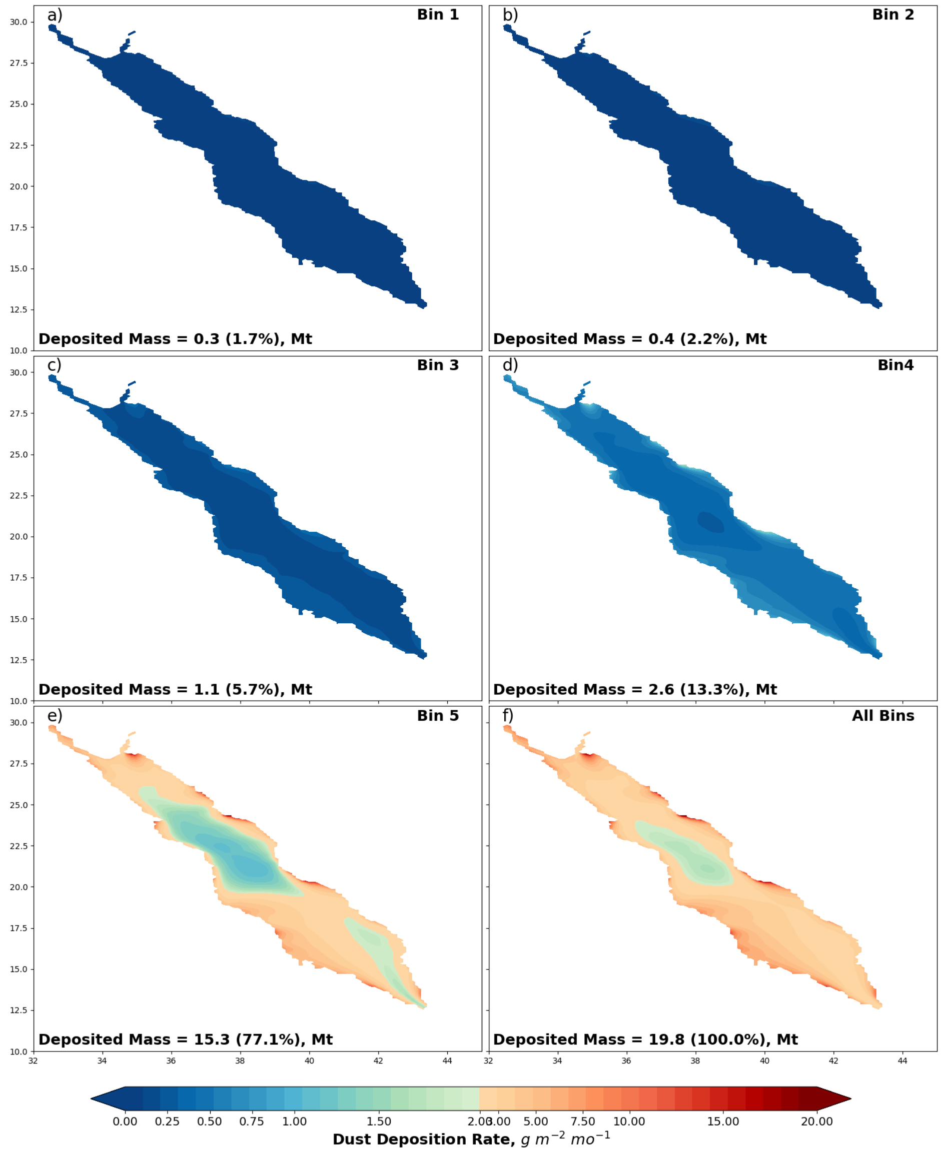

Figure 15: Annual mean dust deposition rate ($g\ m^{-2}\ mo^{-1}$) in the Red Sea calculated in WRF-Chem with the DD constraints for 2016 caused by the individual dust bins and total: a) Bin 1; b) Bin 2; c) Bin 3; d) Bin 4; e) Bin 5; and f) all Bins. The spatially integrated mass of deposited dust for each bin and its relative contribution is shown in each panel at the bottom.

The seasonal spatial deposition rate over the Arabian Gulf is shown in Figure S5 (see the supplementary information). The maximum deposition is observed in summer (JJA - Figure S5c), reaching 5.5 Mt. Deposition reduces to a minimum of 2.1 Mt in winter (DJF - Figure. S5a). The maximum dust deposition rates, similar to the Red Sea, are along the coastlines in the vicinity of the primary dust sources. The Arabian Gulf receives dust from the eastern Arabian Peninsula, Iraq, the Omani coast, and the western part of Iran.

Figure 16 shows the spatial distribution of annual dust deposition over the Arabian Gulf contributed by the different bins and total, which is 14.1 Mt. The total annual average deposition rate varies from 10 $g\ m^{-2}\ mo^{-1}$ in the north-western and western coastal areas to 1.0 $g\ m^{-2}\ mo^{-1}$ in the central Arabian Gulf (Figure 16f). This deposition rate is about 25% higher than in the Red Sea. Similarly to the Red Sea, the coarse dust particles in bin 5 contribute 76.1% to the dust deposition, and the finest bins 1 and 2 contribute only 3.5%.

Annual deposition over the Arabian Sea within our computational domain is about 14 Mt, with an average rate of 4.9 $g\ m^{-2}\ mo^{-1}$. However, in summer, there are areas with a dust deposition rate above 34.2 $g\ m^{-2}\ mo^{-1}$ located in the northwestern Arabian Sea and along its northern coastline caused by the seasonal intensification of local north-westerly winds and Indian Monsoon circulation. In addition, the Somali jet associated with the southwestern Indian monsoon transports dust from Somalia's deserts to the Arabian Sea in summer (Tindale & Pease, 1999).

Figure 17 shows seasonal deposition rates averaged over the selected regions indicating contributions of coarse dust. In all seasons over land (excluding the southeast Europe region), coarse and giant dust comprises more than 90% of the total deposited dust mass. Over the regional seas, however, fine dust contribution is more than 20%. Thus, the relative contribution of fine dust to DD is twice as large over the seas as the land areas because coarse dust particles predominantly deposit in the coastal areas.

4 Impact of Coarse and Fine Dust on Solar Devices

The Middle East receives a huge amount of solar radiation. For example, the 500× 500 km^2 area in the Saudi desert receives enough solar energy to cover the entire global energy consumption. Dust, however, could significantly hamper the efficiency of solar devices and must be accounted for.

Dust and other aerosols have two main impacts on solar devices. Firstly, aerosols suspended in the atmosphere attenuate solar radiation reducing the downward solar flux at the surface by 12 $W\ m^{-2}$ on average (see Fig. 18). Secondly, dust and other aerosols deposit on the optically active surfaces of solar devices, causing power loss due to soiling (Ilse, Figgis, Werner, et al., 2018; Ilse et al., 2016; Ilse, Figgis, Naumann, et al., 2018; Figgis et al., 2017; Baras et al., 2016; Boyle et al., 2013; Sayyah et al., 2014)

We define the effect of dust as the relative energy loss due to dust deposited on the surfaces of a solar device, e.g., solar PV panels, or because dust attenuates the incoming solar flux when suspended in the atmosphere. Considering the solar devices with a constant radiation-to-electricity conversion coefficient, we can formulate the losses as a relative decrease of incoming solar radiation caused by dust. Thus soiling losses (SL) and attenuation losses (AL) could be calculated in the following way:

$$SL = \frac{E_0 - E_s}{E_0} \times 100\% = \frac{\Delta E_s}{E_0} \times 100\% \tag{9}$$

$$AL = \frac{E_0 - E_a}{E_0} \times 100\% = \frac{\Delta E_a}{E_0} \times 100\% \tag{10}$$

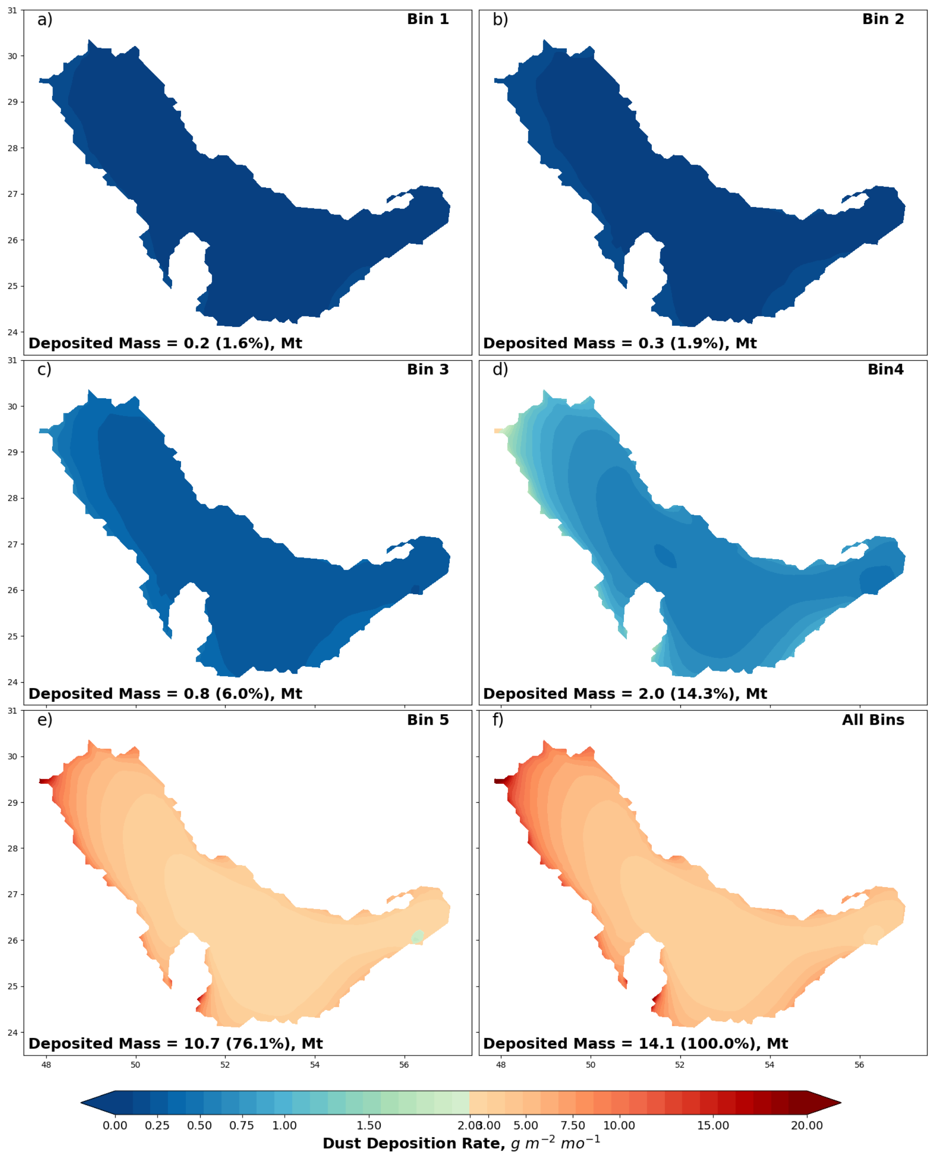

Figure 16: Annual mean dust deposition rate ($g\ m^{-2}\ mo^{-1}$) in the Arabian Gulf calculated in WRF-Chem with the DD constraints for 2016 caused by the individual dust bins and total: a) Bin 1; b) Bin 2; c) Bin 3; d) Bin 4; e) Bin 5; and f) all Bins. The spatially integrated mass of deposited dust for each bin and its relative contribution is shown in each panel at the bottom.

where E_0, E_s, and E_a are, respectively, daily solar energy received by a clean device in a clean atmosphere, the soiled device in a clean atmosphere, and a clean device in a dusty atmosphere. ΔE_s and ΔE_a are, respectively, the solar energy loss due to soiling and attenuation.

The total loss (TL) can be calculated as the sum of soiling and attenuation losses:

$$TL = SL + AL \tag{11}$$

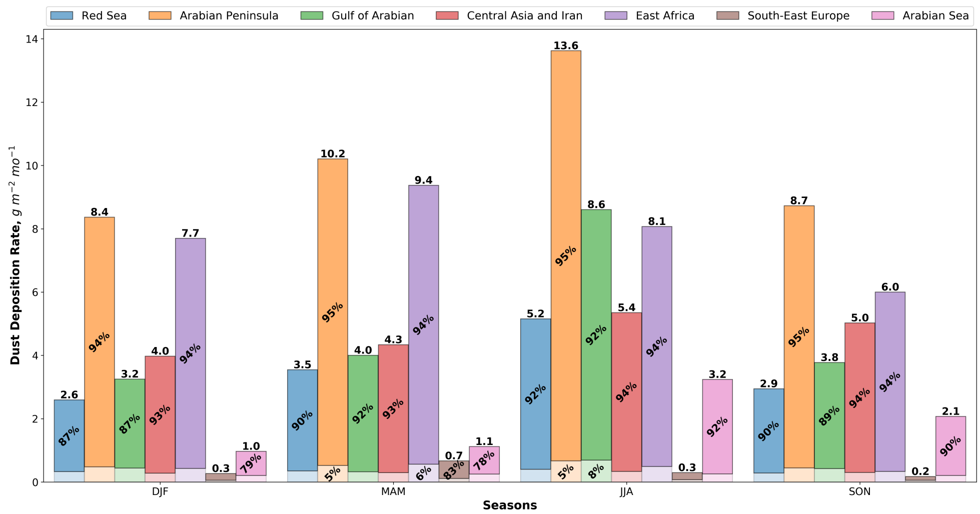

Figure 17: Seasonal mean dust deposition rate ($g\ m^{-2}\ mo^{-1}$) in the seven selected regions calculated in WRF-Chem with the DD constraints for 2016. From bottom to top, the color grading shows the contribution of fine (sum of bins 1-3) and coarse (sum of bins 4-5) dust particles (see Table 1).

Here, we use the assessments of dust radiative effect and DD rates obtained in this study to estimate SL and AL. Figure 18 demonstrates the effect of dust on the downward solar flux at the surface. The average change of solar radiation over the domain is 12.13 $W\ m^{-2}$, but locally it reaches 30 $W\ m^{-2}$. The finest three bins with r < 3 μm produce about 90% of this effect. Thus, the average daily attenuation loss in the chosen domain $AL = 4.75\%$ but locally exceeds 11 %. Specifically, for the KAUST site in summer, this is $AL = 5\%$ (see Figure 18a).

Soiling losses depend on the amount of deposited dust. Our analysis shows that coarse dust comprises most of the deposited mass. Valerino et al. (2020) conducted a comprehensive analysis, measuring soiling loss per unit deposited mass. According to their measurements conducted in Gandhinagar (Gujarat, India), soiling loss is 5-6% per 1 $g\ m^{-2}$ of material deposited on the PV surfaces. This is a useful way to assess soiling, allowing us to scale the soiling loss against corresponding deposition rates.

To interpret their results, Valerino et al. (2020) assumed that the radiative effect of aerosols deposited on the surface of a PV panel would be the same as if they were suspended in the atmosphere. This assumption led to the conclusion that fine particles produce the greatest soiling effect. However, deposited particles are densely packed on the surface of a PV panel, and the Mie theory assumptions (large distances between particles preventing their optical interactions), assumed by Valerino et al. (2020), cannot be satisfied. Here, we suggest a different physical model, assuming that deposited particles make a uniform layer over a solar panel surface. Knowing the refractive index of deposited material, we can calculate the SL per unit deposited mass of 1 $g\ m^{-2}$.

In our simulations, the main deposited material is dust with density $d = 2500\ kg\ m^{-3}$, and refractive index.

$$R_i = n + i \times \chi \tag{12}$$

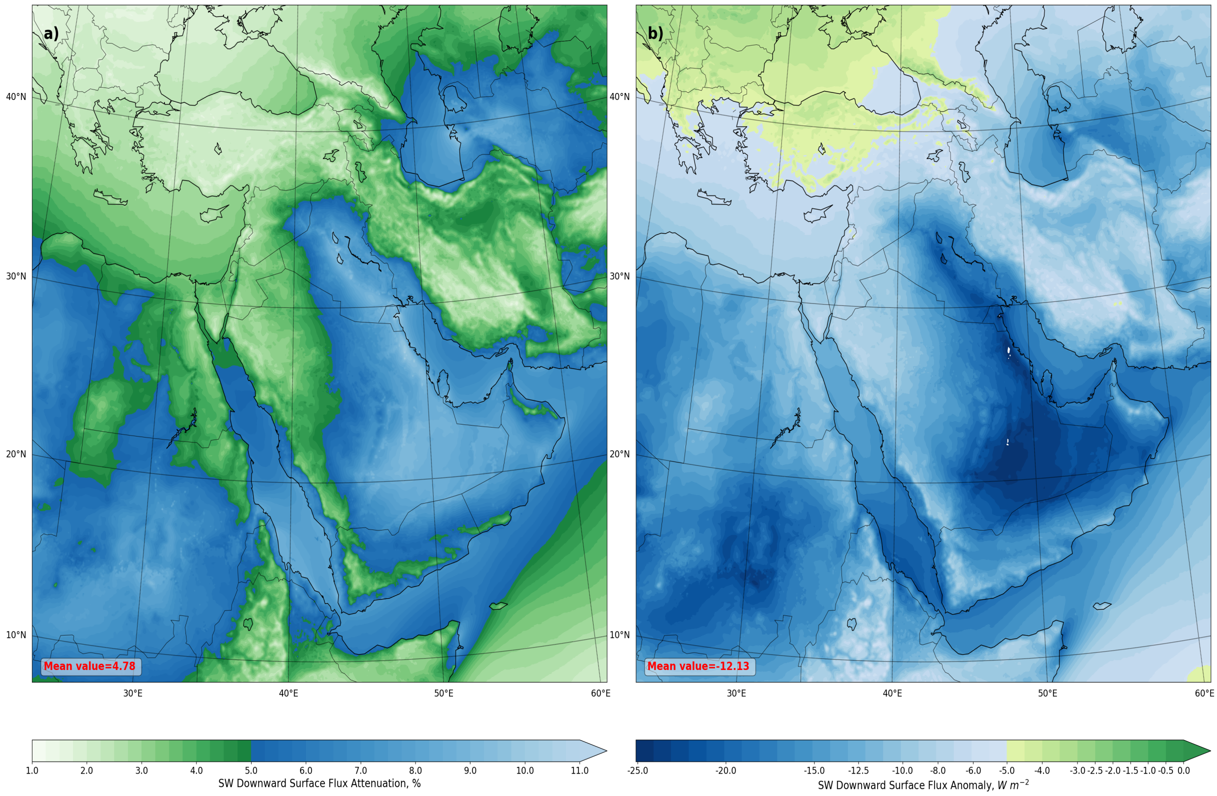

Figure 18: Annual mean dust-caused downward SW radiative flux anomaly at surface calculated in WRF-Chem with the AOD and DD constraints for 2016. a) Normalized to its annual mean value (%); b) Absolute value ($W\ m^{-2}$) The spatially averaged value is shown at the bottom of the panel.

Where the real part of the refractive index is $n = 1.55$, and the imaginary part is $\chi = 0.003$. The depth of the deposited layer with a mass of 1 $g\ m^{-2}$ $h = 0.4\ \mu m$, the following relation gives us the soiling loss (Landau et al., 2013):

$$SL = \frac{4\pi n \chi h}{\lambda} \times 100\% \tag{13}$$

where λ is a characteristic wavelength of solar light. Assuming $\lambda = 0.55\ \mu m$ for the most energetic visible light, we obtain $SL = 4.25\%$, consistent with the measurements conducted by Valerino et al. (2020). However, in this case, we have to conclude that the largest contribution to soiling is from large particles that comprise most of the deposited mass.

The deposition of dust particles on the surface of a PV panel is a complex process that depends on meteorological conditions (Ilse, Figgis, Naumann, et al., 2018), the tilt of a panel (Boyle et al., 2013), dust mineralogy (Engelbrecht et al., 2017), the presence of water, and adhesion forces between a panel and dust particles (Ilse, Figgis, Naumann, et al., 2018). The detailed analysis of these processes is beyond the scope of this paper, but we can estimate the upper limit of the soiling effect. We assume that a PV panel is oriented horizontally and all deposited material is retained on its surface. The average deposition, e.g., at the KAUST site, is about 3 $qm^{-2}week^{-1}$ (Shevchenko et al., 2021). Therefore, the average soiling loss $SL = 12.75\%$ for a weekly cleaning schedule assumes linear dependence of SL on the deposited mass and temporarily uniform accumulation of material on PV surfaces. Accounting for the attenuation losses $AL = 5\%$, we can expect that the total loss of efficiency of the solar panels on the west coast of Saudi Arabia (on a weekly cleaning schedule) would be $TL = 17 - 18\%$ for the areas similar to the KAUST campus. According to our simulations, the deposition rates on the east coast of the Arabian Peninsula are at least three times higher than on the west coast. Therefore, for those areas, the dust-related losses could be projected to TL=45% (assuming a weekly cleaning schedule).

5 Conclusions

In desert regions like the ME, dust is an important climate factor as it significantly attenuates solar radiation at the surface and heats the atmospheric column (Osipov et al., 2015). We evaluated the radiative dust effect and deposition rates in the ME using the free-running WRF-Chem model.

Observations show that large particles with r > 10 μm contribute the most mass in dust deposition. However, the deposited dust mass was underestimated by 2-3 times because the up-to-date models (free-running and used in data assimilation) underrepresented the content of coarse and giant dust in the atmosphere. Therefore, we approximate the effect of giant dust with r > 10 μm by increasing the emission of coarse particles in bin 5 with 6 μm < r < 10 μm. This approach compensates for the suspected model overestimation of the giant dust deposition rate. For the first time, we simultaneously constrained the model simulations by DD and AERONET AOD observations by using dust deposition observations collected on the Red Sea coast with passive dust deposition samplers (Shevchenko et al., 2021). We specifically quantified the effect of dust particles of different sizes on dust RF and mass deposition.

The annual mean area average reduction of SW surface flux reaches 9 $W\ m^{-2}$, but regionally solar surface cooling exceeds 30 $W\ m^{-2}$. Dust-induced LW warming partly compensates for SW cooling so that domain averaged dust annual mean net RF is reduced to - 5.72 $W\ m^{-2}$, but regionally net radiative cooling reaches 20 $W\ m^{-2}$. Annually, non-dust aerosols contribute, on average, about 20% to AOD and RF over land. In the urban centers and areas affected by sulfur emissions and sea salt intrusions, however, the non-dust aerosols' contribution to solar flux reduction increases to > 30%. Fine dust particles with radii r < 3 μm produce about 90% of the net clear-sky SW RF at the surface, while the SW contribution of the coarsest particles with r > 6 μm is < 10%. Conversely, giant and coarse particles dominate the effect on DD and DE. Accounting for giant dust particles and simultaneously fitting the DD and visible AOD observations led to a tripling of DE compared to the simulations without the DD constraints; consequently, DD increases over land 3 times and over regional seas 2.5 times. The fine dust deposition fraction (compared to the coarse dust fraction) in the seas is twice as large than over land because most of the coarse dust particles deposit within the narrow coastal area.

Dust suspended in the atmosphere significantly affects the functioning of solar devices by reducing the downward solar flux and efficacy of solar panels by an average of 5% over the domain. Dust deposition on solar devices is another factor that affects their functionality. Based on the annual average dust deposition rate, the soiling losses could reach 12% per week on the west coast and could be up to three times higher on the East Coast. Fine dust is predominantly responsible for solar light attenuation, but coarse dust particles play a major role in deposition and soiling.

Fitting visible AOD helps to constrain the emission of fine dust, whereas fitting DD constrains the emission of coarse dust. Approximating the giant dust with coarse dust leads to marginally stronger cooling in SW and a slight overestimation of warming in LW (see Figure 11). The SW and LW effects of giant dust almost cancel each other out at the surface, but their SW and LW absorption in the atmosphere enhance their heating of the atmospheric column. Overall, our results are consistent with recent studies (J. Meng et al., 2022; Kok et al., 2017; Adebiyi et al., 2023) and highlight that coarse dust particles underrepresented in the up-to-date models contribute to atmospheric loading by about 25%. At the same time, we found that DD and DE triple in the experiments constrained by AOD and DD, while the radiative effect of giant dust does not exceed 10%. Accounting for giant dust, as suggested in this study, allows us to reach an agreement between the model results and the available observations. Dust deposition data appear to be a valuable asset that, together with AOD, allows model performance to be rectified. Expansion of the network of dust deposition observations is necessary to improve dust modeling and forecasting further.

Acknowledgments

The research reported in this publication was supported by funding from King Abdullah University of Science and Technology (KAUST) through the Competitive Research Grant (URF/1/2180-01-01) “Combined Radiative and Air Quality Effects of Anthropogenic Air Pollution and Dust over the Arabian Peninsula,” and the ACWA Power industrial grant RGC/3/5274-01-01 "Development of a Soiling Map for the GCC region." This research used the resources of the Supercomputing Laboratory at KAUST.

References

Abdou, W. A., Diner, D. J., Martonchik, J. V., Bruegge, C. J., Kahn, R. A., Gaitley, B. J., … Holben, B. (2005). Comparison of coincident multiangle imaging spectroradiometer and moderate resolution imaging spectroradiometer aerosol optical depths over land and ocean scenes containing aerosol robotic network sites. *Journal of Geophysical Research: Atmospheres*, *110*(D10).

Adebiyi, A., Kok, J., Murray, B., Ryder, C., Stuut, J., Kahn, R., … others (2023). *A review of coarse mineral dust in the earth system* (Vol. 60). Elsevier.

Adebiyi, A., & Kok, J. F. (2020). Climate models miss most of the coarse dust in the atmosphere. *Science advances*, *6*(15), eaaz9507.

Anisimov, A., Axisa, D., Kucera, P. A., Mostamandi, S., & Stenchikov, G. (2018). Observations and cloud-resolving modeling of haboob dust storms over the arabian peninsula. *Journal of Geophysical Research: Atmospheres*, *123*(21), 12–147.

Balkanski, Y., Schulz, M., Claquin, T., & Guibert, S. (2007). Reevaluation of mineral aerosol radiative forcings suggests a better agreement with satellite and aeronet data. *Atmospheric Chemistry and Physics*, *7*(1), 81–95.

Baras, A., Jones, R. K., Alqahtani, A., Alodan, M., & Abdullah, K. (2016). Measured soiling loss and its economic impact for pv plants in central saudi arabia. In *2016 saudi arabia smart grid (sasg)* (pp. 1–7).

Bergametti, G., & Forêt, G. (2014). *Dust deposition.* Springer.

Bergin, M. H., Ghoroi, C., Dixit, D., Schauer, J. J., & Shindell, D. T. (2017). Large reductions in solar energy production due to dust and particulate air pollution. *Environmental Science & Technology Letters*, *4*(8), 339–344.

Boucher, O., Pham, M., & Venkataraman, C. (2002). *Simulation of the atmospheric sulfur cycle in the laboratoire de météorologie dynamique general circulation model: Model description, model evaluation, and global and european budgets.* Inst. Pierre Simon Laplace des Sciences de l'Environnement Global.

Boyle, L., Flinchpaugh, H., & Hannigan, M. (2013). Impact of natural soiling on the transmission of pv cover plates. In *2013 ieee 39th photovoltaic specialists conference (pvsc)* (pp. 3276–3278).

Boyle, L., Flinchpaugh, H., & Hannigan, M. (2015). Natural soiling of photovoltaic cover plates and the impact on transmission. *Renewable Energy*, *77*, 166–173.

Bozzo, A., Remy, S., Benedetti, A., Flemming, J., Bechtold, P., Rodwell, M., & Morcrette, J.-J. (2017). *Implementation of a cams-based aerosol climatology in the ifs.* European Centre for Medium-Range Weather Forecasts.

Buchard, V., Randles, C., Da Silva, A., Darmenov, A., Colarco, P., Govindaraju, R., … others (2017). The merra-2 aerosol reanalysis, 1980 onward. part ii: Evaluation and case studies. *Journal of Climate*, *30*(17), 6851–6872.

Cakmur, R., Miller, R., Perlwitz, J., Geogdzhayev, I., Ginoux, P., Koch, D., … Zender, C. (2006). Constraining the magnitude of the global dust cycle by minimizing the difference between a model and observations. *Journal of Geophysical Research: Atmospheres*, *111*(D6).

Chadwick, O. A., Derry, L. A., Vitousek, P. M., Huebert, B. J., & Hedin, L. O. (1999). Changing sources of nutrients during four million years of ecosystem development. *Nature*, *397*(6719), 491–497.

Chin, M., Diehl, T., Tan, Q., Prospero, J. M., Kahn, R. A., Remer, L. A., … Zhao, X.-P. (2014). Multi-decadal aerosol variations from 1980 to 2009: a perspective from observations and a global model. *Atmospheric Chemistry and Physics*, *14*(7), 3657–3690. Retrieved from `https://www.atmos-chem-phys.net/14/3657/2014/` doi: 10.5194/acp-14-3657-2014

Chin, M., Ginoux, P., Kinne, S., Torres, O., Holben, B. N., Duncan, B. N., … Nakajima, T. (2002). Tropospheric aerosol optical thickness from the gocart model and comparisons with satellite and sun photometer measurements. *Journal of the atmospheric sciences*, *59*(3), 461–483.

Chin, M., Rood, R. B., Lin, S.-J., Müller, J.-F., & Thompson, A. M. (2000). Atmospheric sulfur cycle simulated in the global model gocart: Model description and global properties. *Journal of Geophysical Research: Atmospheres*, *105*(D20), 24671–24687.

Climate.com. (2018). *Climate of middle east.* Author. Retrieved from `http://climateof.com/middleeast/index.asp`

Darmenova, K., Sokolik, I. N., Shao, Y., Marticorena, B., & Bergametti, G. (2009). Development of a physically based dust emission module within the weather research and forecasting (wrf) model: Assessment of dust emission parameterizations and input parameters for source regions in central and east asia. *Journal of Geophysical Research: Atmospheres*, *114*(D14).

DeMott, P. J., Prenni, A. J., Liu, X., Kreidenweis, S. M., Petters, M. D., Twohy, C. H., . . . Rogers, D. (2010). Predicting global atmospheric ice nuclei distributions and their impacts on climate. *Proceedings of the National Academy of Sciences*, *107*(25), 11217–11222.

Dubovik, O., & King, M. D. (2000). A flexible inversion algorithm for retrieval of aerosol optical properties from sun and sky radiance measurements. *Journal of Geophysical Research: Atmospheres*, *105*(D16), 20673–20696.

El-Shobokshy, M. S., & Hussein, F. M. (1993). Degradation of photovoltaic cell performance due to dust deposition on to its surface. *Renewable energy*, *3*(6-7), 585–590.

Engelbrecht, J. P., Stenchikov, G., Prakash, P. J., Lersch, T., Anisimov, A., & Shevchenko, I. (2017). Physical and chemical properties of deposited airborne particulates over the arabian red sea coastal plain. *Atmospheric Chemistry and Physics*, *17*(18), 11467–11490.

Fan, S.-M., Moxim, W. J., & Levy, H. (2006). Aeolian input of bioavailable iron to the ocean. *Geophysical Research Letters*, *33*(7).

Figgis, B., Ennaoui, A., Ahzi, S., & Rémond, Y. (2017). Review of pv soiling particle mechanics in desert environments. *Renewable and Sustainable Energy Reviews*, *76*, 872–881.

Forster, P., Ramaswamy, V., Artaxo, P., Berntsen, T., Betts, R., Fahey, D. W., . . . others (2007). Changes in atmospheric constituents and in radiative forcing. chapter 2. In *Climate change 2007. the physical science basis.* WMO.

Ginoux, P., Chin, M., Tegen, I., Prospero, J. M., Holben, B., Dubovik, O., & Lin, S.-J. (2001). Sources and distributions of dust aerosols simulated with the gocart model. *Journal of Geophysical Research: Atmospheres*, *106*(D17), 20255–20273.

Ginoux, P., Prospero, J. M., Gill, T. E., Hsu, N. C., & Zhao, M. (2012). Global-scale attribution of anthropogenic and natural dust sources and their emission rates based on modis deep blue aerosol products. *Reviews of Geophysics*, *50*(3).

Gliß, J., Mortier, A., & Schulz, M. (2020). Multi-model evaluation of aerosol optical properties in the aerocom phase iii control experiment, using ground and space based observations from aeronet, modis, aatsr and a merged satellite product as well as surface in-situ observations from gaw sites. In *Egu general assembly conference abstracts* (p. 18390).

Grell, G. A., & Dévényi, D. (2002). A generalized approach to parameterizing convection combining ensemble and data assimilation techniques. *Geophysical Research Letters*, *29*(14), 38–1.

Grell, G. A., Peckham, S. E., Schmitz, R., McKeen, S. A., Frost, G., Skamarock, W. C., & Eder, B. (2005). Fully coupled "online" chemistry within the wrf model. *Atmospheric Environment*, *39*(37), 6957–6975.

Hamidi, M., Kavianpour, M. R., & Shao, Y. (2013). Synoptic analysis of dust storms in the middle east. *Asia-Pacific Journal of Atmospheric Sciences*, *49*(3), 279–286.

Highwood, E., & Ryder, C. (2014). *Mineral dust: A key player in the earth sys-*

tem edited by p knippertz and jb stuut. Dordrecht: Springer) Radiative effects of dust.

Hong, S., Dudhia, J., & Noh, Y. (2003). A new vertical diffusion package with explicit treatment of the entrainment processes, extended abstract. In *International workshop on numerical weather forecast models, japan.*

Huneeus, N., Schulz, M., Balkanski, Y., Griesfeller, J., Prospero, J., Kinne, S., ... others (2011). Global dust model intercomparison in aerocom phase i. *Atmospheric Chemistry and Physics*, *11*(15), 7781–7816.

Iacono, M., Levinson, D., & El-Geneidy, A. (2008). Models of transportation and land use change: A guide to the territory. *Journal of Planning Literature*, *22*(4), 323–340.

Ilse, K., Figgis, B. W., Naumann, V., Hagendorf, C., & Bagdahn, J. (2018). Fundamentals of soiling processes on photovoltaic modules. *Renewable and Sustainable Energy Reviews*, *98*, 239–254.

Ilse, K., Figgis, B. W., Werner, M., Naumann, V., Hagendorf, C., Pöllmann, H., & Bagdahn, J. (2018). Comprehensive analysis of soiling and cementation processes on pv modules in qatar. *Solar Energy Materials and Solar Cells*, *186*, 309–323.

Ilse, K., Werner, M., Naumann, V., Figgis, B. W., Hagendorf, C., & Bagdahn, J. (2016). Microstructural analysis of the cementation process during soiling on glass surfaces in arid and semi-arid climates. *physica status solidi (RRL)–Rapid Research Letters*, *10*(7), 525–529.

Janssens-Maenhout, G., Pagliari, V., Guizzardi, D., & Muntean, M. (2013). Global emission inventories in the emission database for global atmospheric research (edgar)–manual (i). *Gridding: EDGAR emissions distribution on global gridmaps, Publications Office of the European Union, Luxembourg*.

Jish Prakash, P., Stenchikov, G., Kalenderski, S., Osipov, S., & Bangalath, H. (2015). The impact of dust storms on the arabian peninsula and the red sea. *Atmospheric Chemistry and Physics*, *15*(1), 199–222.

Jish Prakash, P., Stenchikov, G., Tao, W., Yapici, T., Warsama, B., & Engelbrecht, J. P. (2016). Arabian red sea coastal soils as potential mineral dust sources. *Atmospheric Chemistry and Physics*, *16*(18), 11991–12004.

Kalenderski, S., & Stenchikov, G. (2016). High-resolution regional modeling of summertime transport and impact of african dust over the red sea and arabian peninsula. *Journal of Geophysical Research: Atmospheres*, *121*(11), 6435–6458.

Kalenderski, S., Stenchikov, G. L., & Zhao, C. (2013). Modeling a typical wintertime dust event over the arabian peninsula and the red sea. *Atmospheric Chemistry and Physics*.

Knippertz, P., & Stuut, J.-B. W. (2014). Mineral dust. *Mineral dust—A key player in the Earth system*, 121–147.

Kok, J. F. (2011). Does the size distribution of mineral dust aerosols depend on the wind speed at emission? *Atmospheric Chemistry and Physics*, *11*(19), 10149–10156.

Kok, J. F., Adebiyi, A. A., Albani, S., Balkanski, Y., Checa-Garcia, R., Chin, M., ... others (2021). Contribution of the world's main dust source regions to the global cycle of desert dust. *Atmospheric Chemistry and Physics*, *21*(10), 8169–8193.

Kok, J. F., Ridley, D., Zhou, Q., Miller, R., Zhao, C., Heald, C., ... Haustein, K. (2017). *Smaller desert dust cooling effect estimated from analysis of dust size and abundance* (Vol. 10) (No. 4). Nature Geoscience.

Landau, L. D., Bell, J. S., Kearsley, M., Pitaevskii, L., Lifshitz, E., & Sykes, J. (2013). *Electrodynamics of continuous media* (Vol. 8). elsevier.

Levy, R., Hsu, C., et al. (2015). Modis atmosphere l2 aerosol product. *NASA MODIS Adaptive Processing System, Goddard Space Flight Center, USA, doi*,

10.
Madronich, S. (1987). Photodissociation in the atmosphere: 1. actinic flux and the effects of ground reflections and clouds. *Journal of Geophysical Research: Atmospheres*, *92*(D8), 9740–9752.
Maghami, M. R., Hizam, H., Gomes, C., Radzi, M. A., Rezadad, M. I., & Hajighorbani, S. (2016). Power loss due to soiling on solar panel: A review. *Renewable and Sustainable Energy Reviews*, *59*, 1307–1316.
Mahowald, N., Ward, D. S., Kloster, S., Flanner, M. G., Heald, C. L., Heavens, N. G., ... Chuang, P. Y. (2011). Aerosol impacts on climate and biogeochemistry. *Annual review of environment and resources*, *36*, 45–74.
Mallet, M., Tulet, P., Serça, D., Solmon, F., Dubovik, O., Pelon, J., ... Thouron, O. (2009). Impact of dust aerosols on the radiative budget, surface heat fluxes, heating rate profiles and convective activity over west africa during march 2006. *Atmospheric Chemistry and Physics*, *9*(18), 7143–7160.
Mani, M., & Pillai, R. (2010a). Impact of dust on solar photovoltaic (pv) performance: Research status, challenges and recommendations. *Renewable and Sustainable Energy Reviews*, *14*(9), 3124 - 3131. Retrieved from `http://www.sciencedirect.com/science/article/pii/S1364032110002455` doi: https://doi.org/10.1016/j.rser.2010.07.065
Mani, M., & Pillai, R. (2010b). Impact of dust on solar photovoltaic (pv) performance: Research status, challenges and recommendations. *Renewable and sustainable energy reviews*, *14*(9), 3124–3131.
Marticorena, B., & Bergametti, G. (1995). Modeling the atmospheric dust cycle: 1. design of a soil-derived dust emission scheme. *Journal of geophysical research: atmospheres*, *100*(D8), 16415–16430.
Martin, J. H. (1990). Glacial-interglacial co2 change: The iron hypothesis. *Paleoceanography*, *5*(1), 1–13.
McConnell, C., Formenti, P., Highwood, E., & Harrison, M. (2010). Using aircraft measurements to determine the refractive index of saharan dust during the dodo experiments. *Atmospheric Chemistry and Physics*, *10*(6), 3081–3098.
Meng, J., Huang, Y., Leung, D. M., Li, L., Adebiyi, A. A., Ryder, C. L., ... Kok, J. F. (2022). Improved parameterization for the size distribution of emitted dust aerosols reduces model underestimation of super coarse dust. *Geophysical research letters*, *49*(8), e2021GL097287.
Meng, Z., & Lu, B. (2007). Dust events as a risk factor for daily hospitalization for respiratory and cardiovascular diseases in minqin, china. *Atmospheric environment*, *41*(33), 7048–7058.
Miller, R., & Tegen, I. (1998). Climate response to soil dust aerosols. *Journal of climate*, *11*(12), 3247–3267.
Mlawer, E., & Clough, S. (1998). Shortwave and longwave enhancements in the rapid radiative transfer model. In *Proceedings of the 7th atmospheric radiation measurement (arm) science team meeting* (pp. 409–413).
Mlawer, E. J., Taubman, S. J., Brown, P. D., Iacono, M. J., & Clough, S. A. (1997). Radiative transfer for inhomogeneous atmospheres: Rrtm, a validated correlated-k model for the longwave. *Journal of Geophysical Research: Atmospheres*, *102*(D14), 16663–16682.
Mok, J., Krotkov, N. A., Arola, A., Torres, O., Jethva, H., Andrade, M., ... others (2016). Impacts of brown carbon from biomass burning on surface uv and ozone photochemistry in the amazon basin. *Scientific reports*, *6*(1), 1–9.
Morcrette, J.-J., Boucher, O., Jones, L., Salmond, D., Bechtold, P., Beljaars, A., ... others (2009). Aerosol analysis and forecast in the european centre for medium-range weather forecasts integrated forecast system: Forward modeling. *Journal of Geophysical Research: Atmospheres*, *114*(D6).
Mostamandi, S., Predybaylo, E., Osipov, S., Zolina, O., Gulev, S., Parajuli, S., & Stenchikov, G. (2022). Sea breeze geoengineering to increase rainfall over the

arabian red sea coastal plains. *Journal of Hydrometeorology*, *23*(1), 3–24.

Myhre, G., Myhre, C., Samset, B., & Storelvmo, T. (2013). Aerosols and their relation to global climate and climate sensitivity. *Nature Education Knowledge*, *4*(5), 7.

Osipov, S., Chowdhury, S., Crowley, J. N., Tadic, I., Drewnick, F., Borrmann, S., … others (2022). Severe atmospheric pollution in the middle east is attributable to anthropogenic sources. *Communications Earth & Environment*, *3*(1), 1–10.

Osipov, S., & Stenchikov, G. (2018). Simulating the regional impact of dust on the middle east climate and the red sea. *Journal of Geophysical Research: Oceans*, *123*(2), 1032–1047.

Osipov, S., Stenchikov, G., Brindley, H., & Banks, J. (2015). Diurnal cycle of the dust instantaneous direct radiative forcing over the arabian peninsula. *Atmospheric Chemistry and Physics*, *15*(16), 9537–9553.

Osipov, S., Stenchikov, G., Tsigaridis, K., LeGrande, A. N., & Bauer, S. E. (2020). The role of the so radiative effect in sustaining the volcanic winter and soothing the toba impact on climate. *Journal of Geophysical Research: Atmospheres*, *125*(2), e2019JD031726.

Parajuli, S. P., Stenchikov, G. L., Ukhov, A., Mostamandi, S., Kucera, P. A., Axisa, D., … Zhu, Y. (2022). Effect of dust on rainfall over the red sea coast based on wrf-chem model simulations. *Atmospheric Chemistry and Physics*, *22*(13), 8659–8682.

Patlakas, P., Stathopoulos, C., Flocas, H., Kalogeri, C., & Kallos, G. (2019). Regional climatic features of the arabian peninsula. *Atmosphere*, *10*(4), 220.

Pósfai, M., Axisa, D., Tompa, É., Freney, E., Bruintjes, R., & Buseck, P. R. (2013). Interactions of mineral dust with pollution and clouds: An individual-particle tem study of atmospheric aerosol from saudi arabia. *Atmospheric Research*, *122*, 347–361.

Prospero, J. M., Blades, E., Naidu, R., Mathison, G., Thani, H., & Lavoie, M. C. (2008). Relationship between african dust carried in the atlantic trade winds and surges in pediatric asthma attendances in the caribbean. *International Journal of Biometeorology*, *52*(8), 823–832.

Randles, C., Da Silva, A., Buchard, V., Colarco, P., Darmenov, A., Govindaraju, R., … others (2017). The merra-2 aerosol reanalysis, 1980 onward. part i: System description and data assimilation evaluation. *Journal of climate*, *30*(17), 6823–6850.

Rao, A., Pillai, R., Mani, M., & Ramamurthy, P. (2014). Influence of dust deposition on photovoltaic panel performance. *Energy Procedia*, *54*, 690 - 700. Retrieved from `http://www.sciencedirect.com/science/article/pii/S1876610214011874` (4th International Conference on Advances in Energy Research (ICAER 2013)) doi: https://doi.org/10.1016/j.egypro.2014.07.310

Rashki, A., Kaskaoutis, D., Mofidi, A., Minvielle, F., Chiapello, I., Legrand, M., … Francois, P. (2019). Effects of monsoon, shamal and levar winds on dust accumulation over the arabian sea during summer–the july 2016 case. *Aeolian Research*, *36*, 27–44.

Remer, L. A., Kaufman, Y., Tanré, D., Mattoo, S., Chu, D., Martins, J. V., … others (2005). The modis aerosol algorithm, products, and validation. *Journal of atmospheric sciences*, *62*(4), 947–973.

Rienecker, M. M., Suarez, M., Todling, R., Bacmeister, J., Takacs, L., Liu, H., … others (2008). *The geos-5 data assimilation system: Documentation of versions 5.0. 1, 5.1. 0, and 5.2. 0* (Tech. Rep.). NASA Goddard Space Flight Center, Greenbelt, Maryland.

Ryder, C. L., Highwood, E. J., Walser, A., Seibert, P., Philipp, A., & Weinzierl, B. (2019). Coarse and giant particles are ubiquitous in saharan dust export regions and are radiatively significant over the sahara. *Atmospheric Chemistry and Physics*, *19*(24), 15353–15376.

Sayyah, A., Horenstein, M. N., & Mazumder, M. K. (2014). Energy yield loss caused by dust deposition on photovoltaic panels. *Solar Energy*, *107*, 576–604.

Scheuvens, D., & Kandler, K. (2014). On composition, morphology, and size distribution of airborne mineral dust. *Mineral Dust*, 15–49.

Shao, Y. (2001). A model for mineral dust emission. *Journal of Geophysical Research: Atmospheres*, *106*(D17), 20239–20254.

Shao, Y., Fink, A. H., & Klose, M. (2010). Numerical simulation of a continental-scale saharan dust event. *Journal of Geophysical Research: Atmospheres*, *115*(D13).

Shevchenko, I., Engelbrecht, J. P., Mostamandi, S., & Stenchikov, G. (2021, July). Evaluation of minerals being deposited in the red sea using gravimetric, size distribution, and mineralogical analysis of dust deposition samples collected along the red sea coastal plain. *Aeolian Research*, *52*, 100717. Retrieved from `https://doi.org/10.1016/j.aeolia.2021.100717` doi: 10.1016/j.aeolia.2021.100717

Skamarock, W. C., Klemp, J. B., Dudhia, J., Gill, D. O., Barker, D. M., Wang, W., & Powers, J. G. (2005). *A description of the advanced research wrf version 2* (Tech. Rep.). National Center For Atmospheric Research Boulder Co Mesoscale and Microscale ....

Solomos, S., Kallos, G., Kushta, J., Astitha, M., Tremback, C., Nenes, A., & Levin, Z. (2011). An integrated modeling study on the effects of mineral dust and sea salt particles on clouds and precipitation. *Atmospheric Chemistry and Physics*, *11*(2), 873–892.

Stockwell, W. R., Kirchner, F., Kuhn, M., & Seefeld, S. (1997). A new mechanism for regional atmospheric chemistry modeling. *Journal of Geophysical Research: Atmospheres*, *102*(D22), 25847–25879.

Sulaiman, S. A., Singh, A. K., Mokhtar, M. M. M., & Bou-Rabee, M. A. (2014). Influence of dirt accumulation on performance of pv panels. *Energy Procedia*, *50*, 50 - 56. Retrieved from `http://www.sciencedirect.com/science/article/pii/S1876610214007425` (Technologies and Materials for Renewable Energy, Environment and Sustainability (TMREES14 – EUMISD)) doi: https://doi.org/10.1016/j.egypro.2014.06.006

Sunda, W. G., & Huntsman, S. A. (1997). Interrelated influence of iron, light and cell size on marine phytoplankton growth. *Nature*, *390*(6658), 389–392.

Swap, R., Ulanski, S., Cobbett, M., & Garstang, M. (1996). Temporal and spatial characteristics of saharan dust outbreaks. *Journal of Geophysical Research: Atmospheres*, *101*(D2), 4205–4220.

Talbot, R., Harriss, R., Browell, E., Gregory, G., Sebacher, D., & Beck, S. (1986). Distribution and geochemistry of aerosols in the tropical north atlantic troposphere: Relationship to saharan dust. *Journal of Geophysical Research: Atmospheres*, *91*(D4), 5173–5182.

Tegen, I., Harrison, S. P., Kohfeld, K., Prentice, I. C., Coe, M., & Heimann, M. (2002). Impact of vegetation and preferential source areas on global dust aerosol: Results from a model study. *Journal of Geophysical Research: Atmospheres*, *107*(D21), AAC–14.

Textor, C., Schulz, M., Guibert, S., Kinne, S., Balkanski, Y., Bauer, S., ... others (2006). Analysis and quantification of the diversities of aerosol life cycles within aerocom. *Atmospheric Chemistry and Physics*, *6*(7), 1777–1813.

Tindale, N., & Pease, P. (1999). Aerosols over the arabian sea: Atmospheric transport pathways and concentrations of dust and sea salt. *Deep Sea Research Part II: Topical Studies in Oceanography*, *46*(8-9), 1577–1595.

Todd, M. C., Bou Karam, D., Cavazos, C., Bouet, C., Heinold, B., Baldasano, J. M., ... others (2008). Quantifying uncertainty in estimates of mineral dust flux: An intercomparison of model performance over the bodélé depression, northern chad. *Journal of Geophysical Research: Atmospheres*, *113*(D24).

Ukhov, A., Ahmadov, R., Grell, G., & Stenchikov, G. (2021). Improving dust simulations in wrf-chem v4. 1.3 coupled with the gocart aerosol module. *Geoscientific Model Development*, *14*(1), 473–493.

Ukhov, A., Mostamandi, S., da Silva, A., Flemming, J., Alshehri, Y., Shevchenko, I., & Stenchikov, G. (2020). Assessment of natural and anthropogenic aerosol air pollution in the middle east using merra-2, cams data assimilation products, and high-resolution wrf-chem model simulations. *Atmospheric Chemistry and Physics*, *20*(15), 9281–9310.

Ukhov, A., & Stenchikov, G. (2020, March). *Merra2bc. interpolation utility for boundary and initial conditions used in wrf-chem.* Zenodo. Retrieved from `https://doi.org/10.5281/zenodo.3695911`

Uno, I., Wang, Z., Chiba, M., Chun, Y., Gong, S. L., Hara, Y., ... others (2006). Dust model intercomparison (dmip) study over asia: Overview. *Journal of Geophysical Research: Atmospheres*, *111*(D12).

Valerino, M., Bergin, M., Ghoroi, C., Ratnaparkhi, A., & Smestad, G. P. (2020). Low-cost solar pv soiling sensor validation and size resolved soiling impacts: a comprehensive field study in western india. *Solar Energy*, *204*, 307–315.

Watson, A. J., Bakker, D., Ridgwell, A., Boyd, P., & Law, C. (2000). Effect of iron supply on southern ocean co2 uptake and implications for glacial atmospheric co2. *Nature*, *407*(6805), 730–733.

Yu, Y., Notaro, M., Kalashnikova, O. V., & Garay, M. J. (2016). Climatology of summer shamal wind in the middle east. *Journal of Geophysical Research: Atmospheres*, *121*(1), 289–305.

Zender, C. S., Bian, H., & Newman, D. (2003). Mineral dust entrainment and deposition (dead) model: Description and 1990s dust climatology. *Journal of Geophysical Research: Atmospheres*, *108*(D14).

Zender, C. S., Miller, R., & Tegen, I. (2004). Quantifying mineral dust mass budgets: Terminology, constraints, and current estimates. *Eos, Transactions American Geophysical Union*, *85*(48), 509–512.

Zhao, C., Chen, S., Leung, L. R., Qian, Y., Kok, J., Zaveri, R. A., & Huang, J. (2013). Uncertainty in modeling dust mass balance and radiative forcing from size parameterization. *Atmospheric Chemistry and Physics*, *13*(21), 10733–10753.

Zhao, C., Hu, Z., Qian, Y., Ruby Leung, L., Huang, J., Huang, M., ... others (2014). Simulating black carbon and dust and their radiative forcing in seasonal snow: a case study over north china with field campaign measurements. *Atmospheric Chemistry and Physics*, *14*(20), 11475–11491.

Zhao, C., Liu, X., Leung, L., Johnson, B., McFarlane, S. A., Gustafson Jr, W., ... Easter, R. (2010). The spatial distribution of mineral dust and its shortwave radiative forcing over north africa: modeling sensitivities to dust emissions and aerosol size treatments. *Atmospheric Chemistry and Physics*, *10*(18), 8821–8838.

Zhao, C., Liu, X., Ruby Leung, L., & Hagos, S. (2011). Radiative impact of mineral dust on monsoon precipitation variability over west africa. *Atmospheric Chemistry and Physics*, *11*(5), 1879–1893.

Zhu, X., Prospero, J., & Millero, F. J. (1997). Diel variability of soluble fe (ii) and soluble total fe in north african dust in the trade winds at barbados. *Journal of Geophysical Research: Atmospheres*, *102*(D17), 21297–21305.

1 Supplementary Information

1.1 Line-by-line Radiative Transfer Model

To quantify the RF of dust, we performed the radiative transfer calculations using the line-by-line modeling framework. The framework was previously used in (Mok et al., 2016; Osipov et al., 2020) and is described in detail in Appendix A (Osipov et al., 2020). The Python wrapper to run the DISORT model is publicly available at `https://github.com/SeregaOsipov/pyDISORT`. This section outlines the modeling setup adjustments necessary to calculate the RF of aerosols.

We assumed the bright desert Lambertian surface and prescribed an albedo of 0.3. We do not consider the diurnal cycle (see Figure 12 in (Osipov et al., 2015)) and fixed the solar zenith angle at 0 degrees. The dust was distributed in the 5 km thick layer in the lower troposphere (characteristic height of the PBL). The number of particles in the size distribution was scaled to produce column AOD of 0.5 at 0.5 μm. The refractive index of dust was taken from the WRF-Chem model. The characteristic values of the imaginary part is 10^{-3} in shortwave and 0.65 at 10 μm. The shortwave and longwave spectra were discretized with 10 cm^{-1} step. Figure S1 shows the corresponding spectral optical properties of dust, while Figure S2 shows the CDFs, i.e. the relative contribution of the dust particles as the radius increases.

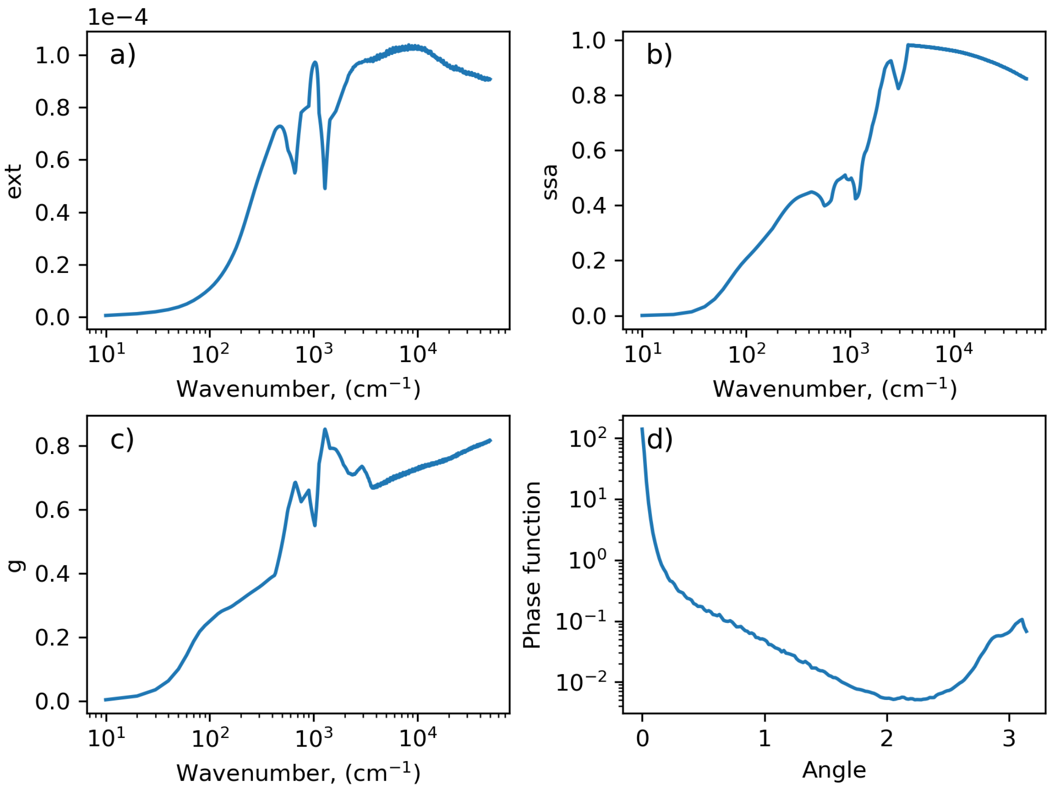

Figure S1: a) Spectral extinction, b) single-scattering albedo, c) asymmetry parameter, and d) phase function for the dust PSD observed after the Haboob dust storm in Saudi Arabia on 9 April 2009. The corresponding dust size distribution is shown in the main text (Figure 11, left column). The number of particles was normalized to produce column AOD of 0.5 at 0.5 μm.

Table S1: Statistical scores (R, RMSE, and Bias) of DD for particles with r < 5 μm simulated within WRF-Chem, MERRA2, and CAMS compared to observations for 2016.

	R	RMSE	Bias
WRF-Chem (Ukhov et al., 2020)	0.70	0.94	0.31
WRF-Chem (This Study)	0.64	1.04	-0.29
MERRA-2	0.41	1.11	-0.24
CAMS	0.36	1.14	0.29

References

Mok, J., Krotkov, N. A., Arola, A., Torres, O., Jethva, H., Andrade, M., … others (2016). Impacts of brown carbon from biomass burning on surface uv and ozone photochemistry in the amazon basin. *Scientific reports*, *6*(1), 1–9.

Osipov, S., Stenchikov, G., Brindley, H., & Banks, J. (2015). Diurnal cycle of the dust instantaneous direct radiative forcing over the arabian peninsula. *Atmospheric Chemistry and Physics*, *15*(16), 9537–9553.

Osipov, S., Stenchikov, G., Tsigaridis, K., LeGrande, A. N., & Bauer, S. E. (2020). The role of the so radiative effect in sustaining the volcanic winter and soothing the toba impact on climate. *Journal of Geophysical Research: Atmospheres*, *125*(2), e2019JD031726.

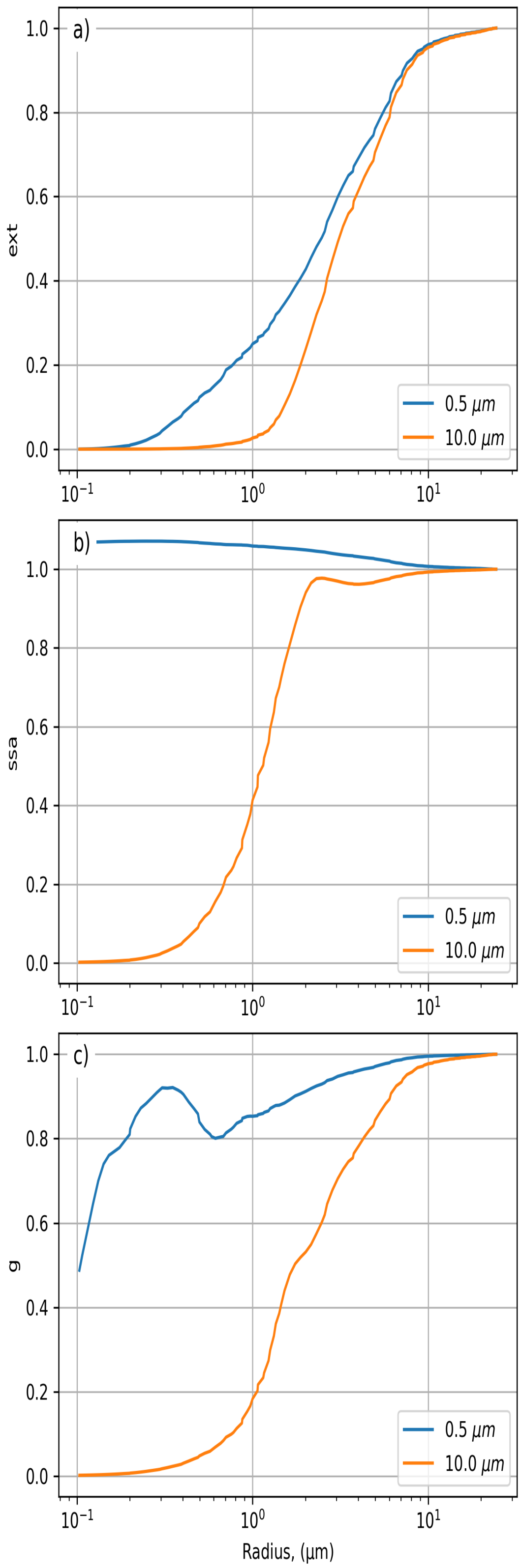

Figure S2: Relative contribution (CDFs) of the dust particles up to radius r to the SW and LW dust optical properties: a) extinction, b) single-scattering albedo, and c) asymmetry parameter shown in Figure S1.

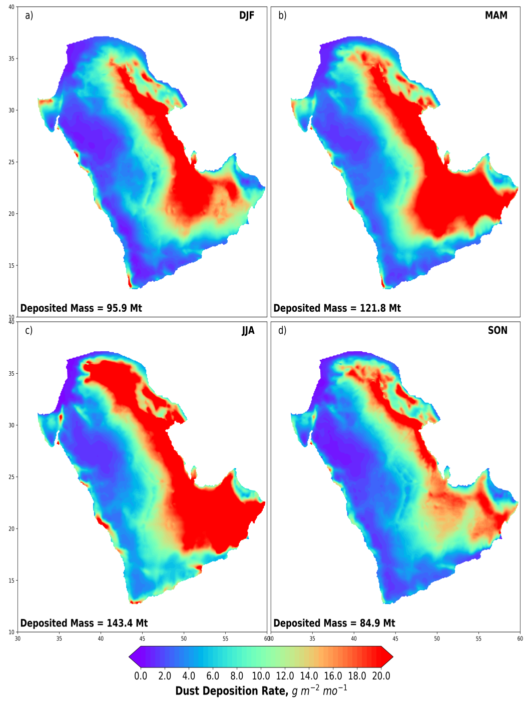

Figure S3: Seasonal mean dust deposition rate $g\ m^{-2}\ mo^{-1}$ in the Arabian Peninsula calculated in WRF-Chem with the DD constraints for 2016: a) DJF, b) MAM, c) JJA, and d) SON. The spatially integrated mass of deposited dust is shown in each panel at the bottom.

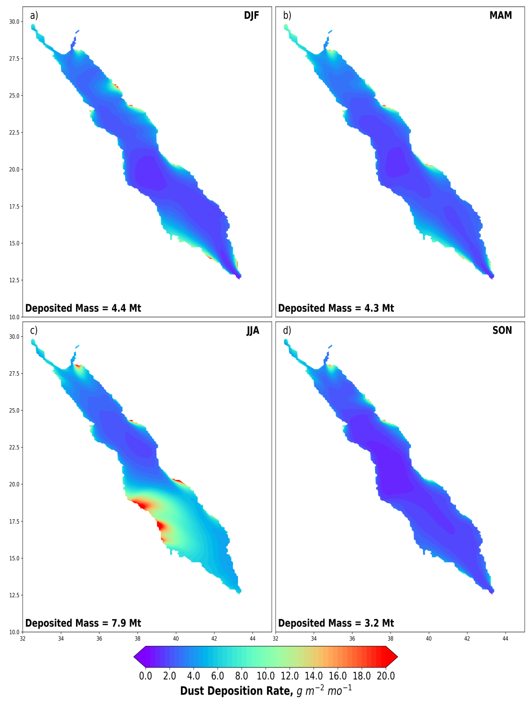

Figure S4: Seasonal mean dust deposition rate $g\ m^{-2}\ mo^{-1}$ in the Red Sea calculated in WRF-Chem with the DD constraints for 2016: a) DJF, b) MAM, c) JJA, and d) SON. The spatially integrated mass of deposited dust is shown in each panel at the bottom.

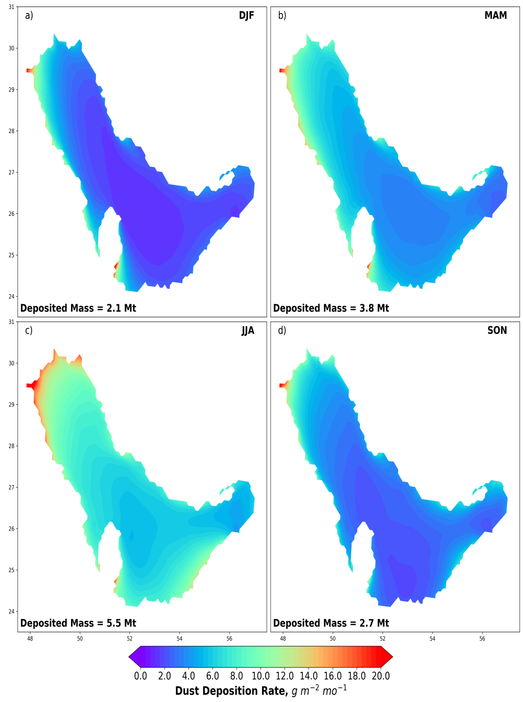

Figure S5: Seasonal mean dust deposition rate $g\ m^{-2}\ mo^{-1}$ in the Arabian Gulf calculated in WRF-Chem with the DD constraints for 2016: a) DJF, b) MAM, c) JJA, and d) SON. The spatially integrated mass of deposited dust is shown in each panel at the bottom.